Physics of Fluids

RESEARCH ARTICLE | JANUARY 03 2024

Hydrodynamic responses and layout optimization of wave energy converter arrays consisting of five-degree-of-freedom truncated cylinders in front of a vertical wall

Yuanshun Kang (康元顺) ; Xiaohui Zeng (曾晓辉) ; Zhehua Cui (崔哲华) ; Jiahao Chen (陈嘉昊)

Physics of Fluids 36, 017102 (2024)
https://doi.org/10.1063/5.0184849

Physics of Fluids ARTICLE pubs.aip.org/aip/pof

Hydrodynamic responses and layout optimization of wave energy converter arrays consisting of five-degree-of-freedom truncated cylinders in front of a vertical wall

Cite as: Phys. Fluids **36**, 017102 (2024); doi: 10.1063/5.0184849
Submitted: 27 October 2023 · Accepted: 8 December 2023 ·
Published Online: 3 January 2024

View Online Export Citation CrossMark

Yuanshun Kang (康元顺),[1,2] Xiaohui Zeng (曾晓辉),[1,2,a)] Zhehua Cui (崔哲华),[1,2,3] and Jiahao Chen (陈嘉昊)[1,2]

AFFILIATIONS

[1]Institute of Mechanics, Chinese Academy of Sciences, Beijing 100190, China
[2]School of Engineering Science, University of Chinese Academy of Sciences, Beijing 100049, China
[3]School of Future Technology, University of Chinese Academy of Sciences, Beijing 100049, China

[a)]Author to whom correspondence should be addressed: zxh@imech.ac.cn

ABSTRACT

The hydrodynamic responses and layout optimization of a group of cylindrical wave energy conversion devices (WEC) in front of a fully reflecting vertical wall are investigated. Each truncated floating cylinder can oscillate with five degrees of freedom, i.e., surge, sway, heave, roll, and pitch. Based on the linear water wave theory, an analytical solution is developed for the hydrodynamic problem. The results of specific parameter studies suggest that the wall reflection effect significantly improves the energy extraction performance of the WEC array with the appropriate parameter conditions. A multi-level optimization method based on a genetic algorithm is developed. This paper investigates the optimal layout of the six WEC arrays, composed of 2–7 buoys, respectively. Additionally, the impact of other degrees of freedom (DOFs), besides the heave mode, on the hydrodynamic performance of the array is investigated. For $\beta \leq \pi/12$, there is no need to consider the impact of other DOFs on the energy extraction in heave mode. The dimensionless amplitudes of other DOFs gradually decrease as the equivalent constraint stiffness increases. For $k_0a > 1.0$, the heave amplitude and energy capture performance of the WEC array are significantly smaller. However, the amplitudes of other DOFs still have considerable magnitudes for $k_0a > 1.0$. Therefore, for the sea area with high-frequency incident waves ($k_0a > 1.0$), setting up a power takeoff system on other DOFs of each buoy to extract energy is a feasible solution to improve the performance of the WEC array.

I. INTRODUCTION

Currently, in order to alleviate the global energy shortage and reduce greenhouse gas emissions, many renewable energy sources are being developed and utilized, such as wind energy, solar energy, tidal energy, and wave energy (Wang, 2017). In the past few decades, the research and development on wave energy has attracted the attention of many scholars (McIver and Evans, 1988; Mavrakos and McIver, 1997; Child and Venugopal, 2010; Parrinello *et al.*, 2020; Wang *et al.*, 2022; Zeng *et al.*, 2022c; and Zhang *et al.*, 2023). The oscillating-type wave energy converter (WEC) has attracted widespread attention due to its wide adaptability and high efficiency. At the moment, the WEC system still suffers from high costs compared to conventional electricity generation such as from coal power plants (He *et al.*, 2013). The economics of the WEC system can be enhanced by improving its efficiency. In order to improve the energy capture efficiency of the WEC array, many scholars (Child and Venugopal, 2010; Giassi and Göteman, 2018) have developed different optimization methods to optimize the geometric dimensions, physical parameters, and spatial layout of the buoys. Zeng *et al.* (2022c) developed a better-performing WEC system that can extract energy in multi-degrees of freedom (DOF). Another way to increase the attractiveness of the WEC is to integrate the WEC into other maritime structures such as breakwater. Many countries have several examples of implemented projects on wave energy devices and breakwater integration, which proved the effectiveness of the idea, by supplying electricity to the island community and providing shelter to the near-shore area (Mustapa, 2017). Many previous studies (Loukogeorgaki *et al.*, 2021; Kara, 2022; and Li and Liu, 2022) have shown that the WEC system can be integrated

with breakwaters/coasts/walls to share the construction cost and improve energy extraction performance. Such integrated WEC systems can be modeled as cylinder arrays in front of a vertical wall. How to arrange the positions of each cylinder in the array to improve the efficiency of wave energy extraction is an important issue, which is the main motivation of this study.

In order to more effectively exploit wave energy resources and achieve megawatt-level power generation capacity, WEC must be arranged in an array (Giassi and Göteman, 2018). Hydrodynamic interactions among buoys by diffraction and radiation of water waves may have constructive or destructive effects on the overall energy extraction performance of the WEC array. To date, extensive research efforts have been conducted to accurately calculate the hydrodynamic interactions among each buoy in the array. For hydrodynamic problems of general geometric structures, numerical methods such as the boundary element method, the finite element method, and the finite difference method are usually used to solve (Chen *et al.*, 2011). However, for geometric structures with regular cross sections such as vertical barriers, spheres, and vertical cylinders, analytical methods are appropriate (Chanda and Bora, 2020; 2022; Zeng *et al.*, 2019; and Li and Liu, 2022). It can not only effectively reduce computational costs but also provide a clear understanding of the physical meaning of the hydrodynamic problem. In the context of linear water waves, Kagemoto and Yue (1986) combined the multiple scattering method (Okhusu, 1974) and the direct matrix method (Spring and Monkmeyer, 1974) to derive an analytical method called the exact algebraic method. This method was widely adopted in subsequent studies (Flavia and Meylan, 2019; Wang *et al.*, 2022). Linton and Evans (1990) proposed an analytical method that can accurately solve the water wave diffraction problem of the bottom-mounted cylinder array. Zheng *et al.* (2020) investigated the hydroelastic interaction between water waves and submerged porous elastic disks of negligible thickness. Their results demonstrate that deploying multiple disks in an array is a more promising approach for wave power absorption/dissipation compared to enlarging the area of an isolated disk. Chanda *et al.* (2022) conducted the scattering problem of a bottom-mounted surface-piercing compound porous cylinder located on a porous seabed based on the linear water wave theory. Their results show that the efficiency of the proposed compound cylinder in mitigating wave impact can be enhanced by suitable consideration of porosity and structure parameters. Based on the framework of linear water wave theory, Chanda and Pramanik (2023) theoretically investigated the water wave scattering by a surface-piercing porous breakwater in the presence of a thin vertical porous barrier. Sarkar and Chanda (2022) further studied the scattering problem of a submerged bottom-mounted compound porous cylinder located on a porous sea-bed under the framework of linear water wave theory. Their results show that the suitable positioning of the annular spacing of the system can reduce the exciting force acting on the inner and outer cylinders. Zeng *et al.* (2016; 2019; 2022a) used the analytical method to investigate the hydrodynamic interactions of the truncated floating cylinder array and the bottom-mounted cylinder array, respectively.

In order to improve the energy extraction performance of the array with a large number of buoys, many scholars (Tokić and Yue, 2019; Zhong and Yeung, 2019; Dafnakis *et al.*, 2020; Liu *et al.*, 2022; and Zhu *et al.*, 2023) conducted the hydrodynamic performance of the WEC array in an open water domain and proposed different optimization techniques to optimize the geometric dimensions, physical parameters, and spatial layout. McGuinness and Thomas (2016) used sequential quadratic programing to investigate the optimal layout of the WEC array with 5–7 spherical buoys. The geometry of the array was restricted to straight lines or circles. In other words, the array can be described by several parameters. Neshat *et al.* (2019) used artificial neural networks to research the optimal layout of the WEC array with 16 buoys. This method demonstrates excellent adaptability and rapid optimization speed. Child and Venugopal (2010) used a genetic algorithm and parabolic intersection method to optimize an array composed of five buoys and compared the optimization results. Mercadé Ruiz *et al.* (2017) proposed a new layout optimization strategy and compared the performance and computational cost of three optimization methods, i.e., the covariance matrix adaptation evolution strategy (CMA), a genetic algorithm (GA), and the glowworm swarm optimization (GSO) algorithm. Fang *et al.* (2018) proposed an improved differential evolution algorithm and conducted layout optimization for the arrays consisting of 3, 5, and 8 buoys, respectively. Their calculation results demonstrated that the layout optimization effectively improves the energy capture performance of the WEC array. Sharp and Dupont (2018) used a binary genetic algorithm to perform array optimization on the WEC array with five buoys and examined the impact of the minimum separation distance on the optimization results. Based on the genetic algorithm toolbox in MATLAB, Giassi and Göteman (2018) proposed two layout optimization schemes for the point-absorbing wave energy converter array and optimized the arrangement of the array composed of 4–14 buoys in limited sea areas. In order to reduce construction costs, facilitate maintenance, and meet navigation needs, Balitsky *et al.* (2018) aggregated the WEC array into several sub-arrays. This layout method showed promising application prospects and attracted the attention of many scholars. Tokić and Yue (2019) investigated the fluid dynamics of WEC arrays consisting of periodically repeated single bodies or sub-arrays. Their results demonstrated that a significant decrease in the energy extraction performance of the array is related to Laue resonance. In order to achieve fast calculation, Zhong and Yeung (2019) used a new "Haskind" relationship to calculate the hydrodynamic properties of the WEC array and combined this method with the point absorption approximation method to study the interacting factors of a large wave farm composed of multiple sub-arrays. To improve the optimization efficiency of the WEC array with a large number of buoys, Zeng *et al.* (2022b) proposed a hierarchical optimization algorithm based on a matrix-encoded genetic algorithm. This method initially divided the large-scale array into several sub-arrays that are easy to handle and subsequently utilized a genetic algorithm to optimize sub-arrays.

The above works focus on the layout optimization of the WEC array in an open water domain. In sea areas near a coast, the WEC system can be combined with existing coastal structures, such as vertical breakwaters, which can not only improve the energy capture performance of the WEC system but also help share the construction cost and facilitate later maintenance and operation. Therefore, the WEC array near coasts/walls/breakwaters has received much attention. Kara (2021) used a boundary element method to investigate the wave energy extraction performance of the WEC array in front of a vertical wall. The WEC array consists of three different shapes of buoys, including truncated vertical cylinders, vertical cylinders with hemispherical bottoms, and floating spheres. Kara (2022) used the three-dimensional

transient Green's function direct time domain method to study the energy extraction performance of the WEC array near a vertical wall. Their calculation revealed that the reflection of a vertical wall can significantly improve the performance of the array. Loukogeorgaki and Chatjigeorgiou (2019) analyzed the hydrodynamic performance of a truncated floating cylindrical array near a bottom-mounted vertical wall in the frequency domain and compared the situations of infinite and finite walls. Their calculation results showed that the concept of "infinite straight wall" will lead to an underestimation or overestimation of the heave excitation force within the low-frequency range, but has less impact within the high-frequency region. Based on the linear water wave theory, Konispoliatis *et al.* (2020) developed a semi-analytical method to investigate the hydrodynamic characteristics and energy extraction performance of a cylindrical WEC array in front of an infinitely long vertical breakwater. Their calculation results showed that the energy extraction performance of the array is affected by the distance between the center of each buoy and a vertical wall, the WEC array arrangement, and the incident angle. Li and Liu (2022) established a hydrodynamic analysis model of a submerged spherical WEC array near a vertical wall based on the context of linear water waves. They investigated the influence of the number of buoys, the spacing between the center of each buoy and a vertical wall, and the incident angle on the energy extraction performance of the linearly arranged WEC array near a vertical wall. Their calculation results showed that the reflection effect of a vertical wall could improve the overall energy extraction performance of the WEC system. Loukogeorgaki *et al.* (2021) conducted the first study on the layout optimization of a cluster of heaving point absorbs in front of a vertical wall. They developed an optimization framework based on a genetic algorithm to determine the optimal layout for unidirectional irregular waves. However, in their cases, the layout of the WEC array was restricted to a linear arrangement, i.e., the buoys were arranged along the direction parallel to the vertical wall. Optimization efforts should also consider the possibility of installing buoys more randomly. Ioannou and Loukogeorgaki (2021) further coupled a genetic algorithm with a numerical model based on the frequency domain. For the case of regular waves, they also investigated the optimal layout of five ellipsoidal WECs in front of the finite-length bottom-mounted vertical wall in a limited sea area. However, their hydrodynamic model only tested the optimal layout of 1DOF elliptical WEC arrays.

The aforementioned extensive studies demonstrated that the presence of straight walls/coasts/breakwaters could improve the energy extraction performance of the WEC array. This paper investigates the hydrodynamic interaction of the truncated floating cylindrical WEC array near a straight coast. All buoys can move independently with five DOFs, and the coast is regarded as a fully reflecting vertical wall. Many scholars (Konispoliatis, 2020; Kara, 2022) investigated the hydrodynamic performance of cylindrical WEC arrays near a vertical wall. To our knowledge, published studies have only considered the case in which the buoys oscillate in heave mode without other degrees of freedom. The previous research (Zeng *et al.*, 2022d) demonstrated significant differences in the amplitude response and energy extraction performance of the 5DOF model and the 1DOF (heave) model in an open water domain. Therefore, the hydrodynamic performance of the WEC arrays composed of five-degree-of-freedom truncated floating cylinders in front of a vertical wall remain gap and deserve our full attention. Based on the linear water wave theory, a theoretical analysis model for the hydrodynamic performance of the WEC array near a vertical wall is developed. Based on the image principle, the current physical problem is converted into an equivalent hydrodynamic problem in an open water domain. Many scholars (Zheng and Zhang, 2016; Loukogeorgaki and Chatjigeorgiou, 2019; Zhang *et al.*, 2020; Li and Liu, 2022; Li *et al.*, 2023; and Konispoliatis, 2023) adopted and verified the image principle to solve the hydrodynamic problem near a vertical wall. Then, the analytical solution to the equivalent hydrodynamic problem is solved using eigenfunction expansion and Graf's addition theorem of Bessel functions. Based on the analytical model, the influence of wall reflection and hydrodynamic interaction of each buoy on the energy extraction performance of the WEC array is clarified. Furthermore, to improve the energy extraction performance of the WEC array, a multi-level optimization method based on a genetic algorithm is proposed to optimize the spatial layout. To the authors' knowledge, there is a gap in existing optimization research of cylindrical WEC arrays in front of a vertical wall.

The rest of this paper is organized as follows: In Sec. II, an analytical solution of wave diffraction and radiation for the cylindrical WEC array near a vertical wall is developed based on the linear water wave theory. Each buoy in the array is modeled as truncated floating cylinders that can oscillate with five degrees of freedom, i.e., surge, sway, heave, roll, and pitch. The specific expressions of wave excitation force, added mass, radiation damping, amplitudes of each DOF, and energy extraction performance of the buoys in the WEC array are described. Section III verifies the calculation results of the present study with published results. In Sec. IV, the impact of different parameters on the energy extraction performance of the WEC array is investigated. Section V develops a multi-level optimization method based on a genetic algorithm and investigates the optimal layout of a WEC array containing different numbers of buoys for two different grid densities. Section VI examines the effects of other DOFs, besides heave, on the energy extraction performance of the array. Finally, the main conclusions of this paper are drawn in Sec. VII.

II. MATHEMATICAL MODEL

This study is based on the context of time-harmonic linear water waves without considering complex flow conditions such as nonlinearity of the free water surface and wave breaking, i.e., the fluid is incompressible, non-viscous, irrotational, and non-separated. Figure 1 shows a schematic diagram of a cylindrical wave energy extraction device near a vertical wall. The mathematical model uses a global three-dimensional Cartesian coordinate system o-xyz, where the xy plane is located on the undisturbed free surface, the x axis points outside the fluid, the y axis extends along the vertical wall, and the z axis points vertically upward. The water depth d is assumed to be constant. The vertical wall is fully reflective, and its length is much larger than the incident wavelength. The radius of cylinder j is a_j ($j = 1, 2, \ldots, N$), the draft is h_j, and the height of buoy j above the free surface is h_{upj}. All cylinders in the array can oscillate independently with five degrees of freedom, namely, surge, sway, heave, roll, and pitch. The yaw motion is not considered because it does not produce hydrodynamic force in the ideal fluid. The center of mass of cylinder j is at $(x_j, y_j, \bar{z}_j)$.

Based on the image principle (Teng *et al.*, 2004; Zheng and Zhang, 2015; Cong *et al.*, 2020; and Li and Liu, 2022), the current physical model is converted into an equivalent problem involving two groups of N cylinders in an open water domain, and the two groups

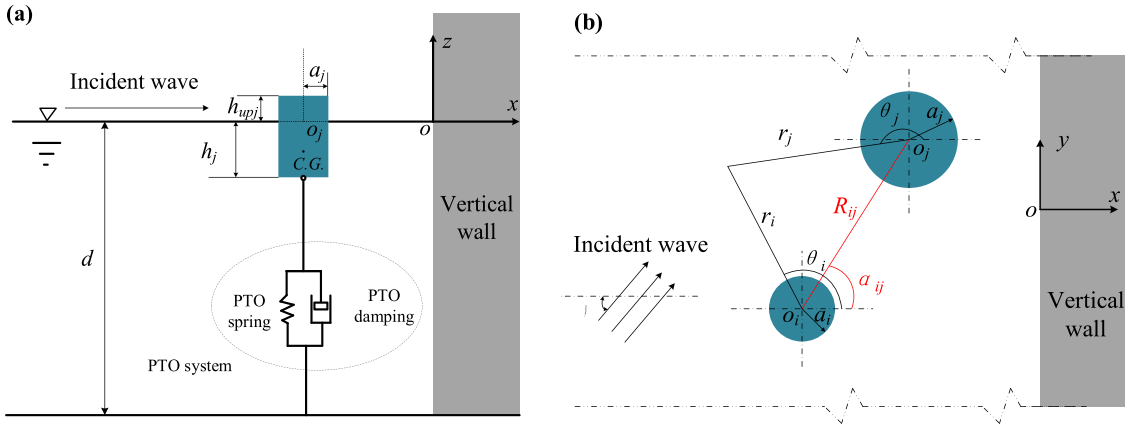

FIG. 1. Schematic of a cylindrical WEC near a vertical wall: (a) side view; (b) top view.

are symmetrical concerning the original wall. The top view of the equivalent hydrodynamic model is shown in Fig. 2.

The cylinder oscillates periodically with a small amplitude under the action of the incident water wave. The total velocity potential Φ can be expressed as

$$\Phi(x,y,z,t) = \mathrm{Re}\{\varphi(x,y,z)e^{-\mathrm{i}\omega_0 t}\}, \tag{1}$$

where Re represents the real part, φ is the spatial factor, $e^{-\mathrm{i}\omega_0 t}$ is time factor, ω_0 is the angular frequency of the ambient incident wave, and $\mathrm{i} = \sqrt{-1}$ represents the imaginary unit.

The fluid domain around each cylinder in the array is divided into two parts: the outer region and the core region, as shown in Fig. 3. The total velocity potential $\varphi^{(j)}$ in the vicinity of the j-cylinder can be divided into the total velocity potential in the exterior region $\varphi_E^{(j)}$ and core region $\varphi_C^{(j)}$. According to the principle of linear superposition, $\varphi_E^{(j)}$ can be further expanded as follows:

$$\varphi_E^{(j)} = \varphi_I + \sum_{i=1}^{2N} \varphi_{D-E}^{(i)} + \sum_{i=1}^{2N}\sum_{s=1}^{5} \zeta_s^{(j)} \varphi_{Rs-E}^{(i)}, \tag{2}$$

where φ_I is the velocity potential of ambient incident wave, $\varphi_{D-E}^{(i)}$ is the diffraction potential in the exterior region of cylinder i, and $\varphi_{Rs-E}^{(i)}$ is the radiation potential of cylinder i oscillating in s mode. To facilitate the solution, $\varphi_{D-E}^{(i)}$ is divided into two parts, $\varphi_{D0-E}^{(i)}$ and $\varphi_{D1-E}^{(i)}$. The first part of the diffraction potential $\varphi_{D0-E}^{(i)}$ is independent of the oscillations of each cylinder, whereas the second part of the diffraction potential $\varphi_{D1-E}^{(i)}$ is related to the oscillation of all cylinders. Therefore, Eq. (2) becomes

$$\varphi_E^{(j)} = \varphi_I + \sum_{i=1}^{2N} \varphi_{D0-E}^{(i)} + \sum_{i=1}^{2N}\sum_{s=1}^{5} \zeta_s^{(j)} \varphi_{Rs-E}^{(i)} + \sum_{i=1}^{2N} \varphi_{D1-E}^{(i)}. \tag{3}$$

Let

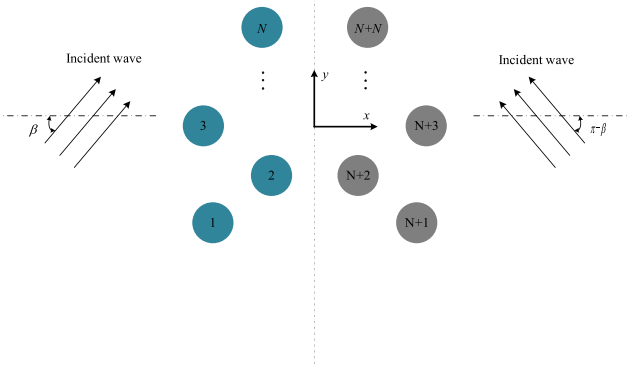

FIG. 2. Top view of the equivalent problem of wave–body interaction in an open water domain.

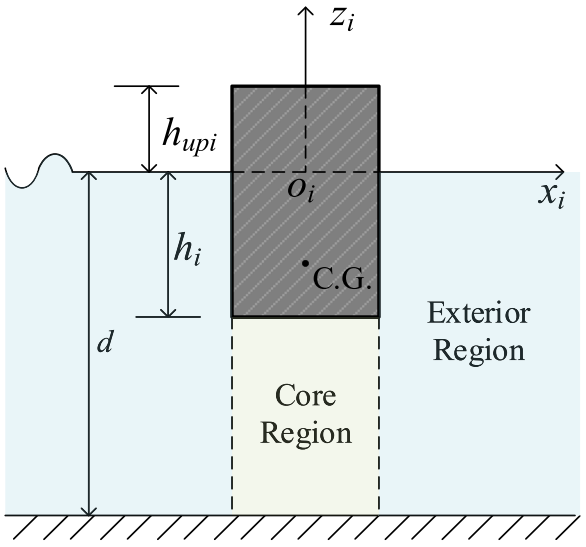

FIG. 3. Schematic diagram of division of core region and exterior region.

$$\varphi_{ID-E}^{(j)} = \varphi_I + \sum_{i=1}^{2N} \varphi_{D0-E}^{(i)},$$
$$\varphi_{RD-E}^{(j)} = \sum_{i=1}^{2N}\sum_{s=1}^{5} \zeta_s^{(j)} \varphi_{Rs-E}^{(i)} + \sum_{i=1}^{2N} \varphi_{D1-E}^{(i)}. \tag{4}$$

Consequently,

$$\varphi_E^{(j)} = \varphi_{ID-E}^{(j)} + \varphi_{RD-E}^{(j)}, \tag{5}$$

where $\varphi_{ID-E}^{(j)}$ is the velocity potential in the exterior region of cylinder j under the action of the ambient incident wave, and the subscript ID represents the incident diffraction. $\varphi_{RD-E}^{(j)}$ is the velocity potential in the exterior region of cylinder j when each cylinder in the array performs 5DOF oscillations with different amplitudes, and the subscript RD indicates radiation-diffraction.

Similarly, the velocity potential $\varphi_C^{(j)}$ in the core region of cylinder j can be divided into two parts: $\varphi_{ID-C}^{(j)}$ and $\varphi_{RD-C}^{(j)}$, that is,

$$\varphi_C^{(j)} = \varphi_{ID-C}^{(j)} + \varphi_{RD-C}^{(j)}, \tag{6}$$

where $\varphi_{ID-C}^{(j)}$ is the velocity potential in the core region in the presence of the ambient incident wave; $\varphi_{RD-C}^{(j)}$ is the velocity potential in the core region, induced by radiation (due to oscillations of cylinders) and the diffraction of radiation waves.

The diffraction problem and radiation problem of the WEC array in front of a vertical wall are discussed in Secs. II A and II B, respectively.

A. Diffraction problem

In the equivalent hydrodynamic model, two groups of N cylinders are subjected to double incident waves with the same amplitude and angular frequency. The incident wave amplitude is A, the angular frequency is ω_0, and the angle between the two incident waves and the positive direction of the x axis are β and π-β, respectively. Thus, the velocity potential of double incident waves can be written as

$$\varphi_I = -\frac{igA}{\omega_0} \sum_{m=-\infty}^{\infty} \left(I_j^{(1)} e^{im(\pi/2-\beta)} + I_j^{(2)} e^{im(-\pi/2+\beta)} \right) \cdot Y_0(z) J_m(k_0 r_j) e^{im\theta_j}, \tag{7}$$

where $I_j^{(1)} = e^{ik_0(x_j \cos\beta + y_j \sin\beta)}$ and $I_j^{(2)} = e^{ik_0(x_j \cos(\pi-\beta) + y_j \sin(\pi-\beta))}$ are spatial phase factors (x_j, y_j represent the coordinates of the j-cylinder in the global coordinate system); $Y_0 = \cosh k_0(z+d)/\cosh k_0 d$ is the characteristic function of the z direction; g represents the gravity acceleration; J_m is the m-order Bessel function of the first kind, and the wavenumber k_0 satisfies the dispersion relationship $k_0 \tanh k_0 d = \omega_0^2/g$.

For the diffracted wave of cylinder i, the velocity potential in the exterior region has the following form in the local coordinate system of i cylinder:

$$\varphi_{D0-E}^{(i)} = -\frac{igA}{\omega_0} \sum_{m=-\infty}^{\infty} \left[A_{m0}^{(i)} Y_0(z) H_m(k_0 r_i) + \sum_{q=1}^{\infty} A_{mq}^{(i)} Y_q(z) K_m(k_q r_i) \right] e^{im\theta_i}, \tag{8}$$

where $A_{mq}^{(i)}$ represents the undetermined complex coefficient; $Y_q = \cos k_q(z+d)$ is the z-direction characteristic function for $q \geq 1$; H_m is the m-order Hankel function; K_m is the m-order modified Bessel function of the second kind.

In the calculation, the infinite series in Eqs. (7) and (8) is truncated into the sum of finite terms with upper bounds of summation m_0 and n_0. Equations (7) and (8) can be written in matrix form

$$\varphi_I = -\frac{igA}{\omega_0} \cdot \mathbf{a_j}^T \boldsymbol{\psi}_\mathbf{j}^\mathbf{I}, \tag{9}$$

$$\varphi_{D0-E}^{(i)} = -\frac{igA}{\omega_0} \cdot \mathbf{A_i}^T \boldsymbol{\psi}_\mathbf{i}^\mathbf{D-E}, \tag{10}$$

where the superscript T represents the transposition operator, and the elements of each vector are defined as follows:

$$\mathbf{a_j}(q,m) = \begin{cases} I_j^a e^{im(\pi/2-\beta)} + I_j^b e^{im(-\pi/2+\beta)}, & q = 0, \\ 0, & q \geq 1, \end{cases} \tag{11}$$

$$\boldsymbol{\psi}_\mathbf{j}^\mathbf{I}(q,m) = \begin{cases} Y_0(z) J_m(k_0 r_j) e^{im\theta_j}, & q = 0, \\ Y_q(z) I_m(k_q r_j) e^{im\theta_j}, & q \geq 1, \end{cases}$$

$$\boldsymbol{\psi}_\mathbf{i}^\mathbf{D-E}(q,m) = \begin{cases} Y_0(z) H_m(k_0 r_i) e^{im\theta_i}, & q = 0, \\ Y_q(z) K_m(k_q r_i) e^{im\theta_i}, & q \geq 1, \end{cases} \tag{12}$$

where I_m is the m-order modified Bessel function of the first kind.

Equation (12) can be expressed by the Graf addition theorem of Bessel functions in the local coordinate system of the j-cylinder

$$\boldsymbol{\psi}_\mathbf{i}^\mathbf{D-E}(q,m) = \begin{cases} \sum_{l=-\infty}^{\infty} H_{m-l}(k_0 R_{ij}) e^{i\alpha_{ij}(m-l)} \cdot Y_0(z) J_l(k_0 r_j) e^{il\theta_j}, \\ \quad q = 0, \\ \sum_{l=-\infty}^{\infty} K_{m-l}(k_q R_{ij}) e^{i\alpha_{ij}(m-l)} (-1)^l \cdot Y_q(z) I_l(k_q r_j) e^{il\theta_j}, \\ \quad q \geq 1, \end{cases} \tag{13}$$

where R_{ij} represents the distance between the centers of the i-cylinder and the j-cylinder. Taking the center of i-cylinder as the origin, α_{ij} represents the angle from the positive direction of x axis to the line connecting the center of i-cylinder and the center of j-cylinder in the counterclockwise direction.

Furthermore, it is written in matrix form

$$\boldsymbol{\psi}_\mathbf{i}^\mathbf{D-E} = \mathbf{T_{ij}} \boldsymbol{\psi}_\mathbf{j}^\mathbf{I}, \tag{14}$$

where $\mathbf{T_{ij}}$ represents the coordinate transformation matrix between two different local coordinate systems, defined as follows:

$$\mathbf{T_{ij}}(q,m,l) = \begin{cases} H_{m-l}(k_0 R_{ij}) e^{i\alpha_{ij}(m-l)}, & q = 0, \\ K_{m-l}(k_q R_{ij}) e^{i\alpha_{ij}(m-l)} (-1)^l, & q \geq 1. \end{cases} \tag{15}$$

Thus, the diffraction potential in the exterior region of the i-cylinder represented by Eq. (10) can be written in the local coordinate system of the j-cylinder as

$$\varphi_{D0-E}^{(i)}\big|_j = -\frac{igA}{\omega_0} \cdot \mathbf{A_i}^T \mathbf{T_{ij}} \boldsymbol{\psi}_\mathbf{j}^\mathbf{I}. \tag{16}$$

The total ambient incident wave of cylinder j is composed of the ambient incident wave and the diffracted waves of other cylinders

$$\varphi_I^{(j)} = \varphi_I + \sum_{i=1,i\neq j}^{2N} \varphi_{D0-E}^{(i)}|_j = -\frac{igA}{\omega_0}\cdot\left(\mathbf{a_j}^T + \sum_{i=1,i\neq j}^{2N} \mathbf{A_i}^T\mathbf{T_{ij}}\right)\boldsymbol{\psi}_\mathbf{j}^\mathbf{I}. \tag{17}$$

The total ambient incident wave and the total diffracted wave in the vicinity of cylinder j can be related by its isolated-body inherent diffraction transfer matrix $\mathbf{B_j^E}$ (Kagemoto and Yue, 1986):

$$\mathbf{A_j} = \mathbf{B_j^E}\left(\mathbf{a_j} + \sum_{i=1,i\neq j}^{2N} \mathbf{T_{ij}}^T\mathbf{A_i}\right), \quad j = 1, 2, \ldots, 2N, \tag{18}$$

where $\mathbf{B_j^E}$ is given in Appendix A; the unknown coefficient vector $\mathbf{A_i}$ can be obtained by solving Eq. (18). $\mathbf{A_i}$ is a $(n_0+1)(2m_0+1)$-by-1 matrix. Therefore, for the diffraction problem, the total velocity potential in the exterior region of cylinder j can be obtained as follows:

$$\varphi_{ID-E}^{(j)} = -\frac{igA}{\omega_0}\cdot\left[\mathbf{A_j}^T\boldsymbol{\psi}_\mathbf{j}^{\mathbf{D-E}} + \left(\mathbf{a_j}^T + \sum_{i=1,i\neq j}^{2N} \mathbf{A_i}^T\mathbf{T_{ij}}\right)\boldsymbol{\psi}_\mathbf{j}^\mathbf{I}\right]. \tag{19}$$

Similarly, the total velocity potential in the core region expressed in the local coordinate of j-cylinder can be written as

$$\varphi_{ID-C}^{(j)} = -\frac{igA}{\omega_0}\cdot\left(\mathbf{a_j}^T + \sum_{i=1,i\neq j}^{2N} \mathbf{A_i}^T\mathbf{T_{ij}}\right)(\mathbf{B_j^C})^T\boldsymbol{\psi}_\mathbf{j}^{\mathbf{D-C}}, \tag{20}$$

where $\mathbf{B_j^C}$ is given in Appendix A, and the component wave vectors of the core region are defined as

$$\boldsymbol{\psi}_\mathbf{j}^{\mathbf{D-C}}(p,m) = \begin{cases} r_j^{|m|}e^{im\theta_j}, & p = 0, \\ I_m(\beta_p r_j)e^{im\theta_j}, & p \geq 1. \end{cases} \tag{21}$$

B. Radiation problem

In this study, each cylinder oscillates sinusoidally with different amplitudes and the same circular frequency ω_0 in undisturbed water. In the context of linear water waves, the hydrodynamic response of the yaw can be ignored. Therefore, each cylinder in the array has five degrees of freedom, namely, surge, sway, heave, roll, and pitch. The instantaneous displacement of cylinder j can be expressed as

$$\Xi_s^{(i)}(t) = \mathrm{Re}\left\{\zeta_s^{(i)}e^{-i\omega_0 t}\right\}. \tag{22}$$

In the local coordinate system of cylinder i, the radiation potential in the exterior region, generated by the oscillating of cylinder i with complex amplitude $\zeta_s^{(i)}$ in the direction of the sth degree of freedom, can be written as

$$\varphi_{Rs-E}^{(i)} = -i\omega_0\zeta_s^{(i)}\sum_{m=-\infty}^{\infty}\left[R_{m0s}^{(i)}Y_0(z)H_m(k_0r_i) + \sum_{q=1}^{\infty}R_{mqs}^{(i)}Y_q(z)K_m(k_qr_i)\right]e^{im\theta_i}. \tag{23}$$

Here, $R_{mqs}^{(i)}$ is the radiation characteristic of an isolated cylinder

$$R_{mqs}^{(i)} = \begin{cases} \dfrac{D_{R0m}^s\cosh k_0 d}{H_m'(k_0a_i)N_0^{1/2}}, & q = 0, \\ \dfrac{D_{Rqm}^s}{K_m'(k_qa_i)N_q^{1/2}}, & q > 0, \end{cases} \tag{24}$$

where D_{Rqm}^s is given in Appendix A. N_0 and N_q are

$$N_0 = \frac{1}{2}\left(1 + \frac{\sinh 2k_0 d}{2k_0 d}\right), \quad N_q = \frac{1}{2}\left(1 + \frac{\sin 2k_q d}{2k_q d}\right). \tag{25}$$

Equation (23) can be written in the form of a matrix and can be further expressed in the local coordinate system of cylinder j using the coordinate transformation matrix $\mathbf{T_{ij}}$,

$$\varphi_{Rs-E}^{(i)} = -i\omega_0\zeta_s^{(i)}\mathbf{R_{is}}^T\boldsymbol{\psi}_\mathbf{i}^{\mathbf{D-E}} = -i\omega_0\zeta_s^{(i)}\mathbf{R_{is}}^T\mathbf{T_{ij}}\boldsymbol{\psi}_\mathbf{j}^\mathbf{I}. \tag{26}$$

When each cylinder oscillates with five degrees of freedom, the diffraction potential in the exterior region of cylinder i generated by the radiation waves and diffraction waves of other cylinders in the array except cylinder i can be written as follows:

$$\varphi_{D1-E}^{(i)} = \sum_{m=-\infty}^{\infty}\left[A_{Rm0}^{(i)}Y_0(z)H_m(k_0r_i) + \sum_{q=1}^{\infty}A_{Rmq}^{(i)}Y_q(z)K_m(k_qr_i)\right]e^{im\theta_i}. \tag{27}$$

In the calculation, the infinite series in Eq. (27) is truncated into the sum of finite terms with upper bounds of summation m_0 and n_0. Similar to Eq. (26), Eq. (27) can be rewritten in matrix form

$$\varphi_{D1-E}^{(i)} = \mathbf{A_{Ri}}^T\boldsymbol{\psi}_\mathbf{i}^{\mathbf{D-E}} = \mathbf{A_{Ri}}^T\mathbf{T_{ij}}\boldsymbol{\psi}_\mathbf{j}^\mathbf{I}, \tag{28}$$

where the coefficient vector $\mathbf{A_{Ri}}$ is to be determined.

The total incident wave of cylinder j is composed of radiated and diffracted waves of other cylinders

$$\begin{aligned}&\sum_{i=1,i\neq j}^{2N}\varphi_{Rs-E}^{(i)}|_j + \sum_{i=1,i\neq j}^{2N}\varphi_{D1-E}^{(i)}|_j \\ &= \sum_{i=1,i\neq j}^{2N}\sum_{s=1}^{5}\left(-i\omega_0\zeta_s^{(i)}\mathbf{R_{is}}^T\right)\mathbf{T_{ij}}\boldsymbol{\psi}_\mathbf{j}^\mathbf{I} + \sum_{i=1,i\neq j}^{2N}\mathbf{A_{Ri}}^T\mathbf{T_{ij}}\boldsymbol{\psi}_\mathbf{j}^\mathbf{I} \\ &= \sum_{i=1,i\neq j}^{2N}\left[\sum_{s=1}^{5}\left(-i\omega_0\zeta_s^{(i)}\mathbf{R_{is}}^T\right) + \mathbf{A_{Ri}}^T\right]\mathbf{T_{ij}}\boldsymbol{\psi}_\mathbf{j}^\mathbf{I}.\end{aligned} \tag{29}$$

Similar to Eq. (18), the total radiated waves in the vicinity of cylinder j can be related by its isolated-body inherent diffraction transfer matrix $\mathbf{B_j^E}$ (Kagemoto and Yue, 1986),

$$\mathbf{A_{Rj}} = \mathbf{B_j^E}\sum_{i=1,i\neq j}^{2N}\mathbf{T_{ij}}^T\left[\sum_{s=1}^{5}\left(-i\omega_0\zeta_s^{(i)}\mathbf{R_{is}}\right) + \mathbf{A_{Ri}}\right], \quad j = 1, 2, \ldots, 2N, \tag{30}$$

where $\mathbf{A_{Rj}}$ is a $(n_0+1)(2m_0+1)$-by-1 matrix.

In the radiation problem, the total velocity potential in the exterior region of cylinder j can be written as

$$\varphi_{RD-E}^{(j)} = \left[\sum_{s=1}^{5}\left(-\mathrm{i}\omega_0\zeta_s^{(j)}\mathbf{R_{js}}^T\right) + \mathbf{A_{Rj}}^T\right]\boldsymbol{\psi}_{\mathbf{j}}^{\mathbf{D-E}} + \sum_{i=1,i\neq j}^{2N}\left[\sum_{s=1}^{5}\left(-\mathrm{i}\omega_0\zeta_s^{(i)}\mathbf{R_{is}}^T\right) + \mathbf{A_{Ri}}^T\right]\mathbf{T_{ij}}\boldsymbol{\psi}_{\mathbf{j}}^{\mathbf{I}}. \quad (31)$$

The total velocity potential in the core region of cylinder j can also be obtained as follows:

$$\varphi_{RD-C}^{(j)} = \sum_{s=1}^{5}\left[-\mathrm{i}\omega_0\zeta_s^{(j)}\varphi_{Rs-C}^{j}(r_j,\theta_j,z)\right] + \left\{\sum_{i=1,i\neq j}^{2N}\left[\sum_{s=1}^{5}\left(-\mathrm{i}\omega_0\zeta_s^{(i)}\mathbf{R_{is}}^T\right) + \mathbf{A_{Ri}}^T\right]\mathbf{T_{ij}}\right\}(\mathbf{B_j^C})^T\boldsymbol{\psi}_{\mathbf{j}}^{\mathbf{D-C}}, \quad (32)$$

$\varphi_{Rs-C}^{(j)}$ is the radiation potential in the core region of cylinder j, defined as

$$\varphi_{Rs-C}^{(j)}(r_j,\theta_j,z) = \sum_{m=-\infty}^{\infty}\left\{\begin{array}{l} C_{R0m}^{s}\left(r_j/a_j\right)^{|m|}X_0(z) \\ +\sum_{p=1}^{\infty}C_{Rpm}^{s}\dfrac{I_m\left(\beta_p r_j\right)}{I_m\left(\beta_p a_j\right)} \\ \times\cos\left[\beta_p(z+d)\right] + \Lambda_s\lambda_{ms}\end{array}\right\}e^{\mathrm{i}m\theta_j}, \quad (33)$$

where coefficients C_{Rpm}^{s}, Λ_s, and λ_{ms} are defined in detail in Appendix A.

C. Hydrodynamic forces and amplitudes of each buoy in the cylindrical array

The relationship between the spatial pressure and velocity potential in the vicinity of cylinder j is as follows:

$$\mathcal{P}^{(j)} = \mathrm{i}\rho\omega\varphi^{(j)}|_{wetted\ surface}. \quad (34)$$

By integrating the pressure $\mathcal{P}^{(j)}$ on the wetted surface of the cylinder, the total hydrodynamic force and moment in the pth mode of cylinder j are obtained as follows:

$$\mathcal{F}_{Hp}^{(j)} = \left\{\begin{array}{ll}\int\mathcal{P}^{(j)}\mathbf{n}dS, & p=1,\ 2,\ 3, \\ \int\mathcal{P}^{(j)}(\mathbf{r}\times\mathbf{n})dS, & p=4,\ 5,\end{array}\right. \quad (35)$$

where $\mathbf{r}$ is the position vector pointing from the center of mass to the integration point; and $\mathbf{n}$ is the unit normal vector of wetted surface pointing into the body, defined as follows:

$$\mathbf{n} = \left\{\begin{array}{ll}(-\cos\theta_j, -\sin\theta_j, 0), & -h\le z\le 0, r=a, \\ (0,0,1), & z=-h, 0\le r\le a.\end{array}\right. \quad (36)$$

Substituting Eqs. (19), (20), (31), and (32) into Eqs. (34) and (35) yields that

$$F_{Hs}^{(j)} = F_{IDs}^{(j)} + \sum_{i=1}^{2N}\sum_{p=1}^{5}F_{RDsp}^{(ji)}\zeta_p^i = F_{IDs}^{(j)} + \sum_{i=1}^{2N}\sum_{p=1}^{5}\left(-\omega^2\cdot a_{sp}^{(ji)}\zeta_p^i + \sum_{i=1}^{2N}\sum_{p=1}^{5}-i\omega\cdot b_{sp}^{(ji)}\zeta_p^i\right), \quad (37)$$

where $\mathcal{F}_{IDp}^{(j)}$ denotes the excitation force of cylinder j caused by the diffraction problem; $F_{RDsp}^{(ji)}$ represents the radiation force on cylinder j in the sth mode due to the oscillating of cylinder i with unit amplitude in the pth mode. $a_{sp}^{(ji)}$ and $b_{sp}^{(ji)}$ are added mass and damping, respectively. The specific forms of the hydrodynamic force of cylinder j induced by the oscillating of each cylinder are shown in Appendix B.

The steady-state motion of cylinder j in the s mode can be described by applying Newton's second law equation at the center of mass

$$\sum_{p=1}^{5}\sum_{i=1}^{2N}\left[-\omega^2\left(M_s^{(j)} + a_{sp}^{(ji)}\right) - i\omega\left(b_{sp}^{(ji)} + \lambda_s^{(j)}\right) + \left(\delta_s^{(j)} + k_s^{(j)}\right)\right]\zeta_p^{(i)} = F_{IDs}^{(j)} \quad (j=1,2,\ldots,2N; s=1,2,\ldots,5), \quad (38)$$

$M_s^{(j)}$, $\lambda_s^{(j)}$, $\delta_s^{(j)}$, and $k_s^{(j)}$ have non-zero values only if $i=j$ and $s=p$. λ_p^j and δ_p^j denote the artificial damping and spring coefficient of cylinder j in the pth mode, respectively, which are induced by the mooring system or the power takeoff system (PTO).

$M_p^{(j)}$ is the mass ($p=1, 2, 3$) and moment of inertia ($p=4, 5$) of cylinder j, defined as

$$M_p^{(j)} = \left\{\begin{array}{ll}\rho g\pi a_j^2 h_j & p=1,2,3, \\ \rho g\pi a_j^2 h_j\left[-a_j^2/4 + (h_j+h_{upj})^2/12 + \bar{z}_j^2\right] & p=4,5.\end{array}\right. \quad (39)$$

$k_p^{(j)}$ denotes the hydrostatic restoring stiffness

$$k_p^{(j)} = \left\{\begin{array}{ll}0, & p=1,2, \\ \rho g\pi a_j^2, & p=3, \\ -\rho g\pi a_j^2\left(\dfrac{h_j^2}{2} + \bar{z}_j h_j - \dfrac{a_j^2}{4}\right), & p=4,5.\end{array}\right. \quad (40)$$

By solving the linear equation system (38), the amplitudes of all cylinders can be obtained, and the hydrodynamic problem is solved. Obviously, since the equivalent hydrodynamic model is symmetrical concerning the original wall, the oscillation amplitudes of cylinder j and cylinder $N+j$ are equal.

D. energy extraction performance

In this paper, each buoy only extracts energy in the heave mode, as shown in Fig. 1(a). The power takeoff system (PTO) consists of spring and damping. For simplicity, the restoring force and damping force are linearly related to the displacement and velocity of the buoy. Therefore, the mean power extracted by the buoy j oscillating with amplitude $\zeta_3^{(j)}$ in the heave mode is (Falnes, 2002)

$$P^j = \frac{1}{2}\omega_0^2\lambda_3^j|\zeta_3^{(j)}|^2. \quad (41)$$

The total power of the WEC array should be

$$P_a = \sum_{j=1}^{N}P^j. \quad (42)$$

TABLE I. Heave amplitudes of the five cylinders for $L=4a$, $c=4a$, $h=a$, $k_0a=0.4$, and $\beta=\pi/4$.

$\lvert\zeta_3^{(j)}\rvert/A$	$j=1$	$j=2$	$j=3$	$j=4$	$j=5$
$m_0=5$, $n_0=5$	1.064 93	1.040 48	1.002 94	0.900 28	0.869 33
$m_0=10$, $n_0=5$	1.064 93	1.040 48	1.002 94	0.900 28	0.869 33
$m_0=5$, $n_0=15$	1.044 74	1.020 57	0.982 89	0.879 95	0.849 79
$m_0=5$, $n_0=20$	1.042 00	1.018 14	0.980 53	0.878 18	0.848 15
$m_0=5$, $n_0=25$	1.043 72	1.019 57	0.981 88	0.878 94	0.848 81
$m_0=5$, $n_0=50$	1.043 43	1.019 26	0.981 56	0.878 56	0.848 43

Capture width is widely used to evaluate the performance of the WEC array and is defined as

$$w=\sum_{i=1}^{N} w_i=\frac{\sum_{i=1}^{N} P^{(i)}}{P_I}=\frac{P_a}{P_I}, \tag{43}$$

where P_I denotes the average energy-flux per unit width across a vertical plane perpendicular to the wave direction, which is

$$P_I=\frac{1}{2}\rho g A^2\cdot\frac{\omega_0}{2k_0}\left(1+\frac{2k_0d}{\sinh 2k_0d}\right). \tag{44}$$

The mechanical damping of the PTO system of buoy j is chosen as the optimal damping of a corresponding isolated buoy, that is,

$$\lambda_3^j=\sqrt{b_{\mathrm{iso},3}^j+\left[\omega_0\left(M_3^j+a_{\mathrm{iso},3}^j\right)-\left(k_3^j+\delta_3^j\right)/\omega_0\right]}, \tag{45}$$

where $a_{\mathrm{iso},3}^j$ and $b_{\mathrm{iso},3}^j$, respectively, represent the added mass and radiation damping of the heaving mode of an isolated buoy in an open water domain, which can be obtained by the methods introduced in Secs. II B and II C of this paper.

Additionally, an indicator W_{wall} is used to evaluate the reflection effect of a vertical wall, which is

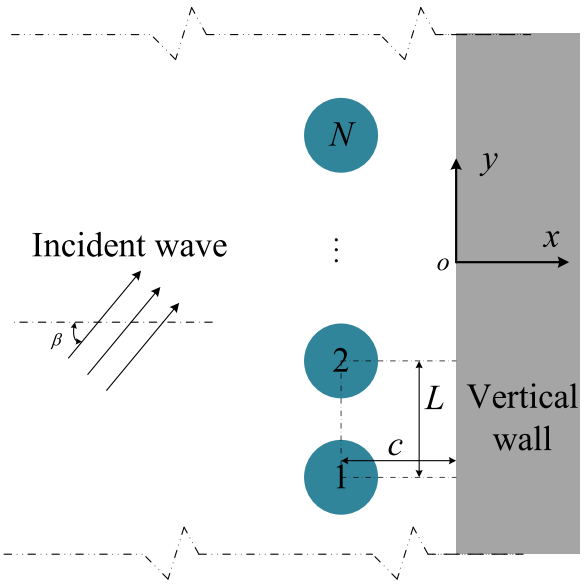

FIG. 4. Plane layout of N buoys near a vertical wall.

$$W_{\mathrm{wall}}=\frac{w}{w_0}, \tag{46}$$

where w_0 denotes the capture width of the corresponding buoys in an open water domain.

Similarly, the effect of hydrodynamic interaction among buoys on energy extraction is evaluated using the $\bar{q}$ factor

$$\bar{q}=\frac{\sum_{i=1}^{N} P^{(i)}}{N\times P^{iso}}, \tag{47}$$

where P^{iso} denotes the optimal power of an isolated buoy near a vertical wall; $\bar{q}>1$ indicates that hydrodynamic interaction plays a constructive role in energy extraction. In contrast, $\bar{q}<1$ means that a destructive effect is induced by the hydrodynamic interaction.

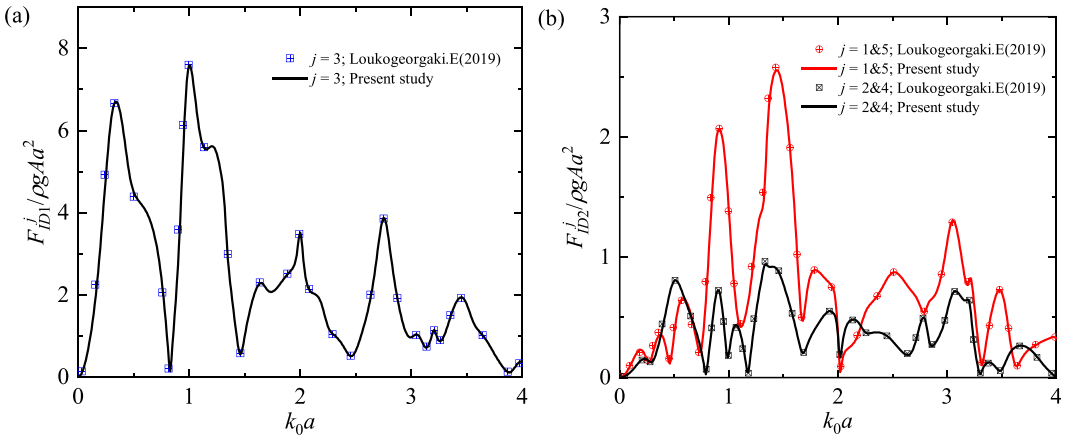

FIG. 5. Exciting force of the five cylinders; (a) surge; (b) sway.

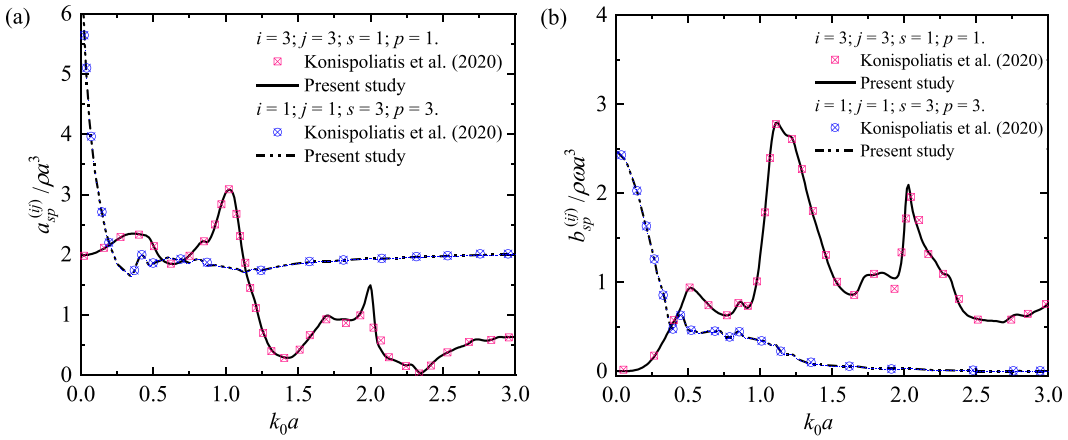

FIG. 6. Hydrodynamic coefficients of the five cylinders: (a) add mass; (b) radiation damping.

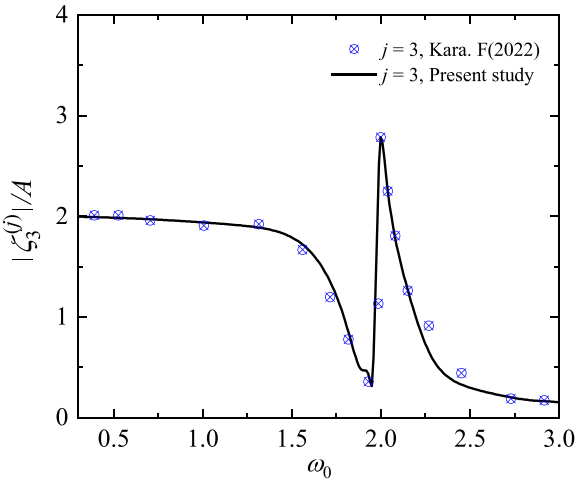

FIG. 7. Heave amplitudes of the five cylinders.

III. VERIFICATION WITH THEORETICAL RESULTS

The semi-analytical method established in Sec. II can accurately and quickly calculate the hydrodynamic interaction of the cylindrical WEC array near a vertical wall. In order to achieve the expected accuracy, two important truncation numbers should be carefully considered in Eqs. (18) and (30). The first truncation number m_0 is related to the trigonometric function, and the other truncation term parameter n_0 is related to the vertical characteristic function. For the diffraction and radiation problems of truncated cylinder groups in an open water domain, a large number of calculation results have shown (Zeng *et al.*, 2016; 2022d) that using the truncation numbers $m_0 = 5$ and $n_0 = 25$ can make the relative error of the calculation results of exciting force, added mass, damping, and response amplitude within 1%. For the problem related to the amplitudes of a cylinder array in the front of a vertical wall, there are hardly any published results on the influence of the upper bounds of the summation on the convergence. According to our computations on the amplitudes of independently oscillating floating cylinders with five DOFs near a vertical wall, the ratio of draught to water depth has a remarkable impact on the convergence. The smaller the ratio of the draft to water depth is, the more terms for

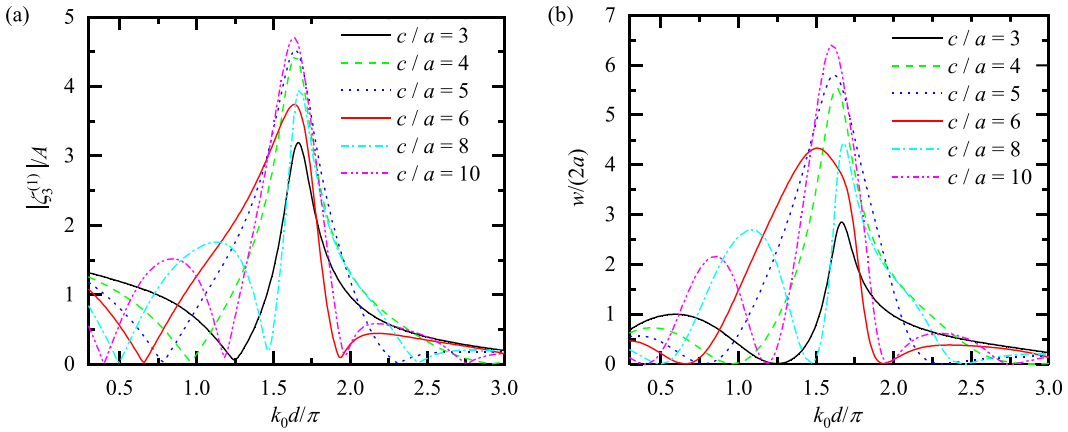

FIG. 8. Heave amplitude and capture width of the two buoys for $c = 5a$ and $\beta = 0$: (a) heave amplitudes; (b) capture width.

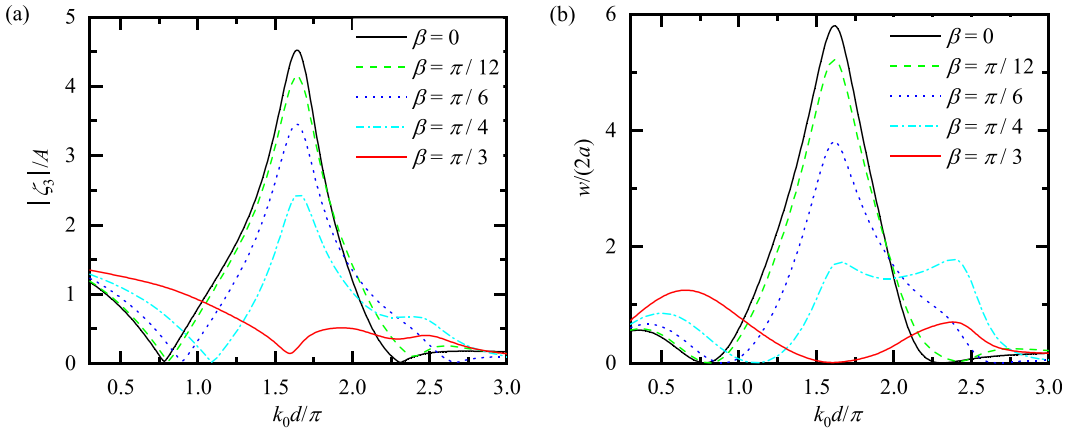

FIG. 9. Heave amplitude and capture width of the two buoys for $L = 6a$ and $c = 5a$: (a) heave amplitude; (b) capture width.

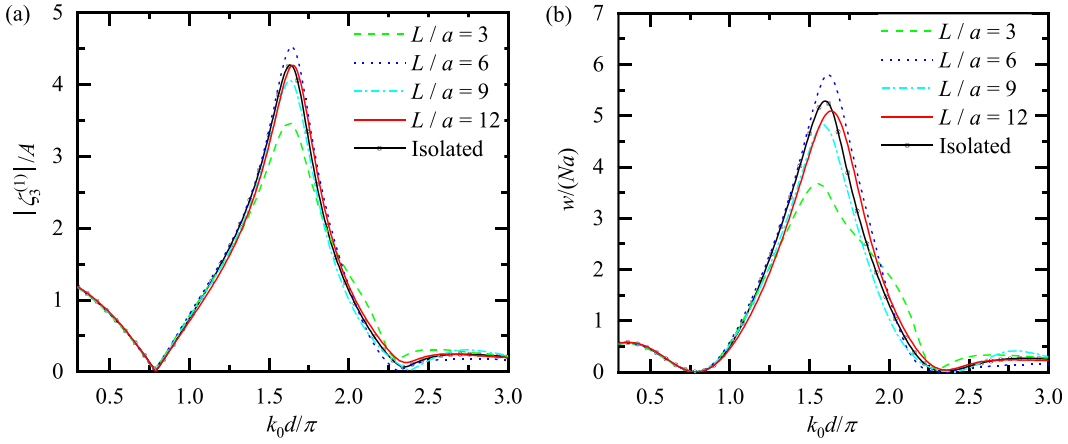

FIG. 10. Heave amplitude and capture width of the two buoys for $c = 5a$ and $\beta = 0$: (a) heave amplitude; (b) capture width.

convergence are required. The convergence is evaluated by comparing the calculated results obtained when the upper bounds of summation are small with those when the upper bounds of summation are large enough. To visually display the convergence, we provide some amplitude results of five cylinders in Table I. The arrangement of the array is shown in Fig. 4. The calculation results revealed that for $m_0 > 5$, even if we continue to increase the upper bound of summation m_0, there is no significant change (the maximum error between $m_0 = 5$ and $m_0 = 10$ is about 0.0002%). Therefore, taking m_0 as 5 is enough. Similarly, increasing n_0 does not significantly change the calculation results when $n_0 > 25$ (the maximum error between $n_0 = 25$ and $n_0 = 50$ is about 0.03%). So, it is reasonable to take n_0 as 25. In this paper, $m_0 = 5$ and $n_0 = 25$ is adopted. For the cases we conducted, computations show good convergence results for all considered wavenumbers.

The semi-analytical method proposed in Sec. II is verified before performing the hydrodynamic analysis. Regarding the diffraction problem of the cylindrical WEC array near a vertical wall under the

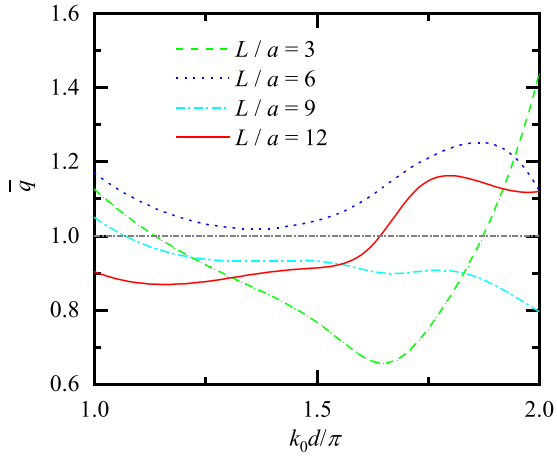

FIG. 11. Interaction factor $\bar{q}$.

action of the ambient incident wave, Loukogeorgaki and Chatjigeorgiou (2019) used an analytical method to calculate the excitation force of an array composed of five cylinders. The arrangement of the array is shown in Fig. 4. The total number of cylinders is $N = 5$. Each cylinder has a radius of a and a draught of $h = 2a$. The water depth is $d = 10a$. The spacing between the center of adjacent cylinders is $L = 4a$. The vertical distance between a vertical wall and the center of each buoy is $c = 4a$. The heading angle of the ambient incident wave is $\beta = 0$. As shown in Fig. 5, the results of the present study are in good agreement with those of Loukogeorgaki and Chatjigeorgiou (2019).

In addition, a comparison is provided for the added mass and radiation damping of the five cylinders near a vertical wall.

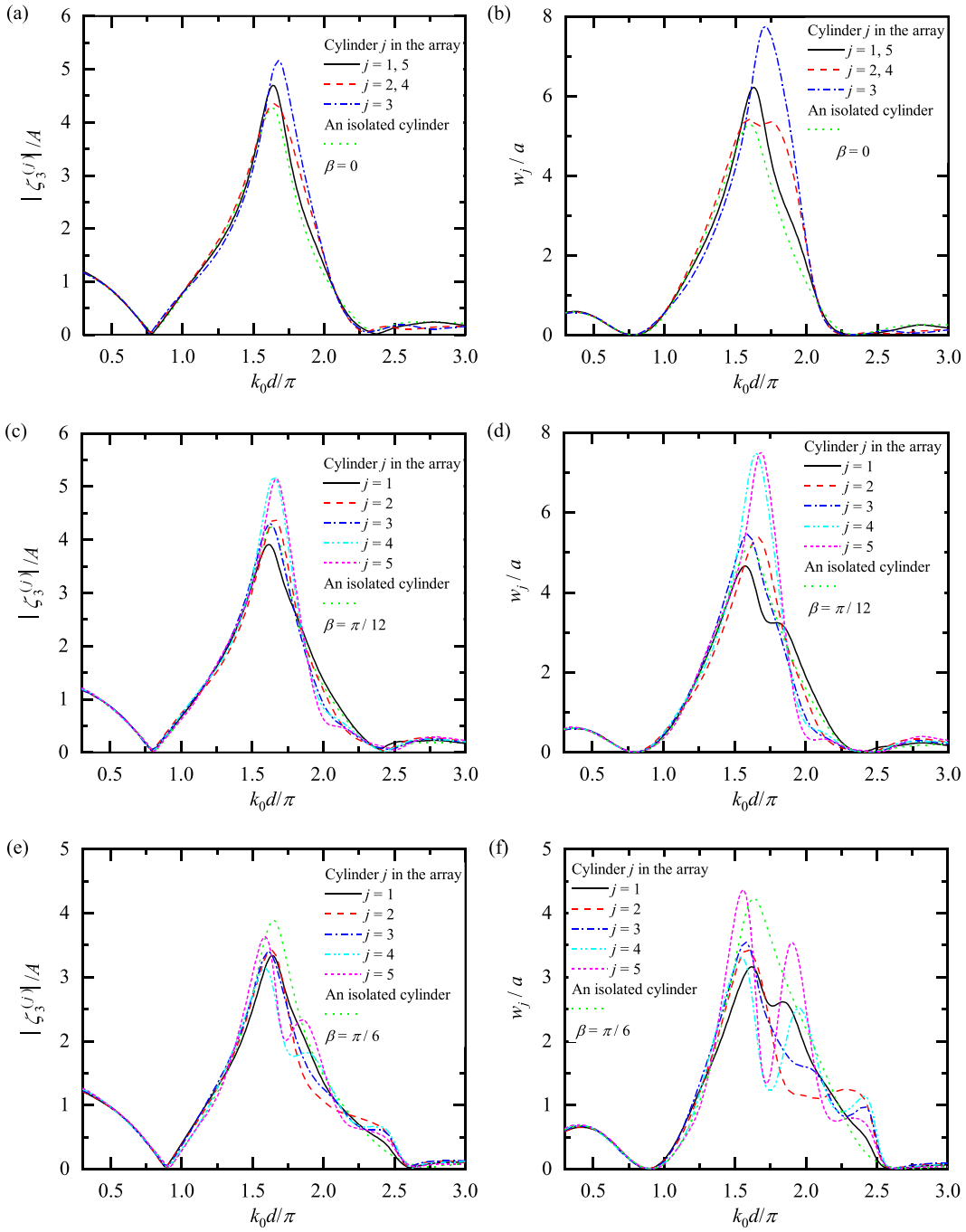

FIG. 12. Heave amplitude (a), (c), (e), (g), and (i) and capture width (b), (d), (f), (h), and (j) of the five buoys with different incident angles for $L/a = 6$ and $c/a = 5$.

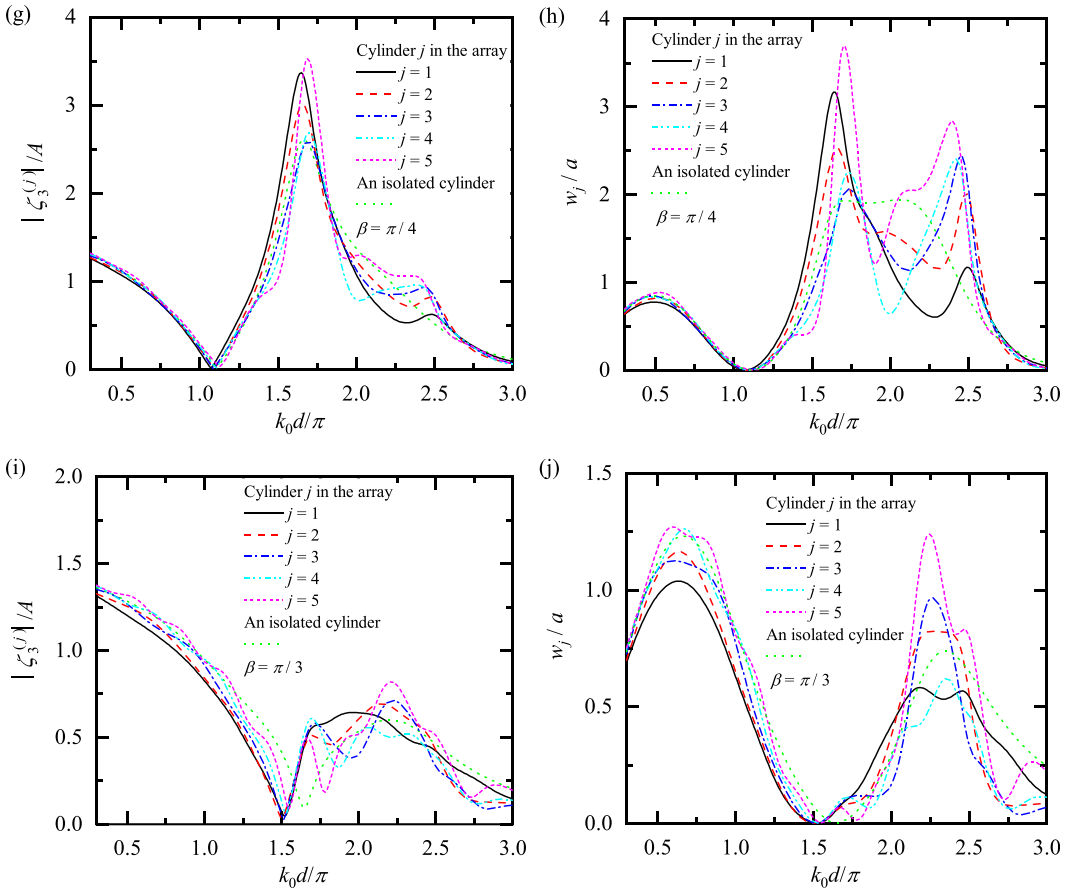

FIG. 12. (*Continued.*)

Konispoliatis *et al.* (2020) used a semi-analytical method to investigate the hydrodynamic results of five cylinders in three different layouts near a vertical wall. The layout shown in Fig. 4 is chosen for comparison. Each cylinder has a radius of a and a draught of $h = 0.5a$. $L = 8a$, $c = 4a$, $d = 2a$, and $\beta = 0$. As shown in Fig. 6, the results of the present study are in good agreement with those of Konispoliatis *et al.* (2020).

Kara (2022) used the time-dependent boundary integral equation method to calculate the amplitudes of five cylinders near a vertical wall. The array layout is shown in Fig. 4. Each cylinder has a radius a and a draught of $h = 2a$. $L = 4a$, $c = 3.5a$, $d = 10a$, and $\beta = 0$. Each cylinder in the array only oscillates in the heave mode, and the PTO damping is the optimal damping of an isolated cylinder at the resonance frequency ($\omega_0 = 2.0$). The comparison between the results of the present study and those of Kara (2022) is shown in Fig. 7, demonstrating a significant agreement.

IV. HYDRODYNAMIC PERFORMANCES

In this section, an equidistant linear array consisting of N identical buoys is considered, the plane layout is shown in Fig. 4. Each cylinder has a radius of a and a draught of $h = a$. The water depth is $8a$. For convenience, all buoys in the array have the same PTO characters. This study adopts the real tuning (Child and Venugopal, 2010). The damping λ of each buoy adopts the optimal damping calculated by Eq. (45) and the elastic stiffness set to $\delta = 0$. Each buoy only moves and extracts energy in the heave mode. The exciting force, heave amplitude, and capture width according to different parameters such as c, L, the number of buoys N, and the incident angle β are investigated.

A. Two buoys

In this subsection, the influence of c, L, and β on the hydrodynamic performances of the two identical cylindrical buoys near a vertical wall is investigated. Figure 4 shows the detailed layout of the two buoys. It can be seen from Fig. 8 that the change of c/a has an obvious impact on the heave amplitude and capture width. The larger the spacing between each buoy and a vertical wall, the more drastic and rapid the variation curve of energy capture width changes with wavenumber. In other words, the energy capture performance of the WEC device is not stable enough when the frequency variation range of the wave field is broad. As shown in Fig. 9, the heave amplitude and capture width are sensitive to the incident angle β. As the incident angle increases, the maximum values of heave amplitude and capture width gradually decrease. It can be seen from Fig. 10 that the maximum values of heave amplitude and capture width occur with $L/a = 6$. When the spacing between the two buoys is large enough (e.g., $L/a = 12$), the heave amplitude and capture width are very close to that of an isolated buoy,

which means that the hydrodynamic interaction has little impact on the energy extraction performance.

Figure 11 shows the calculation results of the interaction factor $\bar{q}$. The displayed frequency range is $\pi < k_0 d < 2\pi$, in which the buoys have a larger heave amplitude and capture width. It can be seen from Fig. 15 that the interaction factor with different L/a has an obvious discrepancy, and there is no trend of monotonically changing with L/a. For $L/a = 6$, the interaction factors are greater than 1 within the entire frequency range, i.e., hydrodynamic interaction is constructive to wave energy capture. Therefore, in order to achieve higher wave energy extraction performance of the WEC array, too large or too small spacing is disadvantageous, and the buoys need to be installed at a suitable position based on the local ambient wave and terrain conditions.

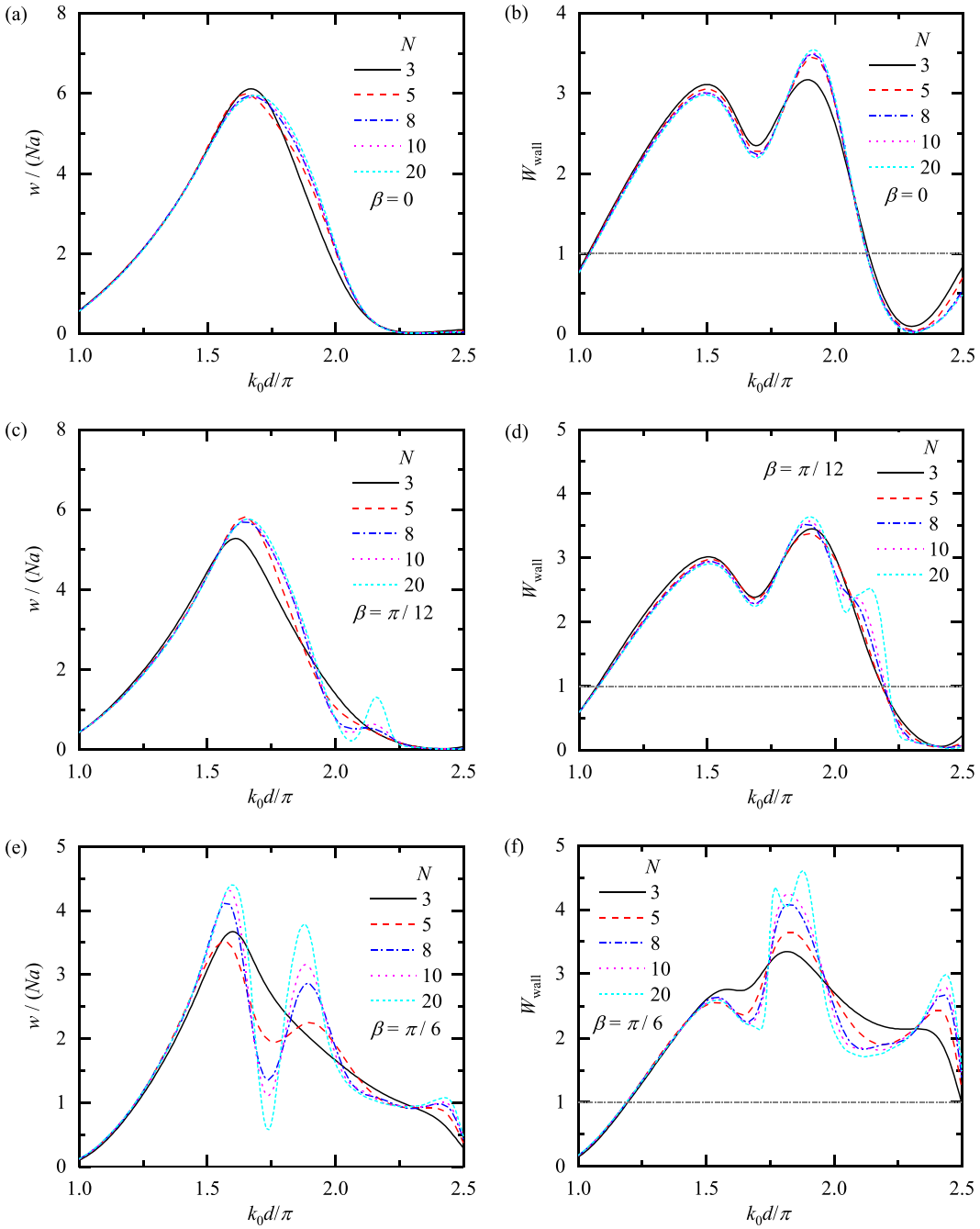

FIG. 13. Average capture width (a), (c), (e), (g), and (i) and effect indicator of the wall reflection (b), (d), (f), (h), and (j) of N buoys for $L/a = 6$ and $c/a = 5$.

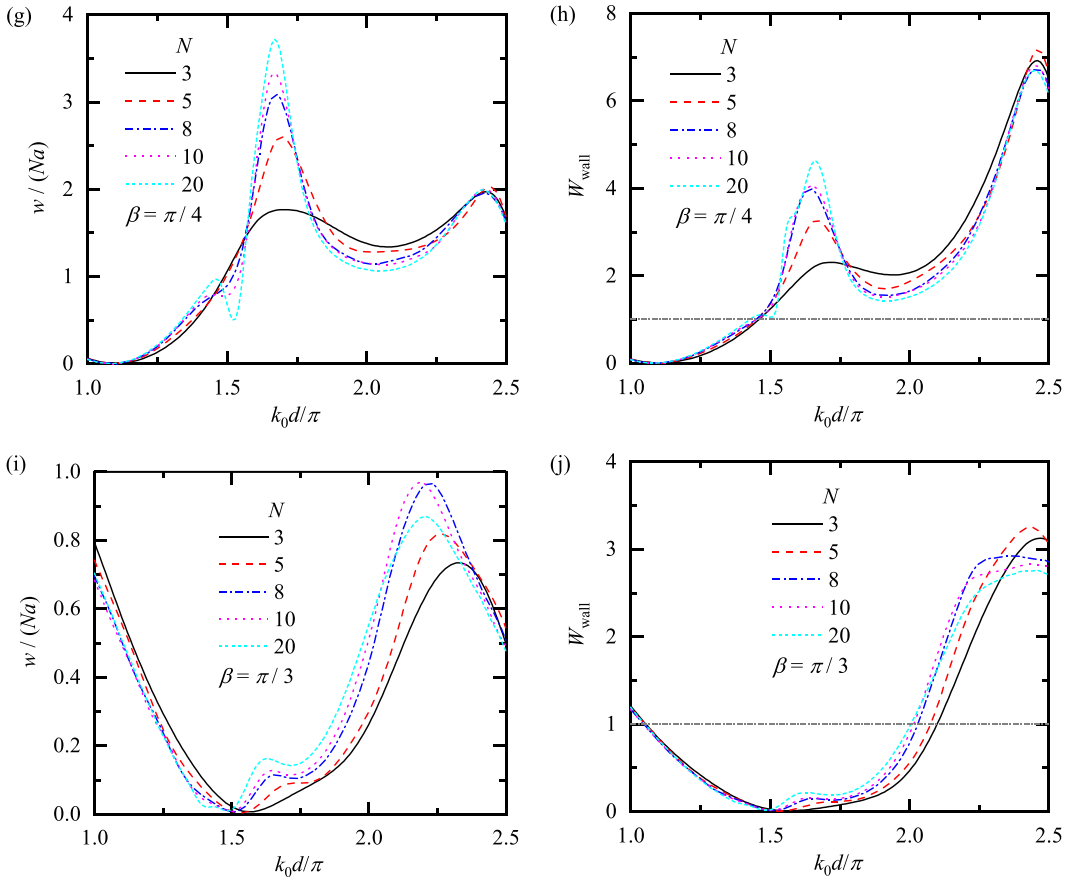

FIG. 13. (*Continued.*)

B. A group of buoys

An equidistant linear array consisting of N identical buoys is investigated in this subsection. The plane layout is shown in Fig. 4. Figure 12 shows the results of the heave amplitude and capture width of five buoys with five different incident angles (i.e., $\beta = 0$, $\beta = \pi/12$, $\beta = \pi/6$, $\beta = \pi/4$, and $\beta = \pi/3$). For comparison, Fig. 12 also shows the corresponding results for an isolated buoy. Owing to the hydrodynamic interaction of five buoys in the array, the heave amplitude and

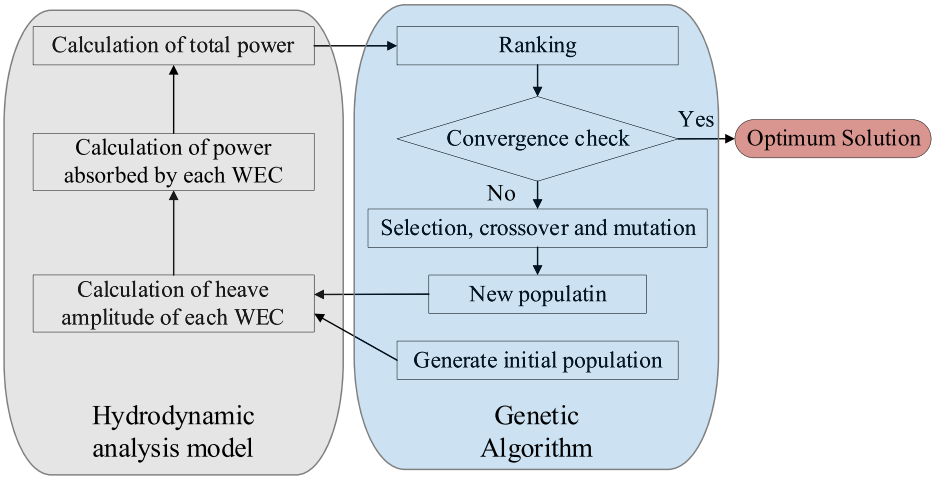

FIG. 14. Flow chart of genetic algorithm program for the layout optimization of the WEC array.

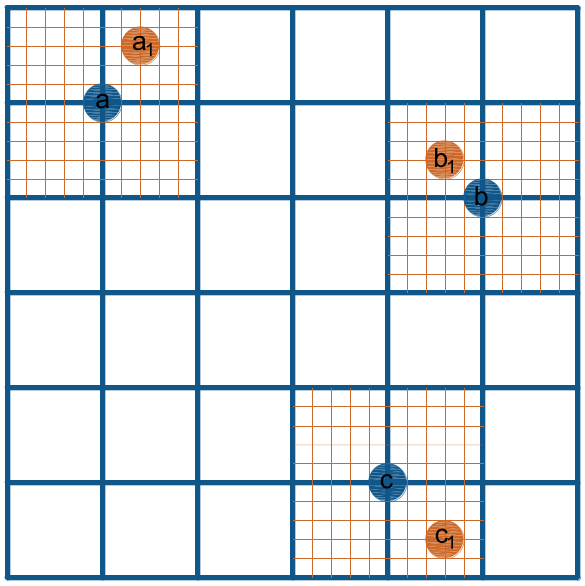

FIG. 15. Example of multi-level optimization method.

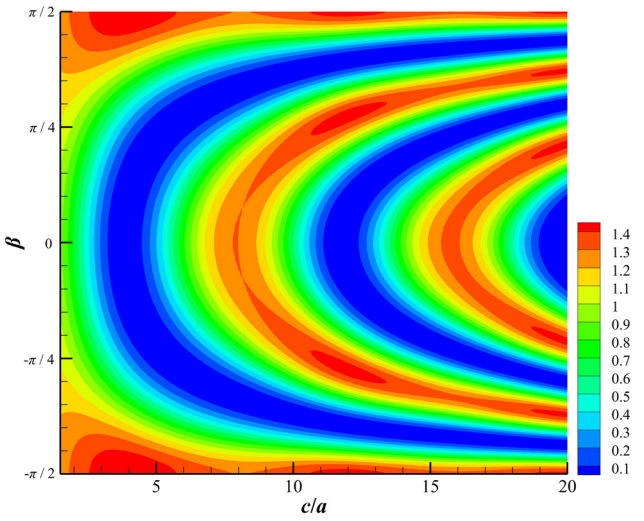

FIG. 16. Contour plot of the capture width of an isolated WEC for $k_0a = 0.4$.

capture width of each buoy are obviously different. The energy extraction performance of the third buoy (i.e., the middle buoy of the array) is the best with the incident angle of $\beta = 0$. As the incident angle increases, the peak capture width of the third buoy gradually decreases, and the peak capture width of the fifth buoy (the most downstream buoy) gradually increases. For $\beta = \pi/12$, the capture widths of the forth buoy and fifth buoy both occur peaks, which shows that the hydrodynamic interaction has a constructive effect on the energy extraction performance. However, for $\beta = \pi/3$, the capture widths of all buoys are less than 1 within the frequency range of $\pi < k_0d < 2.2\pi$, which

TABLE II. Genetic algorithm parameters for cases 1–6.

	Case 1	Case 2	Case 3	Case 4	Case 5	Case 6
N (number of WEC)	2	3	4	5	6	7
S_m^1 (grid size)	a	a	a	a	a	a
S_m^2 (grid size)	0.1 a	0.1 a	0.1 a	0.1 a	0.1 a	0.1 a
N_n (number of nodes)	61	61	61	61	61	61
N_g (maximum number of iterations)	200	200	200	200	200	200
N_p (population size)	300	300	300	300	300	300
R_s (selection rate)	0.1	0.1	0.1	0.1	0.1	0.1
R_m (mutation rate)	0.2	0.2	0.2	0.2	0.2	0.2

TABLE III. First-level optimization results for cases 1–6.

	Case 1	Case 2	Case 3	Case 4	Case 5	Case 6
Coordinates (a)	(−15.0, 0.0), (−15.0, −24.0)	(−39.0, 0.0), (−24.0, 36.0), (−24.0, −36.0)	(−24.0, 18.0), (−24.0, −51.0), (−39.0, −18.0), (−39.0, 51.0)	(−24.0, 0.0), (−24.0, 69.0), (−39.0, 33.0), (−24.0, −69.0), (−39.0, −33.0)	(−15.0, 10.0), (−24.0, 34.0), (−39.0, 67.0), (−15.0, −11.0), (−24.0, -38.0), (−39.0, −68.0)	(−15.0, 0.0), (−24.0, 81.0), (−24.0, 27.0), (−30.0, 51.0), (−24.0, −81.0), (−24.0, −27.0), (−30.0, −51.0)
P_a(kW)	66.017	108.501	145.697	184.909	220.014	238.471
$w/(Na)$	2.670	2.925	2.946	2.991	2.967	2.755

TABLE IV. Second-level optimization results for cases 1–6.

	Case 1	Case 2	Case 3	Case 4	Case 5	Case 6
Coordinates (a)	(−15.7, 0.0), (−15.7, −23.9)	(−39.1, 0.0), (−23.5, 35.9), (−23.5, −35.9)	(−23.5, 17.8), (−23.5, −52.1), (−39.2, -17.8), (−39.2, 52.1)	(−23.5, 0.0), (−23.5, 69.8), (−39.2, 34.2), (−23.5, −69.8), (−39.2, −34.2)	(−15.7, 10.6), (−23.6, 35.9), (−39.3, 66.8), (−15.7, −10.6), (−23.6, −35.9), (−39.3, −66.8)	(−15.7, 0.0), (−23.5, 81.0), (−23.5, 26.7), (−31.5, 51.6), (−23.5, −81.0), (−23.5, −26.7), (−31.5, −51.6)
P_a (kW)	71.088	111.162	150.385	191.196	231.425	271.559
$w/(Na)$	2.875	2.997	3.041	3.093	3.120	3.138

indicates that the hydrodynamic interaction among buoys has a destructive effect on the energy extraction performance of the WEC array.

As is well known, the performance criteria of the WEC array should depend on the total energy extracted by all buoys or the mean energy extracted by each buoy. In order to examine the effect of N (the number of buoys) on the energy extraction performance of the WEC array, an equidistant linear array consisting of 3, 5, 8, 10, and 20 buoys is considered. With five different incident angles (i.e., $\beta = 0$, $\beta = \pi/12$, $\beta = \pi/6$, $\beta = \pi/4$, and $\beta = \pi/3$), the calculated results of the average capture width $w/(Na)$ and effect indicator of the wall reflection W_{wall} are plotted in Fig. 13. As shown in the figure, the appreciable effect N is mainly within the frequency range of $1.5\pi < k_0 d < 2.4\pi$, and the effect can be negligible for other frequencies. For the incidence angle of $\beta = 0$, the influence of N is weak. However, as the incident angle increases, the impact of N becomes more apparent. For example, the average capture width of the WEC array with three buoys is 4.9 times that of the WEC array with twenty buoys when $\beta = \pi/6$, $k_0 d = 1.74\pi$. Therefore, the influence of N needs to be carefully examined when designing the WEC array. Compared with the WEC array in an open wave domain, obvious amplification of energy extraction performance is induced by a vertical wall over a wider range of frequencies, as shown in Figs. 13(b), 13(d), 13(f), 13(h), and 13(j). In general, as the number of cylinders increases, the hydrodynamic interaction among the buoys becomes more violent, and the corresponding curve of capture width has a larger fluctuation amplitude. In most cases, a vertical wall can improve the energy extraction performance of the WEC array, e.g., the values of W_{wall} are greater than 1 within the frequency range of $1.1\pi < k_0 d < 2.1\pi$. Therefore, the reflection effect of a vertical wall can significantly improve the energy extraction performance of the WEC array with appropriate parameter conditions. However, there are also destructive effects for some conditions, e.g., for $\beta = \pi/3$, the existence of a vertical wall reduces the energy extraction performance within the frequency range of $k_0 d < 2.1\pi$.

From the above analysis results, the influence of different parameters (e.g., c, L, β, and N) is essential for the energy extraction performance of the WEC system. Therefore, various parameters should be carefully selected based on local ambient wave and terrain conditions to obtain optimal performance while designing the WEC array.

V. ARRAY OPTIMIZATION UNDER THE ACTION OF REGULAR WAVES

To the authors' knowledge, there is a gap in existing optimization research of cylindrical WEC arrays in front of a vertical wall. This paper takes the total power P_a or the capture width w as the objective function of the array optimization process. Only the energy extraction in the heave direction is considered. The total power and capture width are calculated by Eqs. (42) and (43), respectively. Each buoy in the array has the same size and PTO characteristics. Each buoy has a radius of a and a draught of a. The water depth is $8a$. The wave amplitude is A, and the incident angle is set along the positive x axis ($\beta = 0$). In fact, for a specific sea area, there is usually a dominant wave direction (e.g., the mean wind direction) of the ambient incident wave. The arrays are optimized in the dominant wave direction, i.e., $\beta = 0$. No matter what the dominant direction of the real sea area concerned is, as long as the same coordinate system is established, the optimization of $\beta = 0$ will give the optimal layout for the dominant wave direction. In addition, the dimensionless wavenumber of layout optimization is fixed at $k_0 a = 0.4$, which indicates that the peak power production of the full-scale WEC device (with a radius of 5 m) will coincide with the peak of a JONSWAP spectrum of mean period 5.9 s (Child and Venugopal, 2010). This paper uses real tuning and the mechanical damping of each buoy can be obtained through Eq. (45), that is, $\lambda = 2.94\rho\omega_0 a^3$, and $\delta = 0$.

In this section, the optimal layout of the cylindrical WEC arrays near a vertical wall is investigated. With the fixed number of buoys, the spatial distribution and the incident angle have an important impact on the energy extraction of the WEC array. Currently, the genetic algorithm

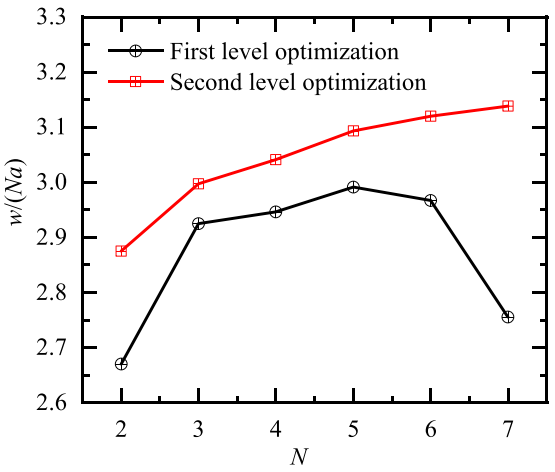

FIG. 17. The variation trend of average capture width with the number of WECs.

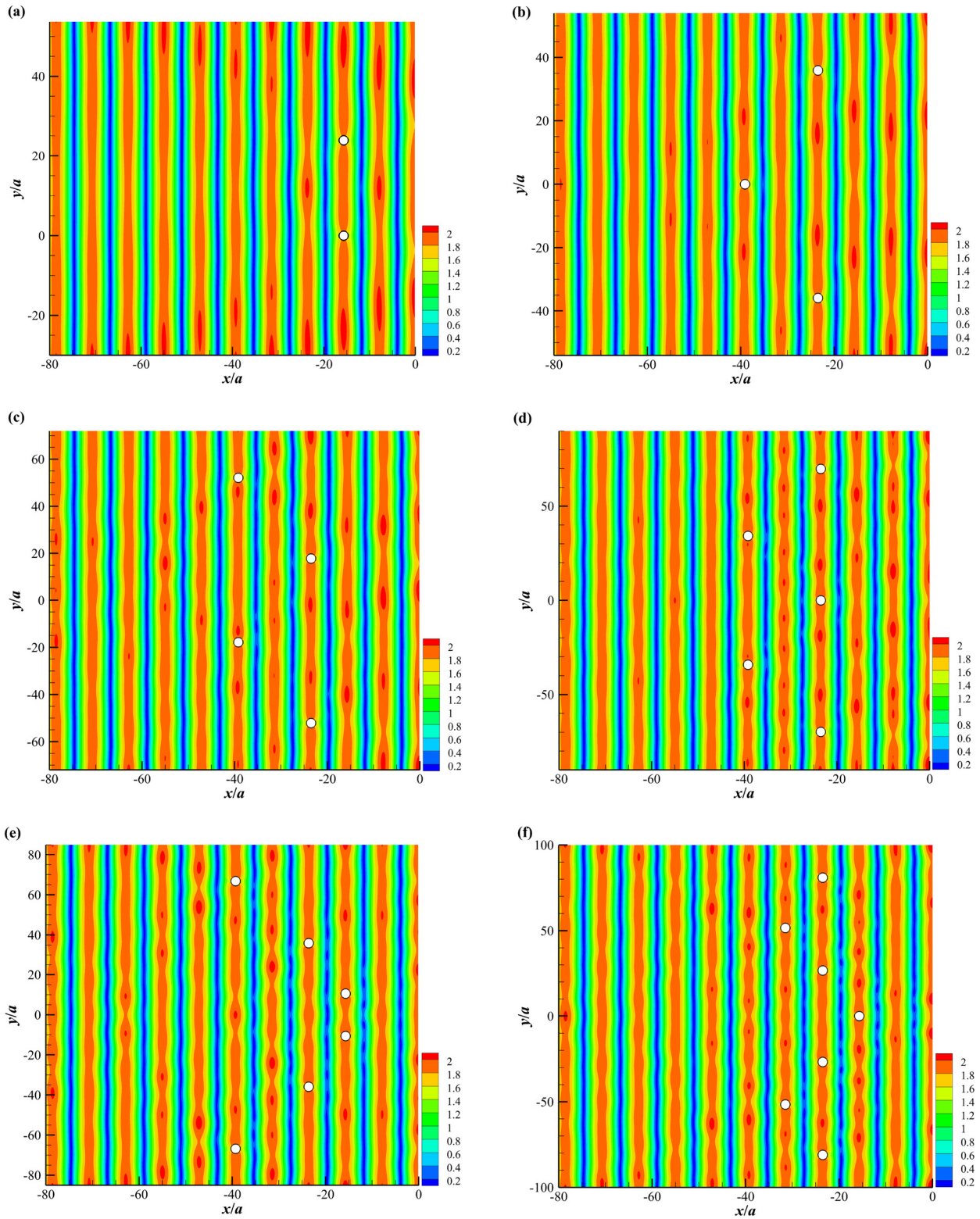

FIG. 18. The optimal layout and corresponding free surface elevation for cases 1–6: (a) case 1, (b) case 2, (c) case 3, (d) case 4, (e) case 5, and (f) case 6.

has been widely used in the layout optimization of the WEC array (Sharp and DuPont, 2018; Ioannou and Loukogeorgaki, 2021; and Zeng *et al.*, 2022b). The genetic algorithm is an optimization method based on a random initial population, and it cannot guarantee a global optimal solution. Therefore, for the optimization space with different grid numbers, an adequate population must be selected to prevent the algorithm from converging too early. In general, when the total optimization space remains unchanged, the greater the number of nodes divided within it (i.e., the smaller the scale of the grids), the more likely it is to obtain the array layout with better energy extraction performance. However, with the number of nodes growing, the total number of potential layouts dramatically increases (Sharp and DuPont, 2018). Therefore, during the optimization process, an appropriate number of nodes must be selected to ensure the stability of the optimization method.

A multi-level genetic algorithm is proposed for layout optimization of the WEC array to improve the energy extraction performance. This method performs the optimization of the array multiple times with different grid densities. The grid spacing is the largest in the initial optimization and gradually decreases in subsequent optimizations. With high optimization efficiency and stable optimization results, multi-level genetic algorithms can effectively improve the performance of optimization results.

A. Genetic algorithm

Genetic algorithm is a stochastic global search and optimization method inspired by imitating the biological evolution process of nature (Holland, 1975). The flow chart of the algorithm is shown in Fig. 14. The implementation process of this algorithm in the WEC array layout optimization problem is described below.

First, the sea area is meshed with uniform square grids, and buoys can be arranged on the grid nodes. The grid spacing S_g and the number of nodes N_n are adjustable parameters. Each node in the grid is encoded using a binary rule to obtain a two-dimensional matrix A. If there is a buoy on the node, the corresponding element value is 1; otherwise, it is 0. The matrix A is called a chromosome or individual, where 0 and 1 are genes. Generate a random primary population P_1 is the first step of a genetic algorithm:

$$P_1 = \{A_1, A_2, A_3, \ldots, A_{N_p}\}, \tag{48}$$

where A_i represents the ith individual in the population, and N_p represents the total number of individuals in the population. It is necessary to check whether the spacing among each buoy in the array meets the restriction condition, i.e., $S_m > 2a$. In other words, there cannot be overlap among buoys. Overlap checks should also be performed for subsequent operations.

Then, the theoretical model established in Sec. II of this paper is used to calculate the heave amplitude of all individuals in the current population. According to Eq. (42), the total power P_a of the array can be obtained and ranked.

When the value of the optimal fitness function in the population remains unchanged for N_c consecutive generations, it denotes the algorithm achieves convergence. If the algorithm achieves convergence or the total generations reaches the predetermined upper limit N_g, the algorithm stops and outputs the optimal solution.

If the results do not meet the convergence condition, the current population is subjected to the operation procedures of selection, crossover, and mutation to generate a new generation population. The same operations are performed on the new population until the convergence condition is satisfied.

Selection, crossover, and mutation are the basic steps of genetic algorithms. The process of selection ensures that evolution occurs. The top-ranked individuals in the population directly copy themselves to the next generation, which ensures that excellent genes are inherited. The top-ranked elite individuals also participate in the crossover process, which is conducive to the increase in excellent genes in the next generation of the population. The bottom-ranked individuals in the population are directly eliminated and cannot participate in the crossover operation. During the optimization process, the selection rate R_s is the same for elitist and elimination, which ensures that the population size N_p remains unchanged.

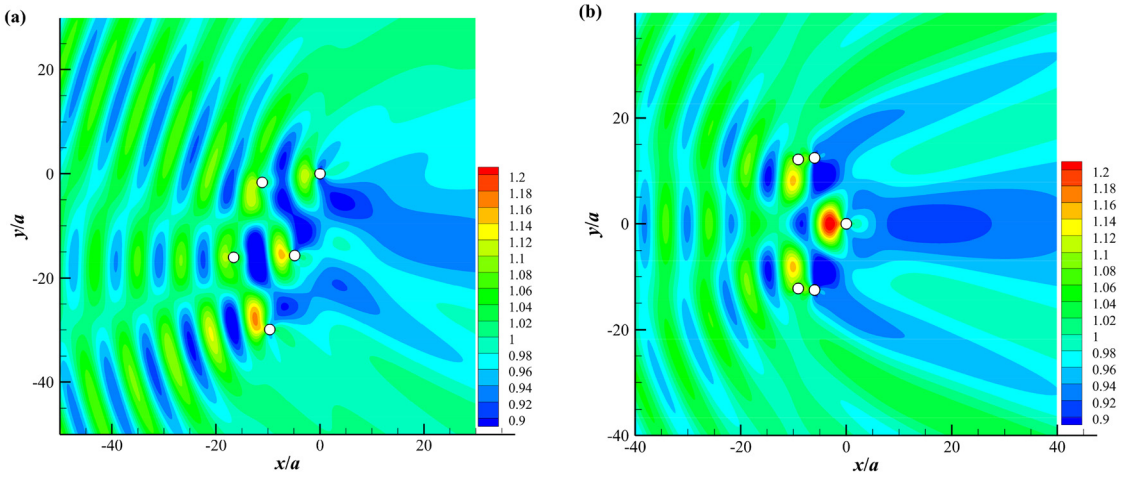

FIG. 19. Optimal layout of five buoys in an open water domain: (a) Child and Venugopal (2010) (Fig. 5G1); (b) present study.

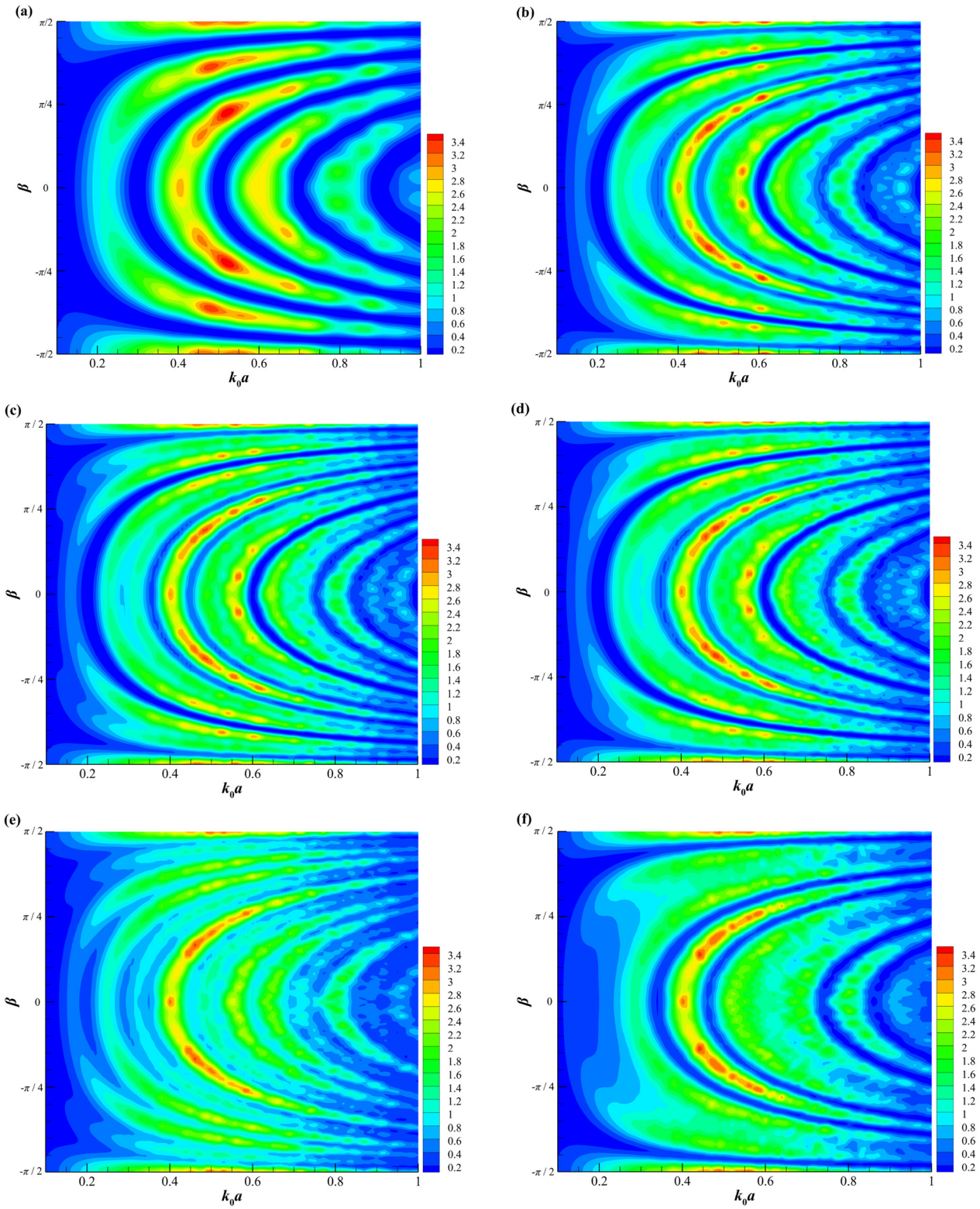

FIG. 20. Contour plots of the average capture width for cases 1–6: (a) case 1, (b) case 2, (c) case 3, (d) case 4, (e) case 5, and (f) case 6.

The purpose of crossover is to recombinant genes and provide population diversity. Randomly select a location where the genotypes of parent 1 and parent 2 are different, and then exchange their genes at this location. With a crossover operation, the offspring will have completely different genotypes compared with their parents. The crossover operation greatly improves the search capabilities of a genetic algorithm.

After the crossover operation is completed, the mutation operation is performed on the individuals. The number of individuals participating in mutation is adjustable through the mutation rate R_m. For individuals participating in the mutation operation, two locations with different internal genotypes are randomly selected, and the genotypes at the two locations are exchanged. The mutation operation further improves the global search capability of a genetic algorithm and is beneficial to finding the optimal solution.

B. Multi-level optimization

In general, the genetic algorithm proposed in Sec. V A can be applied to layout optimization of the WEC array with arbitrary grid density and any number of buoys. However, when array optimization is performed in a larger sea area, in order to ensure the stability and efficiency of the calculation results, the number of nodes must be controlled within an appropriate range; that is, the grid spacing must be relatively large. Therefore, the conventional direct optimization process is limited in improving the energy extraction performance of the array.

In this paper, a multi-level genetic algorithm for WEC array layout optimization is proposed. The array is optimized multiple times with different grid densities. The grid spacing is largest in the initial level optimization and gradually reduced in subsequent level optimizations. Figure 15 shows a schematic diagram of multi-level optimization. The example shown in the figure has two different grid densities. The first-level optimization is targeted at larger-scale grid nodes; that is, the layout optimization of the three buoys marked a, b, and c in the blue grid, as shown in Fig. 15. The genetic algorithm described in Sec. V A can be used directly for the first-level optimization. Then, based on the results of the first-level optimization, the grid density and spatial scope of the second-level optimization are determined. Compared with the first-level optimization, the grid spacing of the second-level optimization is smaller, but the total number of grid nodes cannot increase significantly. In the second-level optimization, the coding of a genetic algorithm needs to be slightly adjusted to constrain the locations of different individuals to obtain the optimization results marked a_1, b_1, and c_1 in the yellow grid, as shown in Fig. 15. In other words,

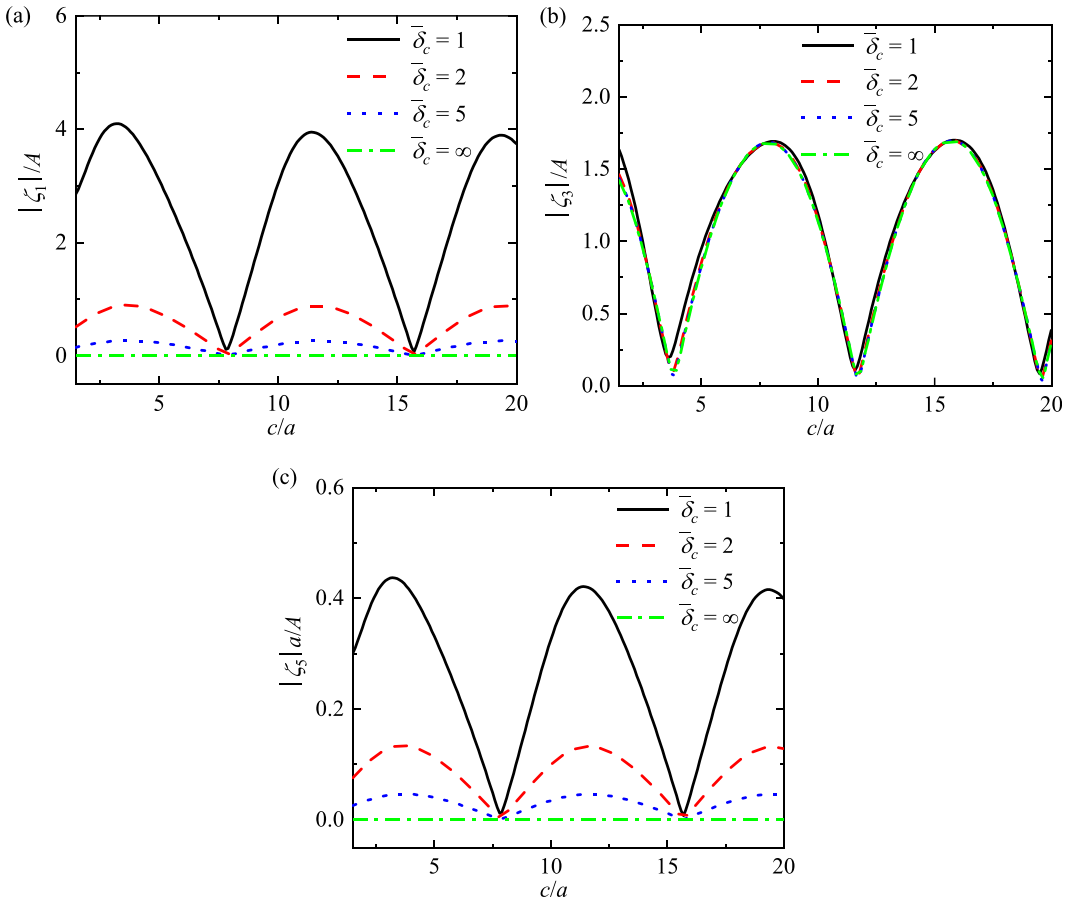

FIG. 21. The amplitudes of an isolated WEC with different equivalent stiffnesses: (a) surge, (b) heave, (c) pitch.

the second-level optimization is a process of local optimization within a limited range around the coordinates of each buoy obtained by the first-level optimization. Similarly, next-level layout optimization can be performed on smaller-scale grids.

Next, the specific cases are conducted.

C. Cases of two-level optimization

Based on the multi-level optimization method proposed in Sec. V B, an implementation program for layout optimization is developed. The optimal layouts of the WEC arrays with different numbers of buoys are investigated.

Before studying the optimal layout of the array, the energy extraction performance of an isolated WEC is examined first. Figure 16 shows the contour plot of capture width w changes with c/a and β. As the incident angle changes, the standing wave field induced by the reflection of a vertical wall also changes. It can be seen from Fig. 16 that the maximum value of the capture width appears periodically with c/a. For $\beta = 0$, the capture width reaches the maximum value at $c/a = 15.7$.

Next, the multi-level optimization method is adopted to optimize the layout of the array.

The first-level optimization is performed on a larger grid spacing, and the results are the basis for the next-level optimization. As shown in Table II, six cases are investigated, named cases 1–6, including 2–7 buoys, respectively. The grid spacing of the first-level optimization is $3a$, i.e., $S_m^1 = 3a$. The number of nodes of 61×61 is selected to ensure that the deployed sea area is large enough. Specifically, the size of the optimization space is $180a \times 180a$. The initial population is randomly generated during the optimization process. In order to ensure the reliability of the optimization results, each case needs to be simulated multiple times. The optimal solution that appears repeatedly in multiple simulations is adopted. Based on the results of the first-level optimization, the second-level optimization is performed for each case. The number of nodes of the second-level optimization is 61×61, and the coordinates of each buoy obtained by the first-level optimization are used as the center points. The program needs to be adjusted slightly.

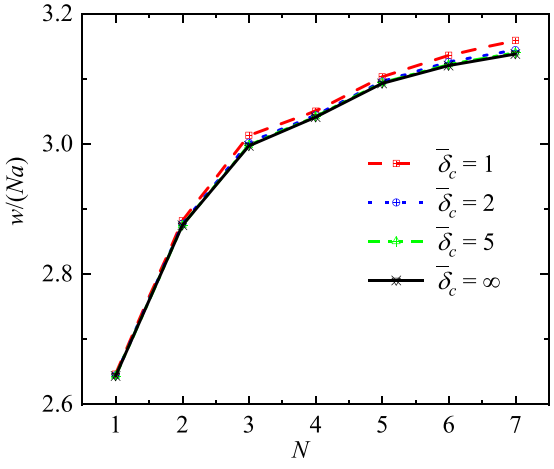

FIG. 22. The influence of different equivalent stiffnesses on the energy extraction performance for six optimal layouts.

TABLE V. The average capture widths $w/(Na)$ of six optimal layouts with different equivalent stiffnesses.

	$\bar{\delta}_c = 1$	$\bar{\delta}_c = 2$	$\bar{\delta}_c = 5$	$\bar{\delta}_c = \infty$
$N = 1$	2.646	2.644	2.643	2.643
$N = 2$ (case 1)	2.882	2.877	2.875	2.875
$N = 3$ (case 2)	3.013	3.002	2.998	2.997
$N = 4$ (case 3)	3.050	3.044	3.042	3.041
$N = 5$ (case 4)	3.103	3.096	3.094	3.093
$N = 6$ (case 5)	3.136	3.126	3.122	3.120
$N = 7$ (case 6)	3.159	3.144	3.140	3.138

Similar to the first-level optimization, the second-level optimization also needs to be simulated multiple times for each case.

The first-level optimization results and the second-level optimization results for each case are shown in Tables III and IV. The total energy capture power P_a and average capture width $w/(Na)$ of an array are also given.

For convenience of description, the optimization parameters of the first-level optimization and the second-level optimization only differ on the grid spacing, but it does not affect the applicability of the multi-level optimization method. According to the method, the optimal solution, which appears consistently across multiple simulations, can usually be obtained with fewer than five simulation attempts. Of course, as the number of buoys increases, the number of iterations and calculation time required for each simulation can also increase accordingly. In case 6, which has the maximum number of buoys in this paper, the results of five simulations all reach convergence before 60 iterations, and the results obtained by the three simulations are consistent and have the best energy extraction performance. In the simulation of case 6, the calculation time for one iteration (population size N_p is 300) is about 6 min. The computing system uses Intel(R) Xeon(R) Gold 6130 CPU @ 2.1GHz with 64 cores and 128 threads, and the RAM is 176GB. With five identical buoys, case 4 is selected to test the optimization efficiency of the traditional genetic algorithm in the same sea area. The sea area is $180a \times 180a$ and the grid spacing is $0.1a$, i.e.,

TABLE VI. Amplitudes of the optimal WEC array consisting of seven buoys.

	$\bar{\delta}_c = 1$	$\bar{\delta}_c = 2$	$\bar{\delta}_c = 5$	$\bar{\delta}_c = \infty$
$\lvert\zeta_1^{(1)}\rvert/A$	0.065	0.014	0.004	0
$\lvert\zeta_1^{(3)}\rvert/A$	0.170	0.041	0.012	0
$\lvert\zeta_1^{(5)}\rvert/A$	0.077	0.019	0.006	0
$\lvert\zeta_1^{(7)}\rvert/A$	0.125	0.027	0.008	0
$\lvert\zeta_3^{(1)}\rvert/A$	1.880	1.866	1.862	1.860
$\lvert\zeta_3^{(3)}\rvert/A$	1.867	1.860	1.858	1.857
$\lvert\zeta_3^{(5)}\rvert/A$	1.824	1.825	1.826	1.826
$\lvert\zeta_3^{(7)}\rvert/A$	1.861	1.858	1.857	1.857
$\lvert\zeta_5^{(1)}\rvert a/A$	0.007	0.002	0	0
$\lvert\zeta_5^{(3)}\rvert a/A$	0.018	0.006	0.002	0
$\lvert\zeta_5^{(5)}\rvert a/A$	0.008	0.003	0.001	0
$\lvert\zeta_5^{(7)}\rvert a/A$	0.013	0.004	0.001	0

the number of nodes is 1801 × 1801. The population size, maximum number of iterations, selection rate, and mutation rate are the same as in Table II. Case 4 is simulated 30 times using the traditional genetic algorithm, and most of the calculation results reach convergence before 160 iterations. However, the results obtained in each simulation are different, and the total energy extraction of the optimal array in 30 simulations is smaller than the result of case 4 obtained by two-level optimization, as shown in Table IV. From the perspective of arrangement geometry, the growth in the number of nodes increases the total number of global potential arrangements, which decreases the optimization efficiency and reduces convergence speed. Therefore, choosing the appropriate number of nodes is crucial, which is also the inspiration for the multi-level optimization method proposed in this paper. While ensuring optimization efficiency, the multi-level optimization

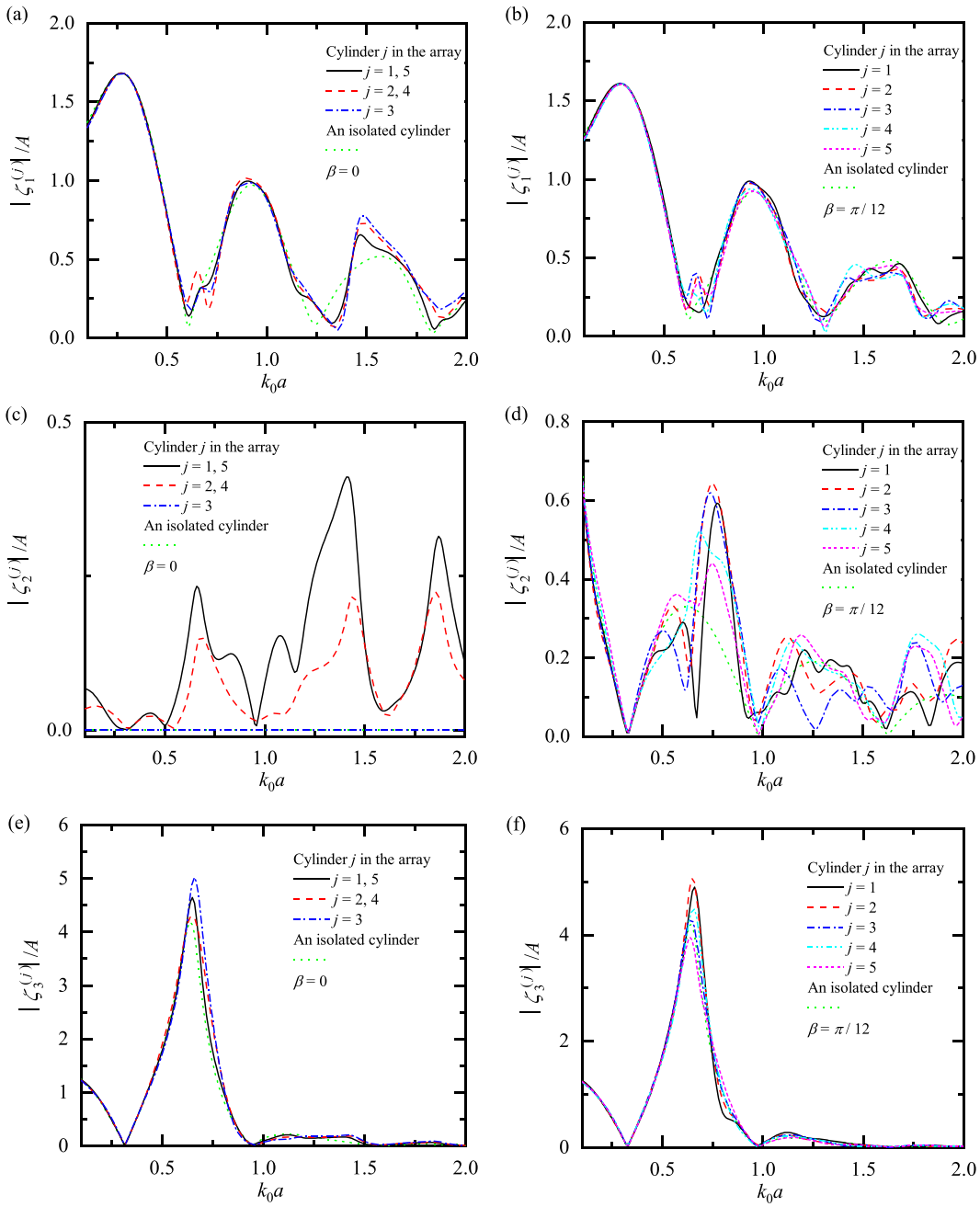

FIG. 23. Amplitude responses of each DOF for the array consisting of five buoys: (a), (c), (e), (g), and (i) $\beta = 0$; (b), (d), (f), (h), and (j) $\beta = \pi/12$.

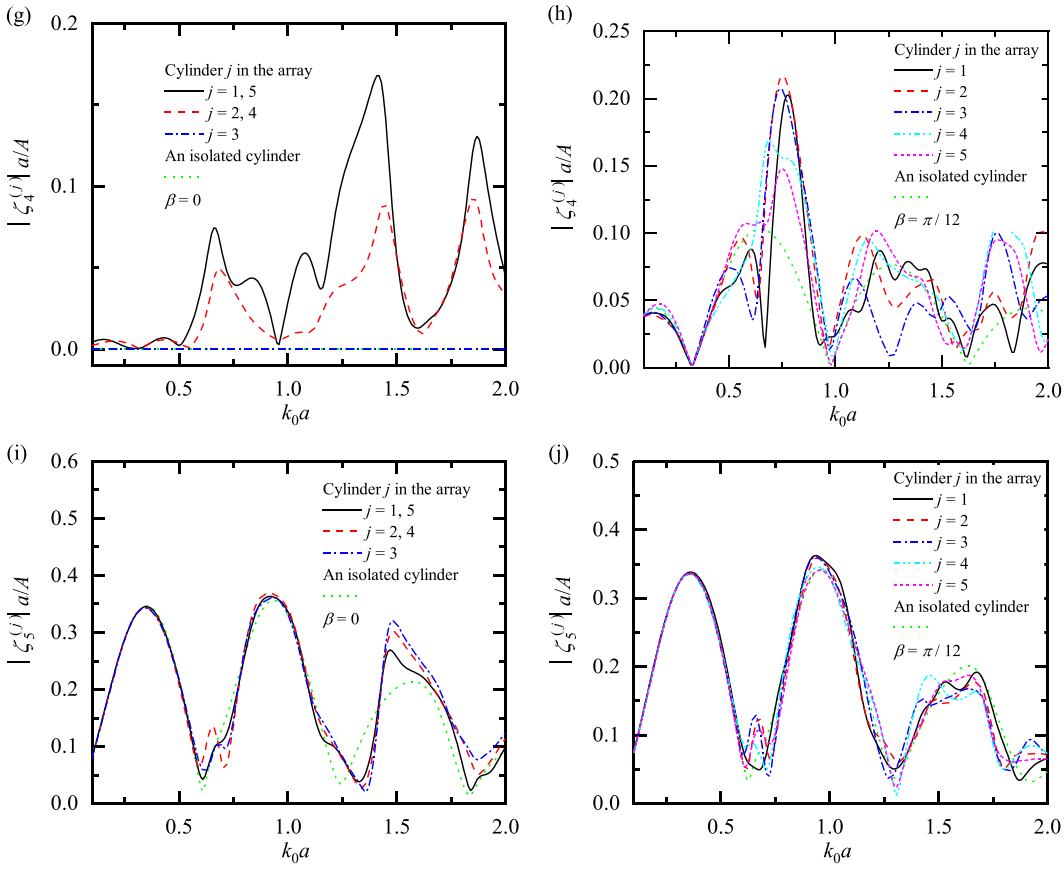

FIG. 23. (*Continued.*)

method can quickly obtain an optimal array layout with better energy extraction performance.

Figure 17 shows the average capture width of the first-level optimization and the second-level optimization for cases 1–6. It is observed from the figure that the second-level optimization can significantly improve the energy capture performance of the WEC array for each case. In case 6, the energy extraction performance of the second-level optimization is 13.9% higher than that of the first-level optimization. In the first-level optimization, the average capture width shows a trend of first increasing and then decreasing as the number of buoys increases and reaches the maximum value in case 4 ($N = 5$). It shows that when the grid spacing is unchanged in optimization, only performing the first-level optimization may not necessarily yield the array layout with optimal energy extraction performance. However, the multi-level optimization method can improve this situation. As shown in Fig. 17, as the number of WECs increases, the average capture width of the second-level optimization gradually increases, and the increase trend gradually slows down. As the number of buoys increases, the spacing among buoys also increases, which weakens the hydrodynamic interaction of the WEC array and slows down the increasing trend of the average capture width. By further reducing the grid size and performing next-level optimization, the energy extraction performance of the WEC array can be improved. However, as the grid spacing and optimization space gradually decrease, the increase in the total power of the WEC array gradually decreases.

In order to more intuitively display the relative positions of buoys in the array, Fig. 18 shows the optimal layout and the free surface elevation of six cases. The plots use the same color scale to facilitate comparison. It is observed from Fig. 18 that the positions of the buoys in the optimal layout are all distributed near the crest of the standing wave field. Except for case 1, a linear array, the buoys in cases 2–6 are all staggered. At the same time, all optimal array layouts possess symmetry. Among them, the optimal array layout of case 3 is centrally symmetrical, and the symmetry center point is (31.35, 0). The other cases are symmetrical about the x-axis.

With a total power of 191.196 kW, the average capture width of case 4 is 3.093. To compare with published results, the multi-level optimization method is utilized to investigate the optimal layout of an array containing five buoys in an open water domain. The optimization parameters are consistent with Table II. The coordinates of the optimal layout obtained by two-level optimization are (0.0, 0.0), (−9.1, 12.2), (−9.1, −12.2), (−6.0, 12.5), (−6.0, −12.5). The total power of the optimal layout is 49.646 kW. Figure 19(b) visually shows the relative position of each buoy in the optimal layout and gives the contour

plot of the free surface elevation. As shown in Fig. 19(a), the total power of the optimal layout of a WEC array consisting of five buoys given by Child and Venugopal (2010) (Fig. 5G1) is 49.345 kW. Therefore, it is obvious that the optimal array obtained by the multi-level optimization method has higher energy extraction performance.

Figure 20 shows the contour plots of the average capture width with the dimensionless wave number k_0a and incident angle β for cases 1–6. For convenience comparison, the figures utilize the same color scale. It is observed from Fig. 20 that the contour plots of the average capture width are symmetrical about $\beta = 0$ except for case 3 [Fig. 20(c)]. Other optimal layouts are symmetrical about $\beta = 0$ except

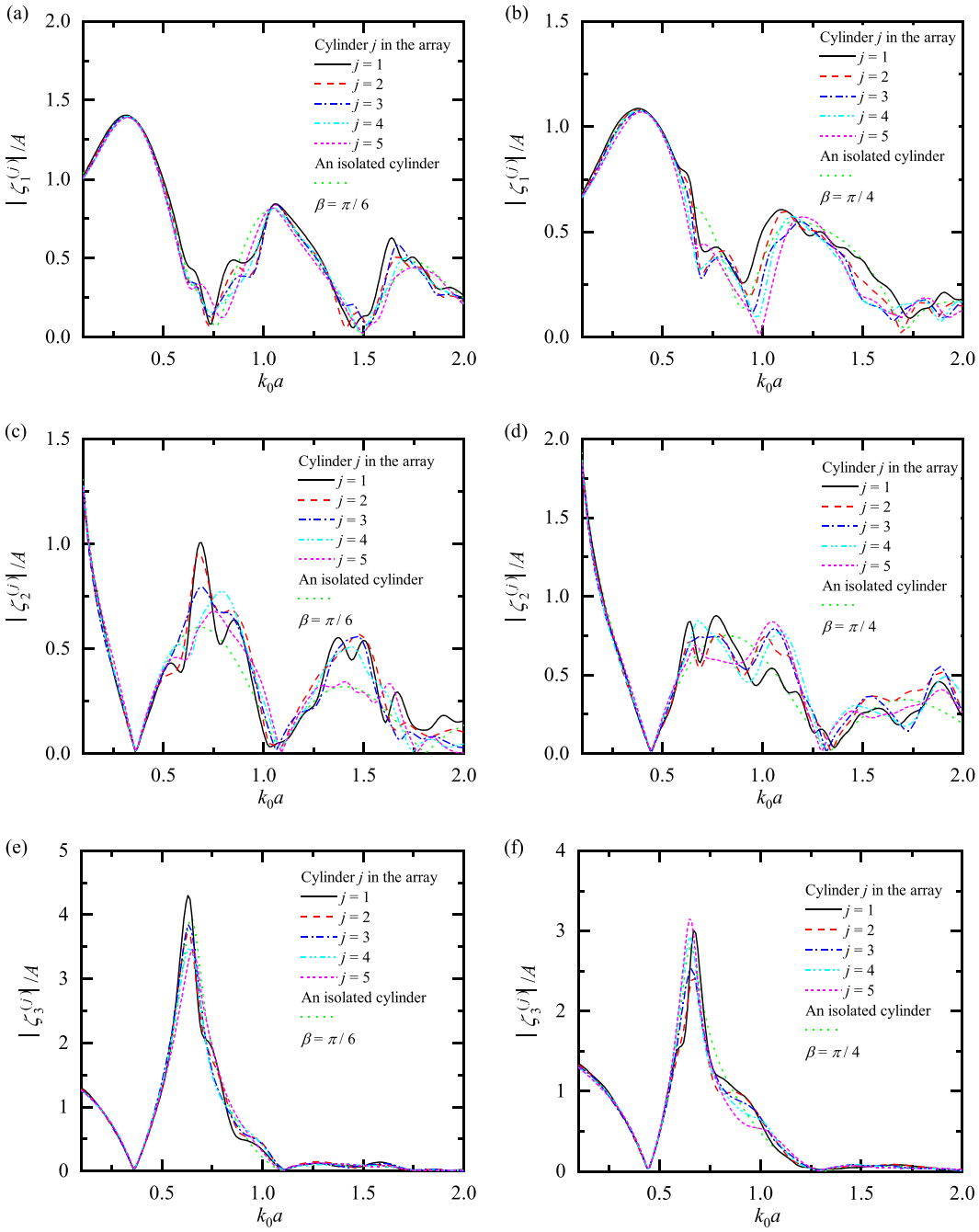

FIG. 24. Amplitude responses of each DOF for the array consisting of five buoys: (a), (c), (e), (g), (i) $\beta = \pi/6$; (b), (d), (f), (h), and (j) $\beta = \pi/4$.

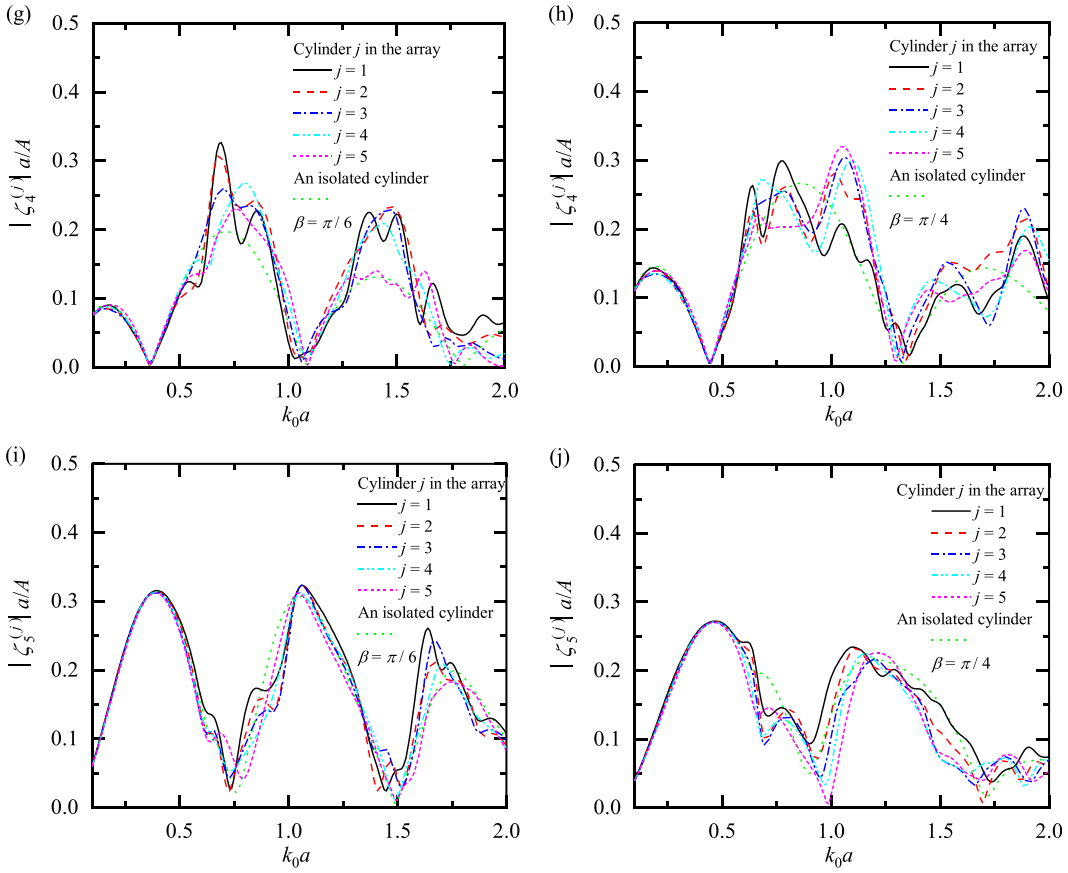

FIG. 24. (*Continued.*)

for case 3, so the symmetry of the calculation results shown in Fig. 20 is as expected. For $k_0a < 0.2$, the calculation results of average capture width are less than 1 for all cases. Larger values of the average capture width for all cases occur periodically with increasing dimensionless wavenumber k_0a. As the absolute value of the incident angle increases, the wave frequency corresponding to the maximum value of capture width gradually increases. For $k_0a = 0.4$, the maximum value of average capture width for each case occurs at $\beta = 0$.

In this section, a multi-level optimization method based on a genetic algorithm is proposed to investigate the optimal layout of the six WEC arrays composed of 2–7 buoys. Compared with the traditional genetic algorithm, the multi-level optimization method can effectively improve the optimization efficiency and obtain an array layout with better energy extraction performance. By adjusting the constraints and objective function, the multi-level optimization method can optimize more parameters, such as the geometric size of the buoy, the number of buoys, the irregular waves, the real wave scenarios, and the multi-degree-of-freedom model.

VI. RESEARCH ON FIVE DEGREES OF FREEDOM MODEL

The hydrodynamic analysis of Secs. IV and V utilize the single degree of freedom (heave) model, i.e., the buoys in the WEC array only moves in the heave mode. This section investigates the effect of multi-degree-of-freedom motion on the hydrodynamic performance. Each buoy has five motion modes, i.e., surge, heave, heave, roll, and pitch. For the convenience of description, the four degrees of freedom (surge, sway, roll, and pitch) are called other DOFs. The geometric size of buoys is consistent with Sec. IV, i.e., each cylinder has a radius of a and a draught of a. The water depth is $8a$. The height of buoys above the free surface is $0.5a$. The center of mass of buoy j is at $(x_j, y_j, 0.0)$. The mass, moment of inertia, and hydrostatic recovery stiffness of each buoy can be solved by Eqs. (39) and (40). For comparison, the 5DOF model extracts energy only in the heave mode, and the PTO characteristics are consistent with the 1DOF model, i.e., the optimal damping calculated by Eq. (45) and $\delta_3 = 0$. The spring constraints of the buoys on other DOFs are modeled as equivalent stiffness. The spring constraints of all buoys in the array are the same and do not couple with each other. Let $\bar{\delta}_c = \delta_{1,2}/\rho g\pi a^2 = \delta_{4,5}/\rho g\pi a^4$, represents the dimensionless equivalent stiffness of other degrees of freedom.

A. An isolated buoy

Figure 21 shows the amplitudes of surge, heave, and pitch for an isolated buoy. The wavenumber is fixed at $k_0a = 0.4$, $\beta = 0$. The PTO damping of each buoy is $\lambda = 2.94\rho\omega_0a^3$. As the equivalent stiffness of

other DOFs increases, the amplitudes of the surge amplitude and the pitch amplitude gradually decrease, as shown in Figs. 21(a) and 21(c). The heave amplitudes are very close with different equivalent stiffness conditions. However, there are distinct differences under certain conditions (e.g., for $c/a = 1.5$, the amplitude of $\bar{\delta}_c = 1$ is 1.14 times of $\bar{\delta}_c = \infty$; for $c/a = 3.8$, the amplitude of $\bar{\delta}_c = 1$ is 3.87 times of $\bar{\delta}_c = \infty$). For $\bar{\delta}_c = 2$, the heave amplitude of 5DOF WEC is almost consistent with the 1DOF WEC (i.e., $\bar{\delta}_c = \infty$). For $k_0a = 0.4$, the wavelength of a standing wave field is about 15.7a. It is interesting that the peaks (valleys) of the surge amplitude and the pitch amplitude appear at the same values of c/a, while the peaks (valleys) of the heave amplitude are opposite. It means that the heave amplitude reaches the maximum near the crest of the standing wave field, and the surge amplitude (pitch amplitude) reaches the maximum near the nodes of

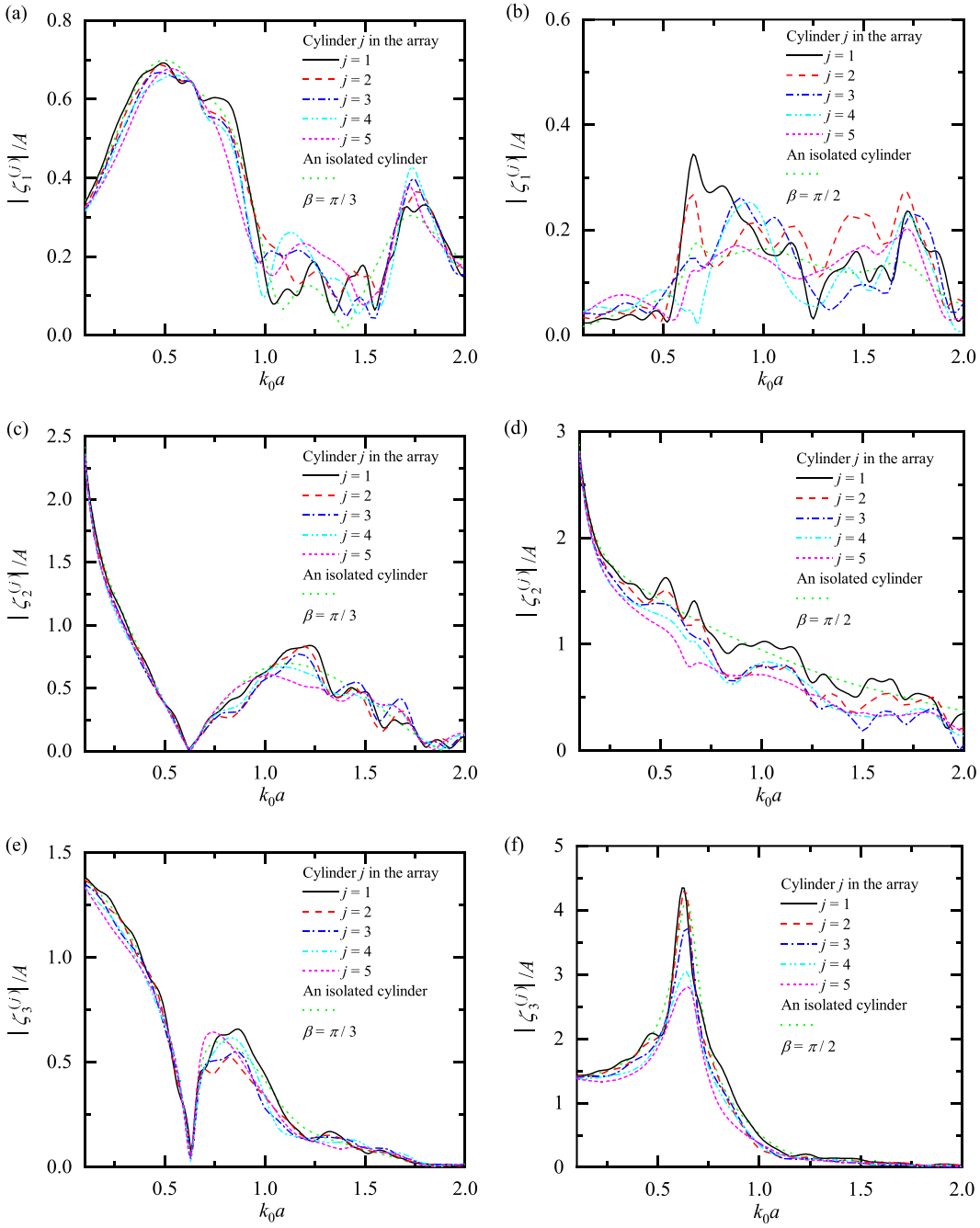

FIG. 25. Amplitude responses of each DOF for the array consisting of five buoys: (a), (c), (e), (g), (i) $\beta = \pi/3$; (b), (d), (f), (h), (j) $\beta = \pi/2$.

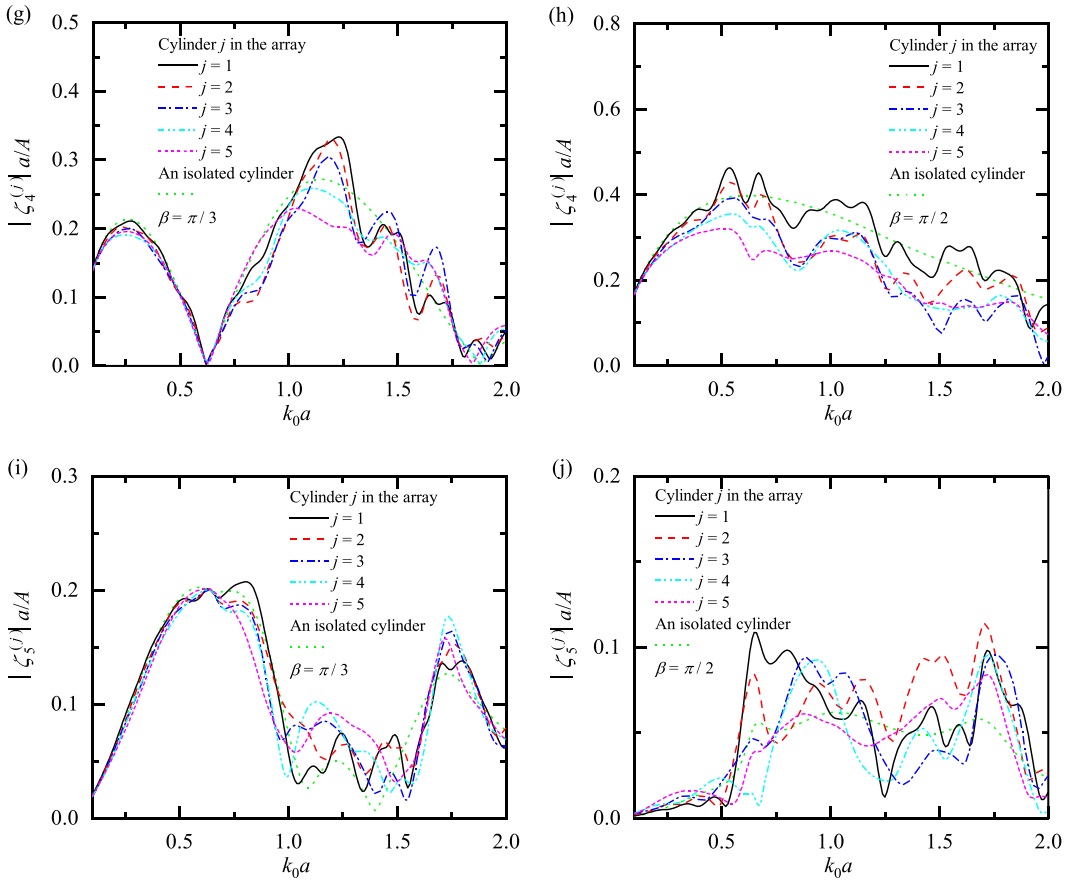

FIG. 25. (*Continued.*)

the standing wave field. Therefore, if the buoy extracts energy on multiple degrees of freedom (e.g., surge, sway, heave, roll, and pitch), the position of the buoy and PTO characteristics (spring δ_p^j and damping λ_p^j) of each DOF are comprehensively considered to achieve optimal energy extraction performance.

B. Six optimal layouts

In this subsection, the impact of other DOFs on the energy extraction performance of the six optimal layouts is investigated. The six optimal layouts are given in Sec. V C. The wavenumber is fixed at $k_0a = 0.4$, $\beta = 0$. For comparison, the results of an isolated WEC also are plotted in Fig. 22. The spacing between the center of an isolated WEC and a vertical wall is $c = 15.7a$. Figure 22 shows the average capture width of six optimal layouts with different equivalent stiffness conditions. Table V lists the specific values for Fig. 22. The case of $\bar{\delta}_c = \infty$ is equivalent to the 1DOF model, and the calculation results of $\bar{\delta}_c = \infty$ are consistent with the results obtained by the second-level optimization in Fig. 17. It is observed from Fig. 22 that as the equivalent stiffness reduces, the average capture width of the WEC array increases. Meanwhile, as the number of floats increases, the impact of other degrees of freedom on the energy extraction performance of the WEC array gradually increases. As shown in Fig. 22, the multiple degrees of freedom are beneficial to improving the energy extraction performance of the WEC array. It indicates that the oscillations of other DOFs create a hydrodynamic interaction that is beneficial to the heave motion. For the six cases based on the 1DOF model, the buoys in the optimal layouts are basically near the crest of the standing wave field, as shown in Fig. 18. It is observed from Fig. 21 that the buoys mainly oscillate in heave mode instead of other DOFs when the buoys are near the crest of the standing wave field. Therefore, the impact of other DOFs on array performance is relatively small.

For different equivalent stiffness conditions, Table VI gives the amplitude responses of the WEC array composed of seven buoys. The coordinates of buoys 1–7 are (−15.7, 0.0), (−23.5, 81.0), (−23.5, 26.7), (−31.5, 51.6), (−23.5, −81.0), (−23.5, −26.7), and (−31.5, −51.6), respectively. Since the incident angle is $\beta = 0$, and the array is symmetrical about the x axis, the amplitudes of buoys 2–4 are consistent with buoys 5–7, respectively. It is observed from Table VI that the heave amplitudes of the 5DOF model are all larger than that of the 1DOF model ($\bar{\delta}_c = \infty$) for buoys 1, 3, 4, 6, and 7. According to Eqs. (41) and (43), the capture width w of the array is proportional to the square of the heave amplitudes. Therefore, the energy extraction performance of the 5DOF model is better than that of the 1DOF model for the optimal WEC array consisting of seven buoys.

C. Five buoys

In this subsection, for an equidistant linear array consisting of five identical buoys, the influence of other DOFs on the hydrodynamic performance with different incident angles ($\beta = 0$, $\beta = \pi/12$, $\beta = \pi/6$, $\beta = \pi/4$, $\beta = \pi/3$, $\beta = \pi/2$) is investigated. The specific arrangement is shown in Fig. 4, $L/a = 6$, and $c/a = 5$. As shown in Figs. 23–25, the variation curves of the pitch, heave, heave, roll, and pitch amplitudes with the dimensionless wavenumber are plotted. The equivalent stiffness of each buoy is $\bar{\delta}_c = 0$. For comparison, the dimensionless amplitudes of an isolated buoy near a vertical wall are also plotted (green dotted line).

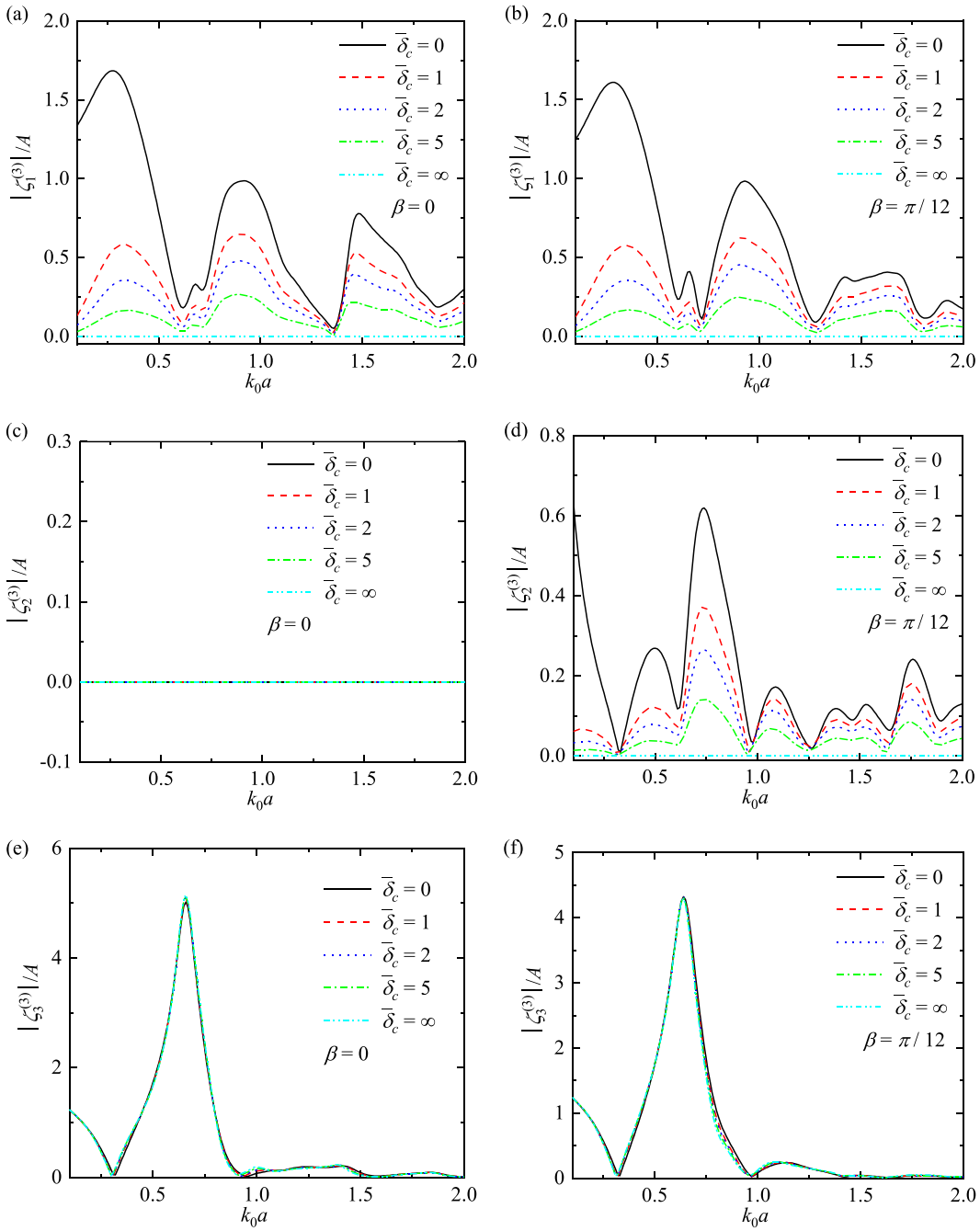

FIG. 26. Amplitude responses of each DOF for the middle buoy of the 5-WEC array with different equivalent stiffnesses: (a), (c), (e), (g), and (i) $\beta = 0$; (b), (d), (f), (h), and (j) $\beta = \pi/12$.

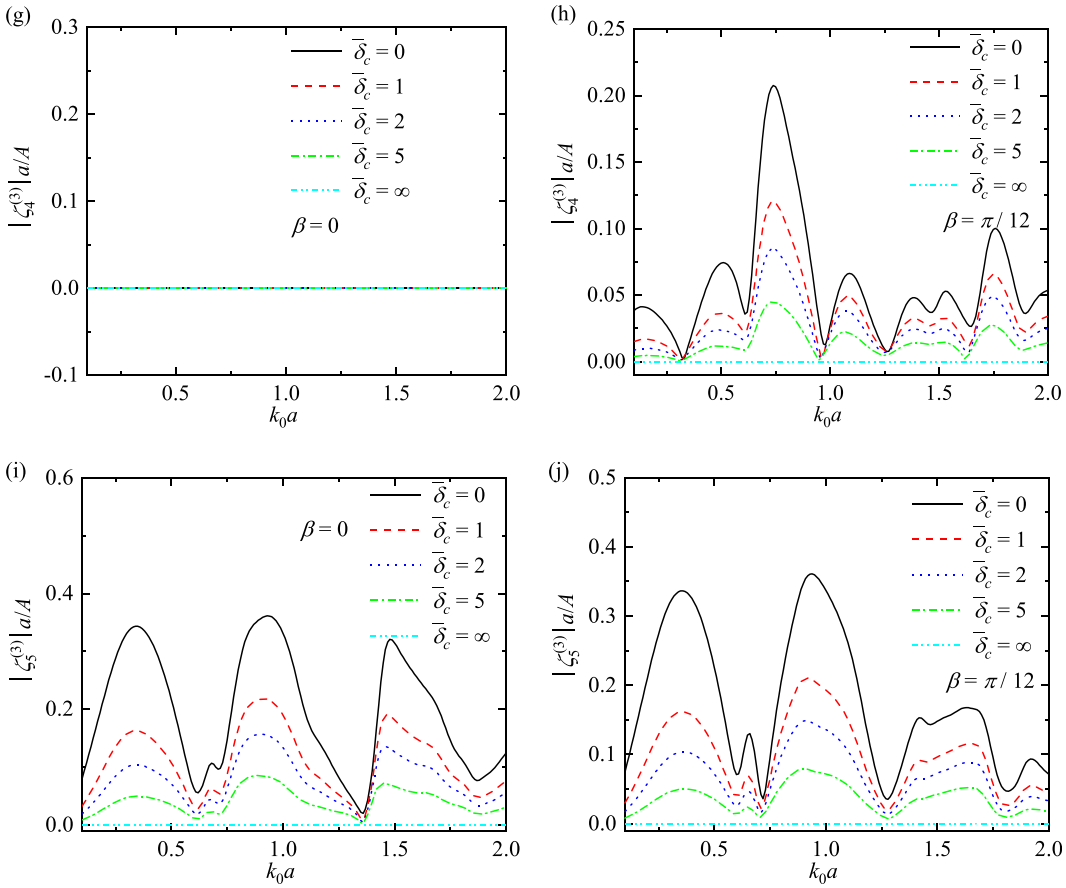

FIG. 26. (*Continued.*)

For the incident angle $\beta = 0$, due to the symmetry of the array layout, the amplitude responses of buoy 1 (2) and buoy 5 (4) are the same, as shown in Figs. 23(a), 23(c), 23(e), 23(g), and 23(i). It is observed from Figs. 23(c) and 23(g) that the sway and roll amplitudes of an isolated buoy and the middle buoy (third buoy) are zero. These results are consistent with expectations. Due to the hydrodynamic interaction among the buoys, the sway and roll amplitudes of buoy 1 (5) and buoy 2 (4) are usually not zero. For the incident angle of $\beta = 0$, the variation curves of sway and roll amplitudes with dimensionless wavenumber are very similar, but the magnitudes of the dimensionless amplitudes have differences, as shown in Figs. 23(c) and 23(g). For $\beta = \pi/2$, the variation curves of the surge and pitch amplitudes with the dimensionless wavenumber also have similar rules, as shown in Figs. 25(b) and 25(j). In other words, for $\beta = 0$ ($\beta = \pi/2$), the hydrodynamic force generated by the incident wave potential on each buoy does not contribute to the amplitudes of sway and roll (surge and pitch). The amplitudes of sway and roll (pitch and pitch) for the case of $\beta = 0$ ($\beta = \pi/2$) are completely generated by the hydrodynamic interaction of the wave diffraction and radiation.

With different wave incident angles, the heave amplitude of each buoy in the array has an obvious peak near the dimensionless wavenumber of $k_0a = 0.636$, as shown in Figs. 23(e), 23(f), 24(e), 24(f), 25(e), and 25(f). Such a peak should be attributed to the resonance motion of the buoys. The detailed explanations are given as follows. For $\beta = 0$, the wavenumber corresponding to the heave amplitude peak of an isolated buoy is $k_0a = 0.636$, as shown in the green dotted line in Fig. 23(e). According to the dispersion relationship, the wave frequency of $k_0a = 0.636$ is $\omega_0 = 2.256\sqrt{g/d}$. For an isolated buoy, computations show that added mass owing to the forced heave oscillation is $a_{33}^{(11)} = 1.770\rho a^3$. As noted by Falnes (2002), the natural frequency of an isolated buoy in heave mode is $\omega_n = \sqrt{(k_3^{(1)} + \delta_3^{(1)})/(M_3^{(1)} + a_{33}^{(11)})} = 2.262\sqrt{g/d}$. As is well known, for systems with damping (mechanical damping of the PTO system and radiation damping are not included in the calculation of natural frequency ω_n), resonance occurs when the excitation frequency is close to and slightly smaller than the natural frequency. Obviously, due to the fact that wave excitation frequency ω_0 is almost equal to and slightly smaller than the natural frequency ω_n of heave oscillation of buoy, the peaks in Figs. 23(e), 23(f), 24(e), 24(f), 25(e), and 25(f) can be attributed to the resonance motions of the buoys in the heave direction. Consequently, it can be concluded that the heave amplitude of an isolated buoy is in resonance at $k_0a = 0.636$. As shown in Fig. 23(e), for each buoy in the array, the magnitudes and the corresponding

frequencies of the heave amplitude peak are different from an isolated buoy near the dimensionless wavenumber of $k_0a = 0.636$, which reflects the influence of hydrodynamic interaction among the buoys.

For cases with different incident angles of the ambient wave, the variation in the amplitudes with k_0a is complex. As shown in Figs. 23(a) and 23(i), for $\beta = 0$, the surge and pitch amplitudes of each buoy are very close to that of an isolated buoy within the wavenumber range of $0.1 < k_0a < 0.5$ and $0.8 < k_0a < 1.2$. It shows that the hydrodynamic interaction among buoys has little influence on the amplitudes of surge and pitch at these frequencies. As shown in Fig. 25(d), for $\beta = \pi/2$, the sway amplitude of an isolated buoy decreases monotonically as the dimensionless wavenumber increases. Due to the hydrodynamic

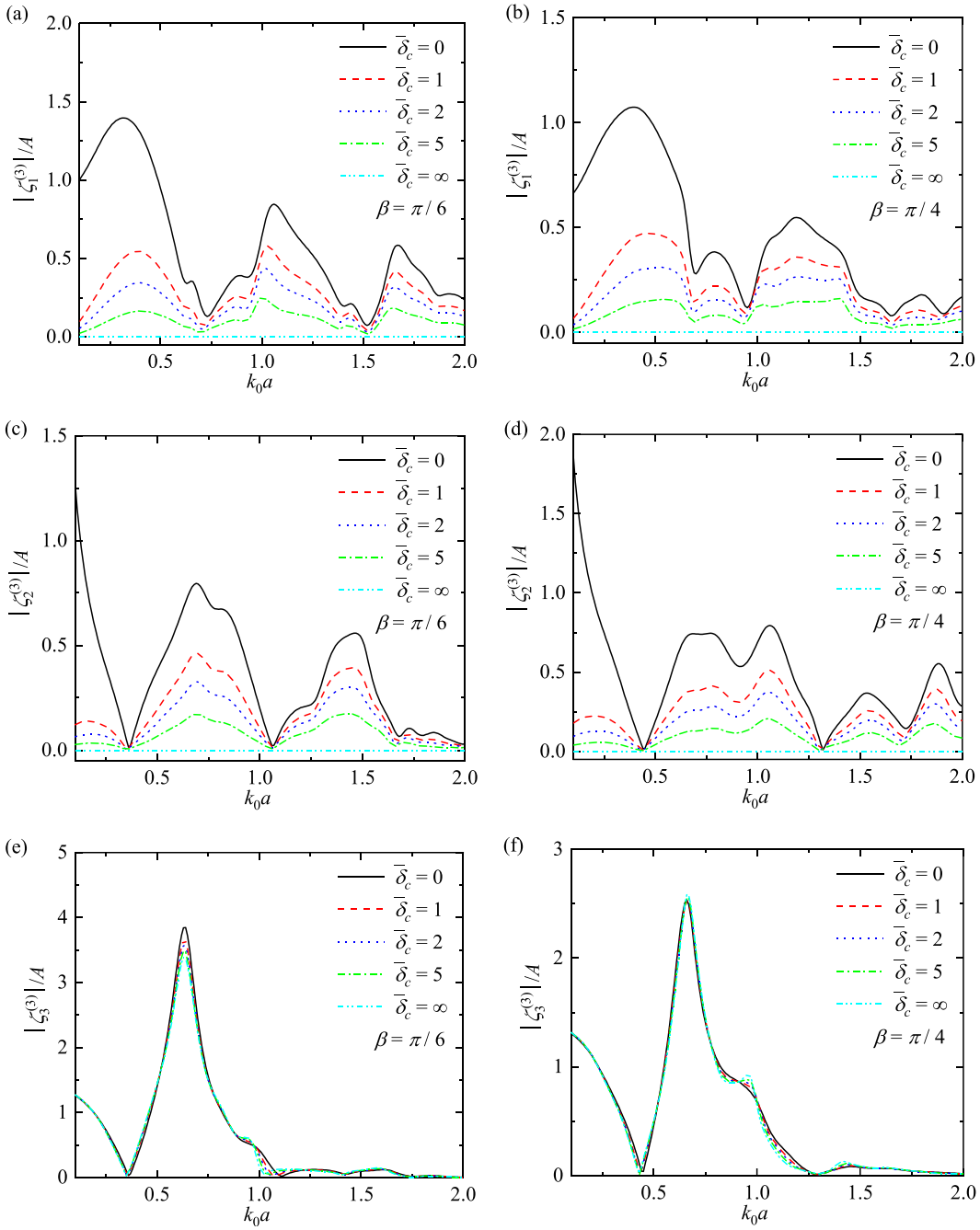

FIG. 27. Amplitude responses of each DOF for the middle buoy of the 5-WEC array with different equivalent stiffnesses: (a), (c), (e), (g), and (i) $\beta = \pi/6$; (b), (d), (f), (h), and (j) $\beta = \pi/4$.

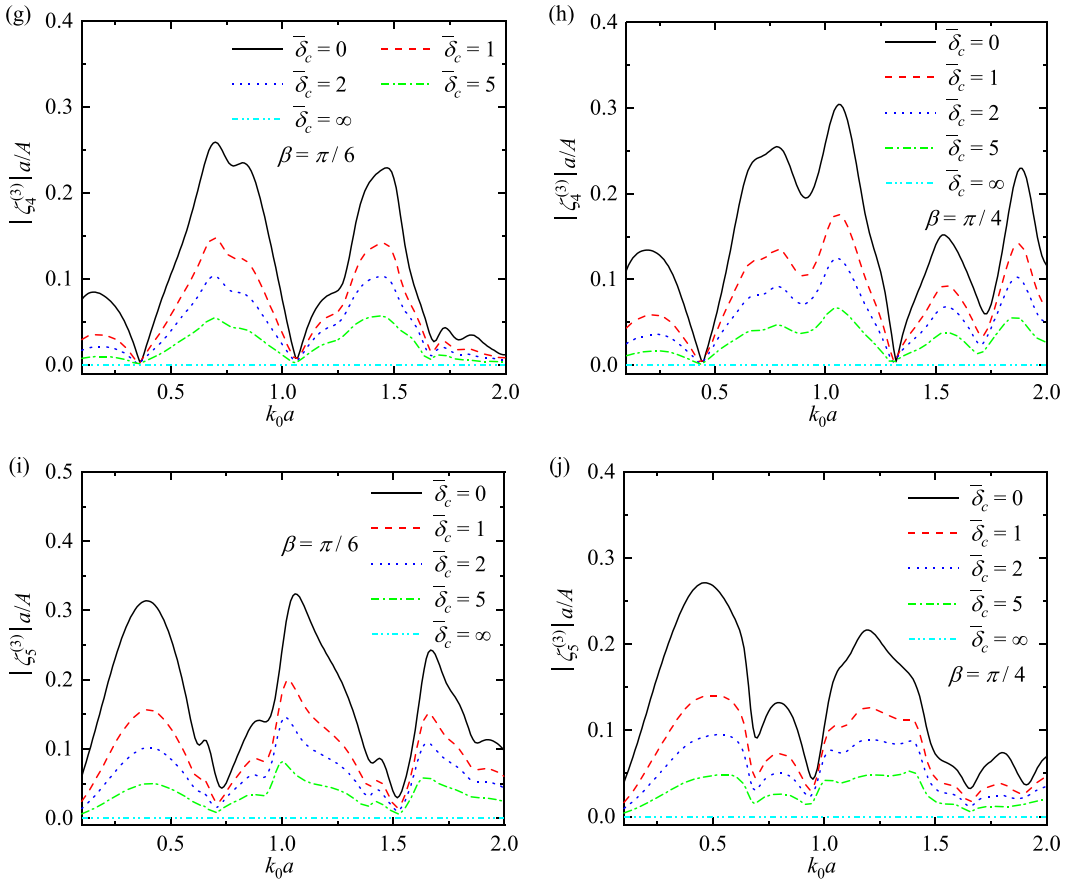

FIG. 27. (*Continued.*)

interaction among the buoys, the sway amplitude of each buoy fluctuates around the amplitude–frequency response curve of an isolated buoy as the wave number increases. For $\beta = \pi/2$, the direction of the ambient incident wave is parallel to the equidistant linear array consisting of five buoys, and buoy 1 is at the forefront. Figures 25(d) and 25(h) shows that the sway and roll amplitudes of buoy 1 are higher than those of other buoys in the WEC array within the wavenumber range of $0.1 < k_0a < 1.8$. However, the sway and roll amplitudes of buoy 5, located at the tail, are smaller than those of an isolated buoy within the entire dimensionless wavenumber range. It indicates that the hydrodynamic interaction creates a destructive impact on the performance of buoy 5.

For $\beta \leq \pi/4$, the variation trend of each buoy's amplitudes with dimensionless wavenumber is close to that of an isolated buoy within the low-frequency region ($k_0a < 0.5$ in this example), as shown in Figs. 23 and 24. It shows that the hydrodynamic interaction among the cylinders has little effect on the heave amplitude at these frequencies. As the incident angle β increases, there is a drastic hydrodynamic interaction in the low-frequency region, e.g., the pitch amplitude of the fifth buoy is 13.6% smaller than that of the first buoy for $k_0a = 0.29$ and $\beta = \pi/3$, as shown in Fig. 25(i); the heave amplitude of fifth buoy is 9.5% smaller than that of first buoy for $k_0a = 0.25$ and $\beta = \pi/3$, as shown in Fig. 25(e).

When the wavelength is short ($k_0a > 1.0$ in this example), the heave amplitude of each buoy is less than 0.5, as shown in Figs. 23(e), 23(f), 24(e), 24(f), 25(e), and 25(f). It shows that the energy extraction performance of the WEC array, which only extracts energy in the heave mode, is poor for the wave fields with the high-frequency region ($k_0a > 1.0$). Different from the heave mode, the dimensionless amplitudes of other DOFs still have large amplitudes within the high-frequency region ($k_0a > 1.0$), e.g., for $k_0a = 1.41$ and $\beta = 0$, the sway and roll amplitudes of buoy 1 (buoy 5) reach the maximum, as shown in Figs. 23(c) and 25(g); for $k_0a = 1.72$, $\beta = \pi/2$, the surge and pitch amplitudes of buoy 1 reach the maximum, as shown in Figs. 25(b) and 25(j).

The hydrodynamic performance of the cases with five equivalent stiffnesses ($\bar{\delta}_c = 0$, $\bar{\delta}_c = 1$, $\bar{\delta}_c = 2$, $\bar{\delta}_c = 5$, and $\bar{\delta}_c = \infty$) is investigated. As shown in Figs. 26–28, the variation curves of surge, sway, heave, roll, and pitch amplitudes with the dimensionless wavenumber k_0a for different incident angles are calculated. For simplicity, only the calculation results of the middle buoy (the third buoy) are plotted. Figure 29 shows the average capture width of the equidistant linear

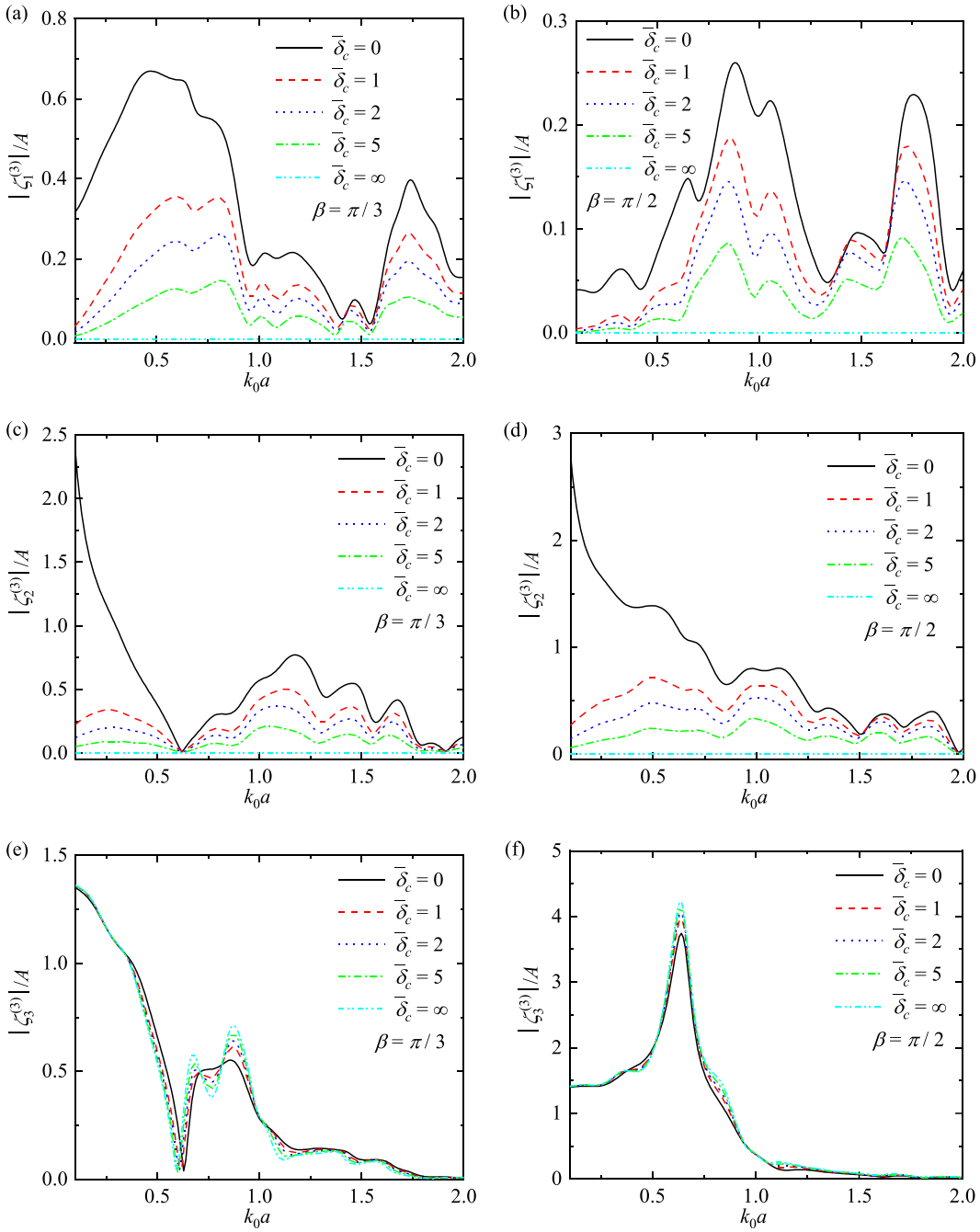

FIG. 28. Amplitude responses of each DOF for the middle buoy of the 5-WEC array with different equivalent stiffnesses: (a), (c), (e), (g), and (i) $\beta = \pi/3$; (b), (d), (f), (h), and (j) $\beta = \pi/2$.

WEC array consisting of five buoys near a vertical wall. The case of $\bar{\delta}_c = \infty$ is equivalent to the 1DOF model. Since the equidistant linear array is symmetrical about the x-axis, the sway and roll amplitudes are zero for the case of $\beta = 0$, as shown in Figs. 26(c) and 26(g).

As the equivalent constraint stiffness increases, the dimensionless amplitudes of other DOFs gradually decrease, as shown in Figs. 26(a), 26(b), 26(d), 26(h)–26(j), 27(a)–27(d), 27(g)–27(j), 28(a)–28(d), and 28(g)–28(j). The introduction of other DOFs makes the hydrodynamic interaction among the buoys and a vertical wall more complex. For the 5DOF model, the oscillation of each mode affects the heave amplitude of the buoys through hydrodynamic interaction and influences the energy extraction performance of the WEC array. As the equivalent

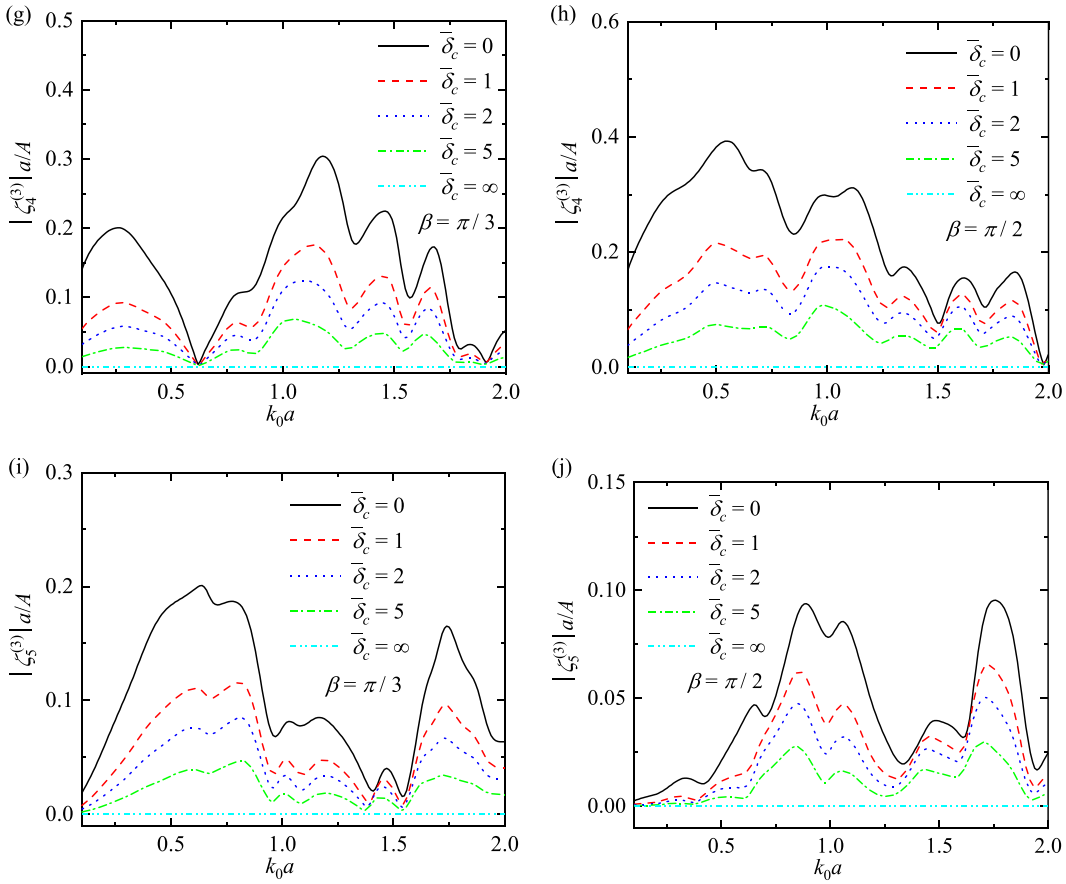

FIG. 28. (*Continued.*)

constraint stiffness increases, the dimensionless amplitudes of other DOFs gradually decrease, and the impact of the introduction of other DOFs on heave amplitude gradually decreases.

For $\beta \leq \pi/12$, the heave amplitudes and average capture widths of the 5DOF model and the 1DOF model ($\bar{\delta}_c = \infty$) are very close within the entire wavenumber range, as shown in Figs. 26(e) and 26(f), and 29(a) and 29(b). It shows that the hydrodynamic interaction generated by the oscillation of other DOFs has less influence on the energy extraction performance of the array that only extracts energy in the heave direction. Therefore, it is reasonable to utilize the 1DOF model for hydrodynamic analysis of the WEC array near a vertical wall. However, the impact of other DOFs on the hydrodynamic performance is strong for specific frequencies and incident angles, and the influence gradually decreases as the equivalent stiffness increases; e.g., for $\beta = \pi/3$ and $0.65 < k_0a < 1.02$, there is a difference of -62.0%–34.0% between the heave amplitudes of $\bar{\delta}_c = 0$ and $\bar{\delta}_c = \infty$, as shown in Fig. 28(e); for $\beta = \pi/6$, $k_0a = 0.62$, the average capture width of $\bar{\delta}_c = 0$ is 27.5% lower than that of $\bar{\delta}_c = \infty$, as shown in Fig. 29(e). For $k_0a > 1.0$, the heave amplitudes and average capture widths are relatively small, as shown in Figs. 26(e), 27(f), 27(e), 27(f), 28(e), 28(f), 29. It shows that the energy capture performance of the WEC array, which only extracts energy in the heave mode, is terrible for either the 5DOF model or the 1DOF model within the high-frequency region ($k_0a > 1.0$).

In general, when the buoys are at the crest of the standing wave, the heave amplitude has a large amplitude, while the amplitudes of other DOFs are relatively small. The spatial position of the standing wave crest changes continuously with incident angle and frequency. Therefore, the hydrodynamic performance closely relates to the dimensionless wavenumber and incident angle of the ambient wave. Additionally, interesting is that for $\beta \leq \pi/12$, there is no need to consider the impact of other DOFs on the energy extraction in heave mode. However, as the incident angle increases, the influence of other DOFs on hydrodynamic performance gradually increases within certain frequency ranges, and the impact gradually decreases with the increase in the equivalent stiffness. Within the high-frequency region ($k_0a > 1.0$), the heave amplitude becomes significantly smaller, but the amplitudes of other DOFs still have considerable magnitudes. Therefore, for the sea area with high-frequency incident waves ($k_0a > 1.0$), setting up a PTO system on other DOFs (surge, sway, roll, and pitch) of each buoy to extract energy is a feasible solution to improve the performance of the WEC array.

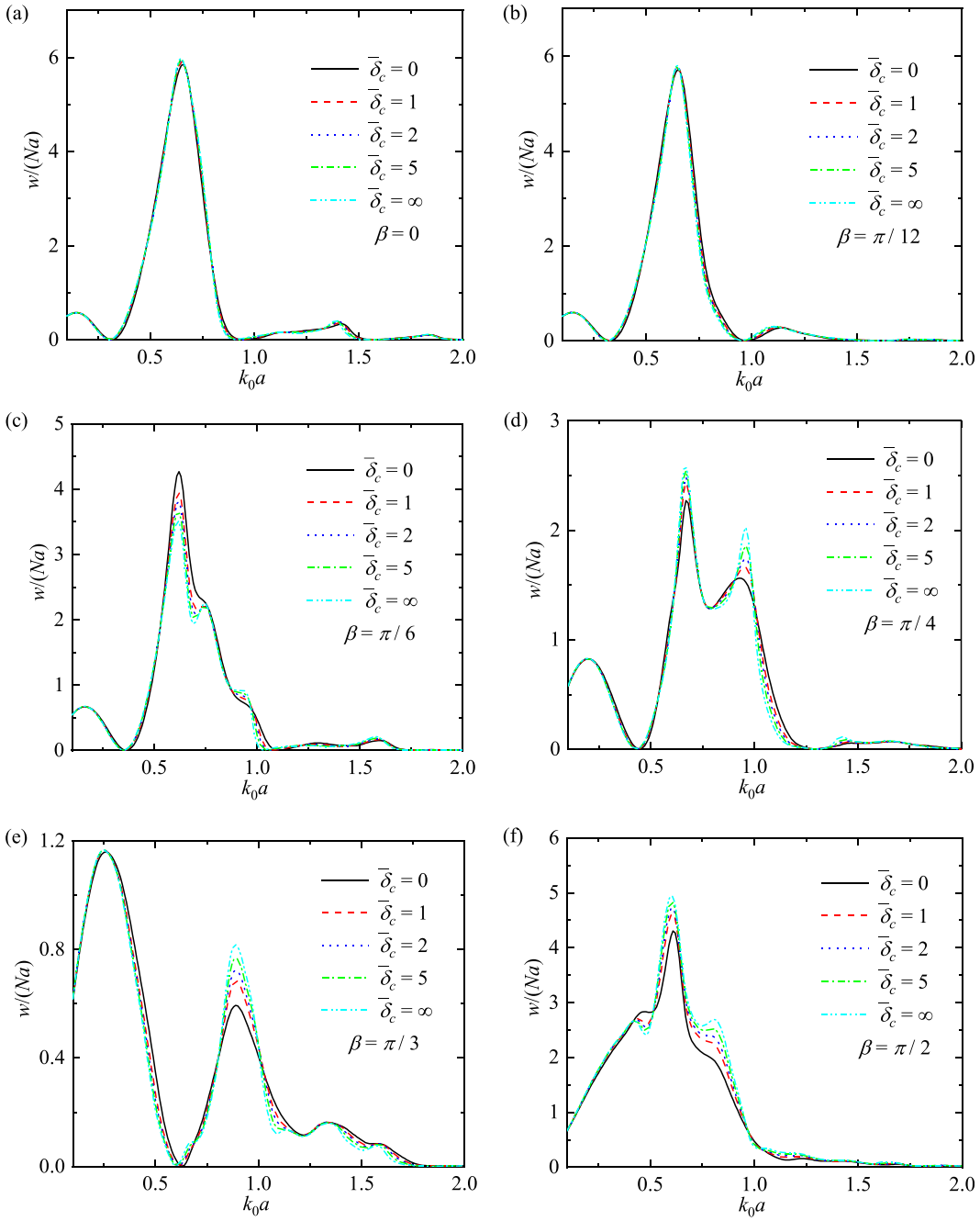

FIG. 29. Average capture widths for the 5-WEC array with different equivalent stiffnesses: (a) $\beta = 0$; (b) $\beta = \pi/12$; (c) $\beta = \pi/6$; (d) $\beta = \pi/4$; (e) $\beta = \pi/3$; (f) $\beta = \pi/2$.

VII. CONCLUSION

This paper mainly investigates the hydrodynamic analysis and layout optimization of the WEC array in front of a fully reflecting vertical wall. All buoys in the array are modeled as truncated floating cylinders that can oscillate with five degrees of freedom, i.e., surge, sway, heave, roll, and pitch. Based on the linear water wave theory, an analytical solution is developed for the hydrodynamic problem. The correctness of the analytical solution is verified by comparing it with existing research results.

Based on the obtained hydrodynamic analysis model, specific parameter studies are conducted. For two identical buoys with a sufficiently large spacing (e.g., $L/a = 12$), the hydrodynamic interaction has

little impact on the energy extraction performance. The results suggest that the reflection effect and the hydrodynamic interaction among buoys on the hydrodynamic performance become more complex as the number of buoys increases. The reflection effect of a vertical wall can significantly improve the energy extraction performance of the WEC array. For some buoys, the hydrodynamic interaction has a constructive effect on the energy capture performance. However, the hydrodynamic interaction may also impose destructive effects on the part of buoys for some conditions.

A multi-level optimization method based on a genetic algorithm is developed. Based on the two-level optimization with two different grid spacings, this paper investigates the optimal layout of the six WEC arrays, composed of 2–7 buoys, respectively, and plots the corresponding contour plots of free surface elevation. These results show that the average capture width gradually increases as the number of buoys increases, but the increase rate gradually decreases. Compared with the optimal layout of published literature in an open water domain, this paper obtains an optimized WEC array with higher energy extraction performance by using the multi-level optimization method. In addition, the performance of these optimal arrays with different incident angles and dimensionless wavenumbers is also conducted.

The impact of other DOFs, besides the heave mode, on the hydrodynamic performance of the WEC array near a vertical wall is investigated. For the six optimal arrays, the average capture widths of the WEC arrays increase as the equivalent stiffnesses of other DOFs decrease. Nevertheless, the energy extraction performance improves little because buoys are close to the crest of the standing wave field and mainly oscillate in heave mode. The dimensionless amplitudes of other DOFs gradually decrease as the equivalent constraint stiffness increases. For $\beta \leq \pi/12$, there is no need to consider the impact of other DOFs on the energy extraction in heave mode. As the incident angle increases, the influence of other DOFs on hydrodynamic performance gradually increases within certain frequency ranges, and the impact gradually decreases with the increase in the equivalent stiffness. For $k_0 a > 1.0$, the energy capture performance of the WEC array, which only extracts energy in the heave mode, is terrible for either the 5DOF model or the 1DOF model. However, the amplitudes of other DOFs still have considerable magnitudes within the high-frequency region. Therefore, for the sea area with high-frequency incident waves ($k_0 a > 1.0$), setting up a PTO system on other DOFs (surge, sway, roll, and pitch) of each buoy to extract energy is a feasible solution to improve the performance of the WEC array.

This paper studies the hydrodynamic interactions between regular waves and cylindrical arrays in front of a vertical wall, which can be extended to the case of irregular waves. This extension goes beyond the scope of this paper and will be carried out in future work.

ACKNOWLEDGMENTS

This work was supported by the National Natural Science Foundation of China (Grant Nos. 12372051 and 11672306) and the National Key Research and Development Program of China (Grant No. 2022YFB4201500).

AUTHOR DECLARATIONS

Conflict of Interest

The authors have no conflicts to disclose.

Author Contributions

Yuanshun Kang: Conceptualization (lead); Data curation (lead); Formal analysis (lead); Investigation (lead); Methodology (lead); Software (lead); Validation (lead); Visualization (lead); Writing – original draft (equal); Writing – review & editing (equal). **Xiaohui Zeng:** Conceptualization (lead); Funding acquisition (lead); Methodology (lead); Supervision (lead); Writing – original draft (equal); Writing – review & editing (equal). **Zhehua Cui:** Data curation (equal); Validation (equal); Writing – review & editing (equal). **Jiahao Chen:** Validation (equal); Writing – review & editing (equal).

DATA AVAILABILITY

The data support the finding of this study are available from the corresponding author upon reasonable request.

APPENDIX A: CALCULATION OF UNKNOWN COEFFICIENTS

The elements of diffraction transfer matrix $\mathbf{B}_j^{\mathrm{E}}$ and $\mathbf{B}_j^{\mathrm{C}}$ for an isolated cylinder are as follows:

$$\mathbf{B}_j^{\mathrm{E}}(0,0,m) = -\frac{J'_m(k_0 a_j)}{H'_m(k_0 a_j)} + \frac{D^n_{mq}\cosh k_0 d}{H'_m(k_0 a_j) N_0^{1/2} e^{im(\pi/2-\beta)}} \quad (n=0, q=0), \tag{A1}$$

$$\mathbf{B}_j^{\mathrm{E}}(q,0,m) = \frac{D^n_{mq}}{K'_m(k_q a_j) N_q^{1/2} e^{im(\pi/2-\beta)}} \quad (n=0, q\geq 1), \tag{A2}$$

$$\mathbf{B}_j^{\mathrm{E}}(0,n,m) = \frac{D^n_{m0}\cosh k_0 d}{H'_m(k_0 a_j) N_0^{1/2}} \quad (n\geq 1, q=0), \tag{A3}$$

$$\mathbf{B}_j^{\mathrm{E}}(q,n,m) = \begin{cases} \dfrac{D^n_{mq}}{K'_m(k_q a_j) N_q^{1/2}} \\ \quad (n\geq 1, q\geq 1, q\neq n), \\ -\dfrac{I'_m(k_q a_j)}{K'_m(k_q a_j)} + \dfrac{D^n_{mq}}{K'_m(k_q a_j) N_q^{1/2}} \\ \quad (n\geq 1, q\geq 1, q=n), \end{cases} \tag{A4}$$

$$\mathbf{B}_j^{\mathrm{C}}(0,0,m) = \frac{C^n_{m0}}{2a_j^{|m|} i^m} \quad (n=0, p=0), \tag{A5}$$

$$\mathbf{B}_j^{\mathrm{C}}(p,0,m) = \frac{C^n_{mp}}{I_m\left(p\pi a_j/(d-h)\right) i^m} \cdot \cos\left(\frac{p\pi(z+d)}{d-h}\right) \quad (n=0, p\geq 1), \tag{A6}$$

$$\mathbf{B}_j^{\mathrm{C}}(0,n,m) = \frac{C^n_{m0}}{2a_j^{|m|}} \quad (n\geq 1, p=0), \tag{A7}$$

$$\mathbf{B}_j^{\mathrm{C}}(p,n,m) = \frac{C^n_{mp}}{\mathrm{I}_m\left(p\pi a_j/(d-h)\right)} \cdot \cos\left(\frac{p\pi(z+d)}{d-h}\right) \quad (n\geq 1, p\geq 1), \tag{A8}$$

where C^n_{mp} and D^n_{mq} are obtained by solving

$$\begin{cases} C_{mp}^{n} + \sum_{q=0}^{\infty} F_{mpq} D_{mq}^{n} = R_{mp}^{n}, \\ D_{mq}^{n} - \sum_{p=0}^{\infty} G_{mqp} C_{mp}^{n} = 0, \end{cases} \tag{A9}$$

with

$$F_{mpq} = \begin{cases} -\dfrac{2H_m(k_0 a_j)k_0(d-h)(-1)^p \sinh k_0(d-h)}{H_m'(k_0 a_j)\cdot N_0^{1/2}\cdot\left[k_0{}^2(d-h)^2 + p^2\pi^2\right]} & (q=0), \\ -\dfrac{2K_m(k_q a_j)k_q(d-h)(-1)^p \sin k_q(d-h)}{K_m'(k_q a_j)\cdot N_q^{1/2}\cdot\left[k_q{}^2(d-h)^2 - p^2\pi^2\right]} & (q\geq 1), \end{cases} \tag{A10}$$

$$G_{mqp} = \begin{cases} \dfrac{|m|\cdot \sin k_q(d-h)}{2a_j\cdot d\cdot k_q{}^2 N_q^{1/2}} & (p=0), \\ \dfrac{I_m'\left(\dfrac{p\pi a_j}{d-h}\right)\cdot p\pi(d-h)(-1)^p\cdot \sin k_q(d-h)}{I_m\left(\dfrac{p\pi a_j}{d-h}\right)\cdot d\cdot N_q^{1/2}\cdot\left[k_q{}^2(d-h)^2 - p^2\pi^2\right]} & (p\geq 1), \end{cases} \tag{A11}$$

$$R_{mp}^{n} = \begin{cases} 2i^m\left[J_m(k_0 a_j) - \dfrac{J_m'(k_0 a_j)}{H_m'(k_0 a_j)}H_m(k_0 a_j)\right] \\ \quad\cdot\dfrac{(-1)^p\cdot k_0(d-h)\sinh k_0(d-h)}{\cosh k_0 d\cdot\left[k_0{}^2(d-h)^2 + p^2\pi^2\right]} & (n=0), \\ 2\left[I_m(k_n a_j) - \dfrac{I_m'(k_n a_j)}{K_m'(k_n a_j)}K_m(k_n a_j)\right] \\ \quad\cdot\dfrac{(-1)^p k_n(d-h)\sin k_n(d-h)}{k_n{}^2(d-h)^2 - p^2\pi^2} & (n\geq 1). \end{cases} \tag{A12}$$

Similar to (A9), $C_{R_{pm}^{s}}$ and $D_{R_{nm}^{s}}$ can be solved from the following equations:

$$\begin{cases} C_{R_{pm}^{s}} + \sum_{q=0}^{\infty} F_{mpq} D_{R_{qm}^{s}} = R_{R_{pm}^{s}}, \\ D_{R_{qm}^{s}} - \sum_{p=0}^{\infty} G_{mqp} C_{R_{pm}^{s}} = S_{R_{qm}^{s}} \end{cases} \tag{A13}$$

with

$$R_{R_{pm}^{s}} = -\frac{2}{d-h}\int_{-d}^{-h} \lambda_{ms}\Lambda_s(a_j, z)\cos\left[\frac{p\pi(z+d)}{d-h}\right]dz, \tag{A14}$$

$$S_{R_{qm}^{s}} = \frac{\lambda_{ms}}{k_q d}\int_{-d}^{-h}\frac{\partial\Lambda_s(a_j,z)}{\partial r}Z_q(z)dz + \frac{\lambda_{ms}}{k_q d}\int_{-h}^{0} f_s(z)Z_q(z)dz, \tag{A15}$$

where

$$f_s(z) = \begin{cases} 1 & (s=1,2), \\ 0 & (s=3), \\ -(z-\bar{z}) & (s=4), \\ (z-\bar{z}) & (s=5), \end{cases} \tag{A16}$$

$$\Lambda_s = \begin{cases} 0 & (s=1,2), \\ \dfrac{1}{2(d-h)}\left[(z+d)^2 - \dfrac{r_j^2}{2}\right] & (s=3), \\ \dfrac{r_j}{2(d-h)}\left[(z+d)^2 - \dfrac{r_j^2}{2}\right] & (s=4), \\ -\dfrac{r_j}{2(d-h)}\left[(z+d)^2 - \dfrac{r_j^2}{4}\right] & (s=5), \end{cases} \tag{A17}$$

$$\lambda_{ms} = \begin{cases} m=1: \begin{cases} \lambda_{11} = \lambda_{15} = \dfrac{1}{2}, \\ \lambda_{13} = 0, \\ \lambda_{12} = \lambda_{14} = \dfrac{1}{2i}, \end{cases} ; \quad m=0: \begin{cases} \lambda_{01} = \lambda_{05} = 0, \\ \lambda_{03} = 1, \\ \lambda_{02} = \lambda_{04} = 0, \end{cases} \\ m=-1: \begin{cases} \lambda_{-11} = \lambda_{-15} = \dfrac{1}{2}, \\ \lambda_{-13} = 0, \\ \lambda_{-12} = \lambda_{-14} = -\dfrac{1}{2i}, \end{cases} ; \ m = \text{others}: \lambda_{ms} = 0. \end{cases} \tag{A18}$$

APPENDIX B: SPECIFIC FORMS OF THE HYDRODYNAMIC FORCE

The specific forms of the hydrodynamic force of cylinder j are as follows:

Surge:

$$\begin{aligned} \mathcal{F}_{RD1}^{(j)} &= i\omega_0\rho\int_0^{2\pi}\int_{-h_j}^{0}\varphi_{RD-E}^{(j)}|_{r=a_j}(-\cos\theta_j)a_j d\theta_j dz \\ &= i\omega_0\rho\int_0^{2\pi}\int_{-h_j}^{0} i\omega_0\sum_{s=1}^{5}\left(\zeta_s^{(j)}\varphi_{RD-Es}^{(jj)} + \sum_{k=1,k\neq j}^{N}\zeta_s^{(k)}\varphi_{RD-Es}^{(jk)}\right)\Big|_{r=a_j} \\ &\quad\times\cos\theta_j a_j d\theta_j dz \\ &= \sum_{s=1}^{5}\left[\zeta_s^{(j)}\left(-\omega_0{}^2\rho\int_0^{2\pi}\int_{-h_j}^{0}\varphi_{RD-Es}^{(jj)}|_{r=a_j}\cos\theta_j a_j d\theta_j dz\right)\right. \\ &\quad\left.+\sum_{k=1,k\neq j}^{N}\zeta_s^{(k)}\left(-\omega_0{}^2\rho\int_0^{2\pi}\int_{-h_j}^{0}\varphi_{RD-Es}^{(jk)}|_{r=a_j}\cos\theta_j a_j d\theta_j dz\right)\right] \\ &= \sum_{s=1}^{5}\left(\zeta_s^{(j)}F_{RD1s}^{(jj)} + \sum_{k=1,k\neq j}^{N}\zeta_s^{(k)}F_{RD1s}^{(jk)}\right) = \sum_{s=1}^{5}\sum_{i=1}^{N}F_{RD1s}^{(ji)}\zeta_s^{i}, \end{aligned} \tag{B1}$$

Sway:

$$\begin{aligned}\mathcal{F}_{RD2}^{(j)} &= \mathrm{i}\omega_0\rho\int_0^{2\pi}\int_{-h_j}^{0}\varphi_{RD-E}^{(j)}|_{r=a_j}(-\sin\theta_j)a_j d\theta_j dz\\ &= \mathrm{i}\omega_0\rho\int_0^{2\pi}\int_{-h_j}^{0}\mathrm{i}\omega_0\sum_{s=1}^{5}\left(\zeta_s^{(j)}\varphi_{RD-Es}^{(jj)}+\sum_{k=1,k\neq j}^{N}\zeta_s^{(k)}\varphi_{RD-Es}^{(jk)}\right)\Bigg|_{r=a_j}\sin\theta_j a_j d\theta_j dz\\ &= \sum_{s=1}^{5}\left[\zeta_s^{(j)}\left(-{\omega_0}^2\rho\int_0^{2\pi}\int_{-h_j}^{0}\varphi_{RD-Es}^{(jj)}|_{r=a_j}\sin\theta_j a_j d\theta_j dz\right)+\sum_{k=1,k\neq j}^{N}\zeta_s^{(k)}\left(-{\omega_0}^2\rho\int_0^{2\pi}\int_{-h_j}^{0}\varphi_{RD-Es}^{(jk)}|_{r=a_j}\sin\theta_j a_j d\theta_j dz\right)\right]\\ &= \sum_{s=1}^{5}\left(\zeta_s^{(j)}F_{RD2s}^{(jj)}+\sum_{k=1,k\neq j}^{N}\zeta_s^{(k)}F_{RD2s}^{(jk)}\right)=\sum_{s=1}^{5}\sum_{i=1}^{N}F_{RD2s}^{(ji)}\zeta_s^{i},\end{aligned}\tag{B2}$$

Heave:

$$\begin{aligned}\mathcal{F}_{RD3}^{(j)} &= \mathrm{i}\omega_0\rho\int_0^{2\pi a_j}\int_0^{2\pi a_j}\varphi_{RD-C}^{(j)}|_{z=-h_j}r_j dr_j d\theta_j\\ &= -\mathrm{i}\omega_0\rho\int_0^{2\pi a_j}\int_0^{2\pi a_j}\mathrm{i}\omega_0\sum_{s=1}^{5}\left(\zeta_s^{(j)}\varphi_{RD-Cs}^{(jj)}+\sum_{k=1,k\neq j}^{N}\zeta_s^{(k)}\varphi_{RD-Cs}^{(jk)}\right)\Bigg|_{z=-h_j}r_j dr_j d\theta_j\\ &= \sum_{s=1}^{5}\left[\zeta_s^{(j)}\left({\omega_0}^2\rho\int_0^{2\pi a_j}\int_0^{2\pi a_j}\varphi_{RD-Cs}^{(jj)}|_{z=-h_j}r_j dr_j d\theta_j\right)+\sum_{k=1,k\neq j}^{N}\zeta_s^{(k)}\left({\omega_0}^2\rho\int_0^{2\pi a_j}\int_0^{2\pi a_j}\varphi_{RD-Cs}^{(jk)}|_{z=-h_j}r_j dr_j d\theta_j\right)\right]\\ &= \sum_{s=1}^{5}\left(\zeta_s^{(j)}F_{RD3s}^{(jj)}+\sum_{k=1,k\neq j}^{N}\zeta_s^{(k)}F_{RD3s}^{(jk)}\right)=\sum_{s=1}^{5}\sum_{i=1}^{N}F_{RD3s}^{(ji)}\zeta_s^{i},\end{aligned}\tag{B3}$$

Roll:

$$\begin{aligned}\mathcal{F}_{RD4}^{(j)} &= \mathrm{i}\omega_0\rho\left(\int_0^{2\pi a_j}\int_0^{2\pi a_j}\varphi_{RD-C}^{j}|_{z=-h_j}{r_j}^2\sin\theta_j dr_j d\theta_j+\int_0^{2\pi}\int_{-h}^{0}\varphi_{RD-E}^{j}|_{r=a_j}(z-\bar{z}_j)a_j\sin\theta_j d\theta_j dz\right)\\ &= -\mathrm{i}\omega_0\rho\left[\int_0^{2\pi a_j}\int_0^{2\pi a_j}\mathrm{i}\omega_0\sum_{s=1}^{5}\left(\zeta_s^{(j)}\varphi_{RD-Cs}^{(jj)}+\sum_{k=1,k\neq j}^{N}\zeta_s^{(k)}\varphi_{RD-Cs}^{(jk)}\right)\Bigg|_{z=-h_j}{r_j}^2\sin\theta_j dr_j d\theta_j\right.\\ &\quad\left.+\int_0^{2\pi}\int_{-h_j}^{0}\mathrm{i}\omega_0\sum_{s=1}^{5}\left(\zeta_s^{(j)}\varphi_{RD-Es}^{(jj)}+\sum_{k=1,k\neq j}^{N}\zeta_s^{(k)}\varphi_{RD-Es}^{(jk)}\right)\Bigg|_{r=a_j}(z-\bar{z}_j)a_j\sin\theta_j d\theta_j dz\right]\\ &= \sum_{s=1}^{5}\left[\zeta_s^{(j)}\left({\omega_0}^2\rho\int_0^{2\pi a_j}\int_0^{2\pi a_j}\varphi_{RD-Cs}^{(jj)}|_{z=-h_j}{r_j}^2\sin\theta_j dr_j d\theta_j+{\omega_0}^2\rho\int_0^{2\pi}\int_{-h_j}^{0}\varphi_{RD-Es}^{(jj)}|_{r=a_j}(z-\bar{z}_j)a_j\sin\theta_j d\theta_j dz\right)\right.\\ &\quad\left.+\sum_{k=1,k\neq j}^{N}\zeta_s^{(k)}\left({\omega_0}^2\rho\int_0^{2\pi a_j}\int_0^{2\pi a_j}\varphi_{RD-Cs}^{(jk)}|_{z=-h_j}{r_j}^2\sin\theta_j dr_j d\theta_j+{\omega_0}^2\rho\int_0^{2\pi}\int_{-h_j}^{0}\varphi_{RD-Es}^{(jk)}|_{r=a_j}(z-\bar{z}_j)a_j\sin\theta_j d\theta_j dz\right)\right]\\ &= \sum_{s=1}^{5}\left(\zeta_s^{(j)}F_{RD4s}^{(jj)}+\sum_{k=1,k\neq j}^{N}\zeta_s^{(k)}F_{RD4s}^{(jk)}\right)=\sum_{s=1}^{5}\sum_{i=1}^{N}F_{RD4s}^{(ji)}\zeta_s^{i},\end{aligned}\tag{B4}$$

Pitch:

$$\begin{aligned}\mathcal{F}_{RD5}^{(j)} &= \mathrm{i}\omega_0\rho\left(-\int_0^{2\pi}\int_0^{a_j}\varphi_{RD-C}^{j}|_{z=-h_j} r_j^2\cos\theta_j dr_j d\theta_j - \int_0^{2\pi}\int_{-h_j}^{0}\varphi_{RD-E}^{j}|_{r=a_j}(z-\bar{z}_j)a_j\cos\theta_j d\theta_j dz\right)\\ &= \mathrm{i}\omega_0\rho\left[\int_0^{2\pi}\int_0^{a_j}\mathrm{i}\omega_0\sum_{s=1}^{5}\left(\zeta_s^{(j)}\varphi_{RD-Cs}^{(jj)} + \sum_{k=1,k\neq j}^{N}\zeta_s^{(k)}\varphi_{RD-Cs}^{(jk)}\right)\Big|_{z=-h_j} r_j^2\cos\theta_j dr_j d\theta_j\right.\\ &\quad \left.+\int_0^{2\pi}\int_{-h_j}^{0}\mathrm{i}\omega_0\sum_{s=1}^{5}\left(\zeta_s^{(j)}\varphi_{RD-Es}^{(jj)} + \sum_{k=1,k\neq j}^{N}\zeta_s^{(k)}\varphi_{RD-Es}^{(jk)}\right)\Big|_{r=a_j}(z-\bar{z}_j)a_j\cos\theta_j d\theta_j dz\right]\\ &= \sum_{s=1}^{5}\left[\zeta_s^{(j)}\left(-{\omega_0}^2\rho\int_0^{2\pi}\int_0^{a_j}\varphi_{RD-Cs}^{(jj)}|_{z=-h_j} r_j^2\cos\theta_j dr_j d\theta_j - {\omega_0}^2\rho\int_0^{2\pi}\int_{-h_j}^{0}\varphi_{RD-Es}^{(jj)}|_{r=a_j}(z-\bar{z}_j)a_j\cos\theta_j d\theta_j dz\right)\right.\\ &\quad \left.+\sum_{k=1,k\neq j}^{N}\zeta_s^{(k)}\left(-{\omega_0}^2\rho\int_0^{2\pi}\int_0^{a_j}\varphi_{RD-Cs}^{(jk)}|_{z=-h_j} r_j^2\cos\theta_j dr_j d\theta_j - {\omega_0}^2\rho\int_0^{2\pi}\int_{-h_j}^{0}\varphi_{RD-Es}^{(jk)}|_{r=a_j}(z-\bar{z}_j)a_j\cos\theta_j d\theta_j dz\right)\right]\\ &= \sum_{s=1}^{5}\left(\zeta_s^{(j)}F_{RD5s}^{(jj)} + \sum_{k=1,k\neq j}^{N}\zeta_s^{(k)}F_{RD5s}^{(jk)}\right) = \sum_{s=1}^{5}\sum_{i=1}^{N}F_{RD5s}^{(ji)}\zeta_s^{i}.\end{aligned} \tag{B5}$$

REFERENCES

Balitsky, P., Verao Fernandez, G., Stratigaki, V., and Troch, P., "Assessment of the power output of a two-array clustered WEC farm using a BEM solver coupling and a wave-propagation model," Energies **11**(11), 2907 (2018).

Chanda, A. and Bora, S. N., "Effect of a porous sea-bed on water wave scattering by two thin vertical submerged porous plates," Eur. J. Mech. B **84**, 250–261 (2020).

Chanda, A., Sarkar, A., and Bora, S. N., "An analytical study of scattering of water waves by a surface-piercing bottom-mounted compound porous cylinder placed on a porous sea-bed," J. Fluids Struct. **115**, 103764 (2022).

Chanda, A. and Bora, S. N., "Scattering of flexural gravity waves by a pair of submerged vertical porous barriers located above a porous sea-bed," J. Offshore Mech. Arct. Eng. **144**(1), 011201 (2022).

Chanda, A. and Pramanik, S., "Effects of a thin vertical porous barrier on the water wave scattering by a porous breakwater," Phys. Fluids **35**(6), 062120 (2023).

Chen, J. T., Lin, Y. J., Lee, Y. T., and Wu, C. F., "Water wave interaction with surface-piercing porous cylinders using the null-field integral equations," Ocean Eng. **38**(2–3), 409–418 (2011).

Child, B. F. M. and Venugopal, V., "Optimal configurations of wave energy device arrays," Ocean Eng. **37**(16), 1402–1417 (2010).

Cong, P., Chen, L., and Gou, Y., "Hydrodynamic interaction among multiple columns in front of a vertical wall," Ocean Eng. **197**, 106877 (2020).

Dafnakis, P., Bhalla, A. P. S., Sirigu, S. A., Bonfanti, M., Bracco, G., and Mattiazzo, G., "Comparison of wave–structure interaction dynamics of a submerged cylindrical point absorber with three degrees of freedom using potential flow and computational fluid dynamics models," Phys. Fluids **32**(9), 093307 (2020).

Fang, H. W., Feng, Y. Z., and Li, G. P., "Optimization of wave energy converter arrays by an improved differential evolution algorithm," Energies **11**(12), 3522 (2018).

Falnes, J., *Ocean Waves and Oscillating Systems, Linear Interactions Including Wave-Energy Extraction*, 1st ed. (Cambridge University Press, Cambridge, 2002).

Flavia, F. F. and Meylan, M. H., "An extension of general identities for 3D water-wave diffraction with application to the diffraction transfer matrix," Appl. Ocean Res. **84**, 279–290 (2019).

Giassi, M. and Göteman, M., "Layout design of wave energy parks by a genetic algorithm," Ocean Eng. **154**, 252–261 (2018).

He, F., Huang, Z., and Law, A. W. K., "An experimental study of a floating breakwater with asymmetric pneumatic chambers for wave energy extraction," Appl. Energy **106**, 222–231 (2013).

Holland, J. H., *Adaptation in Natural and Artificial Systems* (University of Michigan Press, Ann Arbor, 1975).

Ioannou, R. and Loukogeorgaki, E., "Optimum layouts of a cluster of heaving point absorbers in front of wall-type coastal structures under regular wave attack," J. Coastal Hydraul. Struct. **1**, 1–17 (2021).

Kagemoto, H. and Yue, D., "Interactions among multiple three-dimensional bodies in water waves: An exact algebraic method," J. Fluid Mech. **166**, 189–209 (1986).

Kara, F., "Hydrodynamic performances of wave energy converter arrays in front of a vertical wall," Ocean Eng. **235**, 109459 (2021).

Kara, F., "Effects of a vertical wall on wave power absorption with wave energy converters arrays," Renewable Energy **196**, 812–823 (2022).

Konispoliatis, D. N., Mavrakos, S. A., and Katsaounis, G. M., "Theoretical evaluation of the hydrodynamic characteristics of arrays of vertical axisymmetric floaters of arbitrary shape in front of a vertical breakwater," J. Mar. Sci. Eng. **8**(1), 62 (2020).

Konispoliatis, D. N., "Assessment of the hydrodynamic performance of an oscillating water column device in front of a v-shaped vertical wall," J. Offshore Mech. Arct. Eng. **145**(5), 052001 (2023).

Li, A. J. and Liu, Y., "Hydrodynamic performance and energy absorption of multiple spherical absorbers along a straight coast," Phys. Fluids **34**(11), 117102 (2022).

Li, A. J., Liu, Y., and Fang, H., "Wave scattering by porous cylinders with inner columns near a vertical wall," Phys. Fluids **35**(8), 087111 (2023).

Liu, Y., Zheng, S., Liang, H., and Cong, P., "Wave interaction and energy absorption from arrays of complex-shaped point absorbers," Phys. Fluids **34**(9), 097107 (2022).

Linton, C. M. and Evans, D. V., "The interaction of waves with arrays of vertical circular cylinders," J. Fluid Mech. **215**, 549–569 (1990).

Loukogeorgaki, E., and Chatjigeorgiou, I. K., "Hydrodynamic performance of an array of truncated cylinders in front of a vertical wall," Ocean Eng. **189**, 106407 (2019).

Loukogeorgaki, E., Michailides, C., Lavidas, G., and Chatjigeorgiou, I. K., "Layout optimization of heaving wave energy converters linear arrays in front of a vertical wall," Renewable Energy **179**, 189–203 (2021).
Mavrakos, S. A., and McIver, P., "Comparison of methods for computing hydrodynamic characteristics of arrays of wave power devices," Appl. Ocean Res. **19**(5–6), 283–291 (1997).
McGuinness, J. P., and Thomas, G., "Hydrodynamic optimisation of small arrays of heaving point absorbers," J. Ocean Eng. Mar. Energy **2**(4), 439–457 (2016).
McIver, P. and Evans, D. V., "Approximate theory for the performance of a number of wave-energy devices set into a reflecting wall," Appl. Ocean Res.**10**(2), 58 (1988).
Mercadé Ruiz, P., Nava, V., Topper, M. B., Ruiz Minguela, P., Ferri, F., and Kofoed, J. P., "Layout optimisation of wave energy converter arrays," Energies **10**(9), 1262 (2017).
Mustapa, M. A., Yaakob, O. B., Ahmed, Y. M., Rheem, C. K., Koh, K. K., and Adnan, F. A., "Wave energy device and breakwater integration: A review," Renewable Sustainable Energy Rev. **77**, 43–58 (2017).
Neshat, M., Abbasnejad, E., Shi, Q., Alexander, B., and Wagner, M., "Adaptive neuro-surrogate-based optimisation method for wave energy converters placement optimization," in *Proceedings of Neural Information Processing: 26th International Conference, ICONIP 2019, Sydney, NSW, Australia, December 12–15, 2019* (Springer International Publishing, 2019), Vol. 26, Part II, pp. 353–366.
Okhusu, M., "Hydrodynamic forces on multiple cylinders in waves," in *International Symposium on the Dynamics of Marine Vehicles and Structures in Waves* (University College London, London, 1974), Paper No. 12, pp. 107–112.
Parrinello, L., Dafnakis, P., Pasta, E., Bracco, G., Naseradinmousavi, P., Mattiazzo, G., and Bhalla, A. P. S., "An adaptive and energy-maximizing control optimization of wave energy converters using an extremum-seeking approach," Phys. Fluids **32**(11), 113307 (2020).
Sarkar, A., and Chanda, A., "Structural performance of a submerged bottom-mounted compound porous cylinder on the water wave interaction in the presence of a porous sea-bed," Phys. Fluids **34**(9), 092113 (2022).
Sharp, C. and DuPont, B., "Wave energy converter array optimization: A genetic algorithm approach and minimum separation distance study," Ocean Eng. **163**, 148–156 (2018).
Spring, B. H. and Monkmeyer, P. L., "Interaction of plane waves with vertical cylinders," Coastal Eng. **1974**, 1828–1847 (1974).
Teng, B., Ning, D. Z., and Zhang, X. T., "Wave radiation by a uniform cylinder in front of a vertical wall," Ocean Eng. **31**(2), 201–224 (2004).
Tokić, G., and Yue, D. K., "Hydrodynamics of periodic wave energy converter arrays," J. Fluid Mech. **862**, 34–74 (2019).
Wang, G., Zhang, M., Zhang, H., and Yu, F., "Wave diffraction from an array of porous cylinders with porous plates fixed inside," Ocean Eng. **245**, 110327 (2022).
Wang, C., Zheng, S., and Zhang, Y., "A heaving system with two separated oscillating water column units for wave energy conversion," Phys. Fluids **34**(4), 047103 (2022).
Wang, Z., "New wave power," Nature **542**(7640), 159–160 (2017).
Zeng, X., Shi, M., and Huang, S., "Hydrodynamic interactions of water waves with a group of independently oscillating truncated circular cylinders," Acta Mech. Sin. **32**(5), 773–791 (2016).
Zeng, X., Yu, F., Shi, M., and Wang, Q., "Fluctuation of magnitude of wave loads for a long array of bottom-mounted cylinders," J. Fluid Mech. **868**, 244–285 (2019).
Zeng, X., Kang, Y., Wang, G., Xue, Z., and Yu, F., "Approximate calculation method of hydrodynamic solution of an array with a large number of truncated cylinders," Ocean Eng. **257**, 111693 (2022a).
Zeng, X., Wang, Q., Kang, Y., and Yu, F., "Hydrodynamic interactions among wave energy converter array and a hierarchical genetic algorithm for layout optimization," Ocean Eng. **256**, 111521 (2022b).
Zeng, X., Wang, Q., Kang, Y., and Yu, F., "A novel type of wave energy converter with five degrees of freedom and preliminary investigations on power-generating capacity," Energies **15**(9), 3069 (2022c).
Zeng, X., Wang, Q., Shi, M., Kang, Y., and Yu, F., "Hydrodynamic interactions between waves and cylinder arrays of relative motions composed of truncated floating cylinders with five degrees of freedom," J. Fluids Struct. **115**, 103785 (2022d).
Zhang, H., Wang, T., Xu, C., Shi, H., and Guedes Soares, C., "Analysis on the split absorber integrated with taut-moored floating turbine," Phys. Fluids **35**(8), 087110 (2023).
Zhang, Y., Li, M., Zhao, X., and Chen, L., "The effect of the coastal reflection on the performance of a floating breakwater-WEC system," Appl. Ocean Res. **100**, 102117 (2020).
Zheng, S. and Zhang, Y., "Wave diffraction from a truncated cylinder in front of a vertical wall," Ocean Eng. **104**, 329–343 (2015).
Zheng, S. and Zhang, Y., "Wave radiation from a truncated cylinder in front of a vertical wall," Ocean Eng. **111**, 602–614 (2016).
Zheng, S., Meylan, M. H., Greaves, D., and Iglesias, G., "Water-wave interaction with submerged porous elastic disks," Phys. Fluids **32**(4), 047106 (2020).
Zhong, Q. and Yeung, R. W., "Wave-body interactions among energy absorbers in a wave farm," Appl. Energy **233–234**, 1051–1064 (2019).
Zhu, K., Zheng, S., Michele, S., Cao, F., Shi, H., and Greaves, D., "Wave diffraction and radiation from a semi-submersible floating foundation for wind turbines: A semi-analytical study," Phys. Fluids **35**(5), 057120 (2023).